Probing Dense Matter Through f-mode Oscillations of Anisotropic Compact Stars in General Relativity

By

Sushovan Mondal

PHYS10201804011

The Institute of Mathematical Sciences, Chennai

A thesis submitted to the

Board of Studies in Physical Sciences

In partial fulfillment of requirements

For the Degree of

DOCTOR OF PHILOSOPHY

of

HOMI BHABHA NATIONAL INSTITUTE

December 09, 2025

Homi Bhabha National Institute

Recommendations of the Viva Voce Committee

As members of the Viva Voce Committee, we certify that we have read the dissertation prepared by Sushovan Mondal titled "Probing Dense Matter Through f-mode Oscillations of Anisotropic Compact Stars in General Relativity" and recommend that it maybe accepted as fulfilling the thesis requirement for the award of Degree of Doctor of Philosophy.

V. Ravindran
____________________________ Date: 9-December-2025

Chairman: V. RAVINDRAN

Manjari Bagchi
____________________________ Date: 9-December-2025

Guide/Convener: MANJARI BAGCHI

____________________________ Date: 9-December-2025

Examiner: PARAMESWARAN AJITH

Sanatan Digal
____________________________ Date: 9-December-2025

Member 1: SANATAN DIGAL

Chandrashekar
____________________________ Date: 9-December-2025

* Member 2: C.M. CHANDRASHEKAR

____________________________ Date: 9-December-2025

Member 3: SITABHRA SINHA

____________________________ Date: 9-December-2025

Member 4 (External Member): K.G. ARUN

Final approval and acceptance of this thesis is contingent upon the candidate's submission of the final copies of the thesis to HBNI.

I hereby certify that I have read this thesis prepared under my direction and recommend that it may be accepted as fulfilling the thesis requirement.

Date: 9-December-2025

Manjari Bagchi

Place: Chennai

Guide

* C. M. Chandrashekar attended the viva online, all other members attended in person.

STATEMENT BY AUTHOR

This dissertation has been submitted in partial fulfillment of requirements for an advanced degree at Homi Bhabha National Institute (HBNI) and is deposited in the Library to be made available to borrowers under rules of the HBNI.

Brief quotations from this dissertation are allowable without special permission, provided that accurate acknowledgement of source is made. Requests for permission for extended quotation from or reproduction of this manuscript in whole or in part may be granted by the Competent Authority of HBNI when in his or her judgement the proposed use of the material is in the interests of scholarship. In all other instances, however, permission must be obtained from the author.

Sushovan Mondal.

Sushovan Mondal

DECLARATION

I, hereby declare that the investigation presented in the thesis has been carried out by me. The work is original and has not been submitted earlier as a whole or in part for a degree / diploma at this or any other Institution / University.

Sushovan Mondal

Sushovan Mondal

CERTIFICATION ON ACADEMIC INTEGRITY

Undertaking by the Student

1. I **Sushovan Mondal**, HBNI Enrolment No. **PHYS10201804011** hereby undertake that the Thesis, titled **"Probing Dense Matter through f-mode Oscillations of Anisotropic Compact Stars in General Relativity"** is prepared by me and is the original work undertaken by me.

2. I also hereby undertake that this document has been duly checked through a plagiarism detection tool and the document is found to be plagiarism free as per the guidelines of the Institute/UGC.

3. I am aware and undertake that if plagiarism is detected in my thesis at any stage in the future, suitable penalty will be imposed as per the guidelines of the Institute/UGC.

Sushovan Mondal
09.12.2025
Signature of the Student with date

Endorsed by the Thesis Supervisor:

I certify that the thesis written by the researcher is plagiarism free as mentioned above by the student.

Manjari Bagchi

Signature of the Thesis Supervisor with Date and Name (9-December-2025; Manjari Bagchi)

Designation : Professor

Department/ Centre : Theoretical Physics

Name of the CI/ OCC : The Institute of Mathematical Sciences

List of Publications arising from the thesis

- **Published**

  1. **S. Mondal** and M.Bagchi, *f-mode oscillations of anisotropic neutron stars in full general relativity*, Phys. Rev. D 110, 123011 (2024).
  2. **S. Mondal** and M.Bagchi, *Quasi-normal f-modes of anisotropic quark stars in full general relativity*, Phys. Rev. D 111, 103035 (2025).

Other Publications not included in the thesis

- **Published**

  1. **S. Mondal**, S. Ali, S. Shanima, N. Banerjee, and G.M. Hossain, *Propagation of gravitational waves in various cosmological backgrounds*, Gen. Relativ. Gravit. 53, 64 (2021).

Sushovan Mondal.

Sushovan Mondal

List of presentations and participations at conferences

- **Contributed presentations**

  1. Talk given on *Anisotropic Neutron Stars: Exploring Quasinormal Modes in Full General Relativity* in the *Young Researchers' Gravity Meeting* held at the Chennai Mathematical Institute, Chennai, India.
  2. Talk given on *Anisotropic Neutron Stars: Exploring Quasinormal Modes in Full General Relativity* in the *XXV SIGRAV Conference on General Relativity and Gravitation* held at the SISSA, Trieste, Italy.

- **Conferences attended**

  1. Participated in "Summer School on Gravitational-Wave Astronomy" organised at ICTS, Bengaluru, India from 24th July 2023 to 4th August 2023.
  2. Attended "Neutron star meeting" organised at Institute of Mathematical Sciences, Chennai, India from 1st to 3rd February 2023.
  3. Participated in the "Virtual Meeting on Compact Stars and QCD 2020" from 17th to 21st August 2020.
  4. Participated in " First Chennai Symposium on Gravitation and Cosmology" organised at IIT Madras, Chennai, India from 22nd to 24th January 2020.

Sushovan Mondal.

Sushovan Mondal

ACKNOWLEDGEMENTS

I am deeply grateful to my supervisor, Prof. Manjari Bagchi, for her unwavering support and encouragement throughout my research journey. Her guidance and advice have been indispensable, making this journey possible. Her expertise in the subject matter and insightful ideas served as a guiding light whenever I encountered obstacles in my research. She consistently encouraged me to think independently and to develop research problems from scratch. I feel fortunate to have had her as my advisor and mentor, and I will always be grateful for her contribution to building my confidence and fostering my academic growth.

I am extremely grateful to my doctoral committee members Prof. V. Ravindran, Prof. Sanatan Digal, Prof. C. M. Chandrashekar, Prof. Sitabhra Sinha, and Prof. K.G. Arun for their encouragement, insightful questions, and suggestions that helped improve my work. They have always been extremely considerate and supportive of me. I also thank Prof. Manjari Bagchi and Prof. Narayan Banerjee for introducing me to General Relativity and inspiring my interest in compact objects in the universe.

I would like to thank Prof. Nils Andersson, Prof. Hajime Sotani, and Prof. Leonardo Gualtieri for their support during the early stages of my research, especially through helpful email correspondence. I am also grateful to my group members Jyotijwal, Debabrata da, Pratik da, Sarbartha, Shaswata, and Subham, for numerous academic discussions that broadened my understanding of astrophysics beyond the scope of this thesis.

My heartfelt thanks go to Ms. Indra, Ms. Prema, and the entire administrative staff for their timely assistance and for managing the administrative responsibilities that allowed me to focus more fully on my research.

Now comes the part where gratitude alone doesn't suffice. I want to express not only my thanks but also my affection for those without whom this journey would have felt incomplete. I am especially grateful to my office mates, Tanmay (Saha), Jyotijwal (JJ), and Apurba (Apu), for always keeping the office atmosphere cheerful and far from monotonous. My time at IMSc will also be fondly remembered for countless academic and non-academic (and at times, completely nonsensical) conversations with friends and colleagues including Tanmay (Bera), Ankur, Manas, Vinod, JJ, Apu, and Saha.

This journey would not have been the same without our cherished afternoon tea breaks. I thank Anupam da, Debabrata da, Mrinal da, Ratan da, Arka da, Apu, Saha, JJ, and all other temporary and permanent members of the Tea Group. I am also grateful to Pratik, Krishnakumar, BCJ, and other InPTA members who helped me explore the observational side of astrophysics. I extend thanks to all my IMSc friends and colleagues with whom I played badminton, which helped me stay physically and mentally active during this long journey.

I would like to express my deepest gratitude to Mishti (Mohuya) for her unwavering support, patience, and countless sacrifices throughout this journey. This thesis would not have been possible without her constant love and belief in me.

Finally, I owe everything to my maa, baba, bhai, and my entire family. Their unconditional support, patience, and unwavering belief in me made it possible for me to pursue and complete my doctoral studies. Their regular check-ins and heartfelt curiosity about my work gave me the motivation and confidence I needed to persevere.

Contents

Summary

Compact stars, such as neutron stars and quark stars, serve as natural laboratories for exploring matter at extreme densities, inaccessible in terrestrial experiments. However, the microscopic physics governing such regimes remains uncertain due to limitations in our understanding of the nuclear and quark matter equations of state (EoS). Gravitational waves (GW) provide a promising probe of compact star interiors, with quasi-normal modes (QNMs)-which describe damped stellar oscillations-being potential GW sources. Among these, the fundamental (f-) modes are especially important, as they couple strongly to gravitational radiation and are sensitive to the star's global structure and internal composition.

This thesis investigates the f-mode oscillations of anisotropic compact stars using full general relativistic perturbation theory. In contrast to earlier studies based on pressure isotropy or simplified approximations such as the Cowling limit, the present work accounts for both fluid and metric perturbations. Anisotropy is physically motivated by microphysical effects such as superfluidity, pion condensation, strong magnetic fields, and elasticity. The impact of such anisotropy on the f-mode spectrum is analyzed for neutron and quark stars with realistic EoS.

Equilibrium configurations are constructed by extending the Tolman-Oppenheimer-Volkoff equations to include a specified anisotropy profile. Perturbation equations for non-radial oscillations are then derived by linearizing Einstein's field equations and fluid conservation laws, adopting the Regge-Wheeler gauge and restricting to even-parity modes. The

resulting boundary value problem is solved numerically with appropriate conditions at the center, surface, and spatial infinity.

The analysis shows that the f-mode frequency retains an approximately linear relation with the square root of the average density, in line with Newtonian results, but with slope and intercept altered by the anisotropic strength. For both neutron and quark stars, frequency increases with anisotropy for lower masses but decreases at higher masses. The damping time, which indicates gravitational wave energy loss, decreases monotonically with anisotropy for fixed mass. Anisotropy leads to significant variations in both frequency (up to ∼20%) and damping time (up to ∼300%) compared to the isotropic case, depending on the EoS. The inverse normalized damping time varies linearly with compactness, with anisotropy affecting the slope and intercept of this trend.

Semi-empirical relations are developed to express the frequency and damping time in terms of mass, radius, and anisotropic strength. The frequency exhibits a cubic dependence on anisotropy for both neutron and quark stars, while the damping time shows a sextic dependence for neutron stars and quartic for quark stars. These relations are expected to be useful in gravitational wave modeling and may assist in inferring stellar parameters from future observations.

In Chapter 2, we reviewed the Newtonian treatment of f-mode oscillations as a pedagogical prelude, highlighting the classical result that relates frequency to average stellar density. Chapter 3 discusses the equilibrium structure of anisotropic stars in general relativity based on known formalisms, setting the stage for perturbation analysis. In Chapter 4, we extended the general relativistic perturbation framework, originally developed for isotropic stars, to incorporate pressure anisotropy, systematically deriving the modified equations within the Regge-Wheeler gauge. Building upon this, Chapter 5 contains the core numerical results of this thesis, where we computed and analyzed f-mode frequencies and damping times for a range of realistic equations of state, providing new insights into how anisotropy influences quasi-normal f-modes in both neutron stars and quark stars.

In summary, this thesis provides a fully relativistic treatment of f-mode oscillations in anisotropic compact stars, demonstrating that pressure anisotropy significantly alters the quasi-normal mode spectrum. The results, including empirical fits, highlight the observational relevance of anisotropy and may aid in decoding gravitational wave signals. This framework may be extended in future to study other oscillation modes, rotational effects, and more realistic anisotropy models grounded in microphysics.

List of Figures

List of Tables

List of Abbreviations and Frequently Used Symbols

Abbreviations

GR	General Relativity
GW	Gravitational Waves
QNM	Quasi-normal Modes
EoS	Equation of State
EsoS	Equations of State
TOV	Tolman-Oppenheimer-Volkoff

Frequently Used Symbols

M	Mass of the star
R	Radius of the star
ρ	Density

p_r	Radial pressure
p_t	Tangential pressure
χ	Pressure difference, i.e., $p_t - p_r$
ω	Complex frequency of oscillation
$\mathcal{F}$	Real part of ω, i.e., oscillation frequency
$\mathfrak{T}$	Damping time
ν, λ	Metric functions in static spherically symmetric spacetime

Units and Conventions

Throughout this thesis, I adopt geometrized units by setting $G = c = 1$, where G is the gravitational constant and c is the speed of light in vacuum, unless stated otherwise.

Chapter 1

Introduction

1.1 Study of Gravitational Waves: A Brief History

Over a century ago, Albert Einstein introduced one of the most profound and elegant frameworks in modern physics: the general theory of relativity [3]. At the time of its formulation, the theory found confirmation through three key observational phenomena: the precession of Mercury's perihelion, the deflection of light in a gravitational field, and gravitational redshift. Since then, general relativity has remained the cornerstone of our understanding of gravitation.

Among its many groundbreaking predictions, one of the most remarkable was the existence of gravitational waves. Einstein first showed that his equations permitted small, wave-like disturbances that propagate at the speed of light in flat (Minkowski) spacetime [4, 5]. However, Einstein himself was skeptical about their physical reality.

This skepticism was later addressed by Pirani, who demonstrated that gravitational waves could cause measurable relative accelerations between freely falling particles, through their effect on the Riemann tensor [6, 7]. Around the same time, Bondi argued convincingly for the physical existence of gravitational waves and their ability to carry energy [8].

These developments laid the theoretical foundation for the experimental detection of gravitational waves, eventually motivating the construction of kilometer-scale ground-based interferometric detectors [9, 10].

A major milestone came with the discovery of the Hulse–Taylor binary pulsar system [11]. The gradual decay of its orbital period matched the predictions of general relativity due to gravitational wave emission, providing strong indirect evidence for the existence of gravitational waves.

The first direct detection, however, occurred much later. In 2016, the LIGO collaboration announced the historic observation of gravitational waves from a binary black hole merger [12]. This detection not only confirmed a century-old prediction of general relativity but also opened a new observational window into the universe.

Following this breakthrough, numerous binary black hole mergers were recorded by the LIGO-Virgo collaboration. A pivotal moment arrived on August 17, 2017, with the detection of GW170817, the first gravitational wave signal from a binary neutron star merger [13]. This event triggered a worldwide alert, leading to coordinated electromagnetic observations across the entire spectrum, from radio to gamma rays. This marked the dawn of multi-messenger astronomy and represents one of the most significant achievements in neutron star research.

More recently, the Pulsar Timing Array (PTA) collaborations have reported evidence for gravitational waves in the nanohertz regime [14, 15, 16], likely originating from supermassive black hole binaries. Looking ahead, planned observatories like the Laser Interferometer Space Antenna (LISA) [17, 18], the Einstein Telescope [19, 20], the Cosmic Explorer [21, 22], and others are expected to explore a wide range of gravitational wave sources. These facilities promise to deepen our understanding of the cosmos and unveil new classes of astrophysical objects.

1.2 Compact Stars as Gravitational-Wave Sources

Gravitational-wave sources are broadly classified into compact-binary coalescences, burst-like events, stochastic backgrounds, and continuous waves. Neutron stars appear in each category. The merger of two neutron stars or a neutron star and a black hole produces a strong coalescence signal; non-axisymmetric deformations in an isolated, spinning neutron star emit nearly monochromatic continuous waves; and violent processes such as supernova explosions, magnetar flares or glitches can give rise to burst-like emission. These signals are invaluable: as well as testing general relativity, they offer the potential to constrain the interior composition and equation of state (EoS) of neutron star matter.

The inspiral and merger of compact binary systems were predicted to be among the first detections of advanced interferometers, with estimated binary neutron star detection rates for the Advanced LIGO and Virgo network ranging from 0.4 to 400 per year [23]. This expectation was spectacularly realised on 17 August 2017 when the LIGO-Virgo Collaboration observed the gravitational-wave signal GW170817, a binary neutron star inspiral accompanied by multi-wavelength electromagnetic counterparts [13]. Since the start of the advanced detector era in 2015, the network has recorded hundreds of gravitational-wave events; by 19 March 2025 the LIGO-Virgo-KAGRA collaboration had catalogued approximately 290 candidate signals, although only two or three involve binary neutron star mergers [1]. Improvements during the ongoing O4 observing run have more than doubled the binary neutron star detection range to about 550 million light years (approximately 170 Mpc) [1], and are expected to deliver a merger detection every two or three days [2]. Among the events recorded so far are systems containing “mass gap” objects with masses between 2 and 5 $M_\odot$; determining whether these are unusually massive neutron stars or low-mass black holes is an active area of investigation [24]. (For example, the event GW190814 involved a 2.6 $M_\odot$ secondary, arguably the heaviest neutron star or lightest black hole known [25].) Future observations with next-generation ground-based

---

[1] https://www.ligo.caltech.edu/news/ligo20250320

[2] https://www.virgo-gw.eu/news/ligo-and-virgo-detectors-restart-gravitational-wave-observation/

detectors such as the Einstein Telescope and the Cosmic Explorer, as well as space-based interferometers like LISA, will further expand the accessible volume and frequency range, allowing precise measurements of tidal deformabilities and post-merger oscillations.

Isolated neutron stars are also promising continuous-wave sources. A rotating neutron star with a non-zero equatorial ellipticity ϵ radiates at twice its spin frequency with characteristic strain amplitude $h_0 \propto I_{zz} f_{\rm gw}^2 \epsilon/d$, where I_{zz} is the principal moment of inertia, ϵ is the ellipticity of the object, $f_{\rm gw}$ is the gravitational-wave frequency and d is the distance to the source. Such deformations may arise from crustal "mountains" sustained by the solid crust [26] or from strong internal magnetic fields [27].

Transient phenomena in isolated neutron stars can also produce gravitational radiation. Pulsar glitches, sudden jumps in the rotation frequency thought to result from the unpinning of superfluid vortices in the interior, transfer angular momentum between the core and crust and can excite broadband or continuous gravitational waves. Simulations suggest that the burst associated with a glitch could reach strains of $h_0 \sim 10^{-24}$ for typical parameters, but targeted searches of the 2006 Vela pulsar glitch have yielded non-detections, placing upper limits of $h_0 \lesssim 10^{-20}$. Similarly, magnetar giant flares may excite crustal and core oscillations through catastrophic rearrangements of ultra-strong ($B \gtrsim 10^{14}$ G) magnetic fields, though no gravitational waves were seen during the 2004 SGR 1806–20 flare [28]. Newly born neutron stars in supernova remnants may also emit strong gravitational waves due to large internal toroidal fields and differential rotation [29]; however, estimates are highly uncertain.

The detection of gravitational waves from neutron stars promises to revolutionise our understanding of dense matter. Binary inspirals encode the tidal deformability and radii of neutron stars, allowing constraints on the EoS. Continuous-wave detections would measure the star's moment of inertia and ellipticity, revealing details of crustal strength and internal magnetic fields. Burst signals from glitches and magnetar flares could probe superfluid physics and magneto-elastic coupling. With the advent of next-generation detectors and multi-messenger campaigns, gravitational-wave astronomy will provide an indispensable complement to electromagnetic observations, linking the macroscopic dynamics of neutron stars to the microphysics governing matter at supranuclear density.

1.3 Discovery of Neutron Stars

Neutron stars are among the most fascinating celestial objects, remarkable not only for their ability to contain a mass greater than that of the Sun within a radius of just about 10 kilometers (roughly the size of a city), but also for serving as natural laboratories for exploring physical phenomena under extreme conditions that are inaccessible in terrestrial experiments.

The idea of neutron stars was conceived even before the discovery of the neutron itself. As early as February 1931, Lev Landau proposed the concept of a star composed of extremely dense nuclear matter, resembling a gigantic atomic nucleus [30]. His paper was published on 29 February 1932 [31, 30, 32], just within a week James Chadwick announced the discovery of the neutron [33].

Nearly two years after the discovery of the neutron, Baade and Zwicky proposed the existence of neutron stars as the remnants of supernova explosions [34, 35]. This marked the beginning of a more concrete theoretical framework for such compact objects. In 1939, Tolman [36], and Oppenheimer and Volkoff [37], derived the general relativistic hydrostatic equilibrium equation for static, spherically symmetric stars, an essential equation governing the structure of neutron stars.

While theoretical understanding evolved gradually over the decades, a major observational breakthrough came in 1967 when Jocelyn Bell Burnell and Antony Hewish discovered pulsating radio sources, now known as pulsars [38]. These were soon identified as rotating neutron stars emitting beams of radiation. This discovery revolutionized astrophysics and established neutron stars as real, observable astrophysical entities. Since then, more than 3,000 pulsars have been detected across various wavelengths, making them a vital tool for probing fundamental physics under extreme conditions (for the most up-to-date count, see version 2.7.0 (recent version)[3] of [39]).

1.4 Birth of Compact Stars

Compact stars, including neutron stars and potentially quark stars, are formed from the catastrophic gravitational collapse that marks the end stage of a massive star's life cycle. Typically, stars with initial masses exceeding about $8\,M_\odot$ undergo such collapse. During most of its lifetime, a main-sequence star remains in hydrostatic equilibrium by fusing hydrogen into helium in its core. The energy released in the fusion process generates outward thermal pressure, which balances the inward pull of gravity and maintains the star's structural integrity.

As the hydrogen in the core is exhausted, gravitational contraction resumes. The core heats up, igniting helium fusion, while hydrogen burning continues in surrounding shells. In massive stars, the core undergoes successive stages of nuclear fusion such as, carbon, oxygen, magnesium, silicon, each occurring in concentric shells, forming an onion-like structure.

However, nuclear fusion ceases with the production of iron (^{56}Fe), which is most stable nucleus, as the binding energy per nucleon is highest for them. Since fusing iron does not yield energy, the core loses its primary source of outward pressure and becomes gravitationally unstable. As fusion stops, the core collapses under its own gravity.

Eventually, the collapsing core exceeds the Chandrasekhar limit ($\sim$1.4 $M_\odot$), at which point electron degeneracy pressure can no longer counteract gravity. This collapse is further accelerated by inverse beta decay, in which electrons and protons combine to form

---

[3] https://www.atnf.csiro.au/research/pulsar/psrcat/

neutrons and electron neutrinos:

$$p^+ + e^- \rightarrow n + \nu_e.$$

This process depletes the electron population, reducing degeneracy pressure and accelerating the collapse. Initially, the produced neutrinos escape freely, but once the core density reaches $\sim 10^{12}$ g/cm^3, neutrinos become trapped due to high opacity, altering the thermal and pressure balance.

As the density surpasses nuclear saturation ($\sim 2.8 \times 10^{14}$ g/cm^3), nucleons are squeezed into a uniform nuclear matter state. The short-range repulsion between nucleons and neutron degeneracy pressure, along with the contributions from trapped neutrinos, halt the collapse and produce a bounce that drives a shock wave outward. This shock, after gaining sufficient energy, expels the outer layers of the star in a supernova explosion.

For progenitors with initial masses above ~20 $M_\odot$, the remnant may undergo further collapse into a black hole. However, for progenitors with lower mass, the remnant core stabilizes into a neutron star. This proto-neutron star is initially extremely hot ($\sim 10^{11} - 10^{12}$ K) and cools rapidly by emitting trapped neutrinos. Within a day, the temperature typically drops to $\sim 10^9 - 10^{10}$ K, after which the star cools gradually through long-term neutrino emission.

The above discussion outlines the formation of neutron stars. However, another class of compact stars-quark stars-has been theorized. Itoh [40] first proposed that compact stars composed entirely of deconfined quark matter could exist in hydrostatic equilibrium. The Bodmer–Witten hypothesis later suggested that strange quark matter could be the true ground state of matter, being energetically more stable than ^{56}Fe [41, 42]. This hypothesis lays the foundation for the existence of quark stars, self-bound compact stars made entirely of up, down, and strange quarks.

Although direct observational evidence is lacking, several astrophysical objects have been proposed as possible quark star candidates. For instance, the low-mass central object in the supernova remnant HESS J1731−347 is a strong candidate [2, 43], as such a low-mass neutron star is unlikely to result from standard core-collapse supernova models. Other candidates include PSR B0943+10 [44] and PSR J0205+6449 [45], both of which show features that may be consistent with quark star models.

There are several proposed mechanisms by which a quark star may form:

(i) Direct Formation from Core Collapse: In massive stars undergoing Type II supernovae, if the core achieves sufficiently high density (several times nuclear saturation) during collapse, a first-order QCD phase transition could occur, leading to deconfined quark matter in the core. If this happens before black hole formation, the remnant may stabilize as a quark star [46].

(ii) Conversion from a Neutron Star: A neutron star may convert into a quark star over time as its central density increases due to mass accretion (e.g., from a binary companion) or spin-down. This may trigger a rapid phase transition into strange quark matter [47]. The process is exothermic and potentially violent, leading to a secondary explosion known as a "quark nova" [48], with energies of order 10^{52}–10^{53} erg.

(iii) Formation in Neutron Star Mergers: In binary neutron star mergers, the post-merger remnant is ultra-dense and may temporarily avoid black hole formation. If the remnant's core density and temperature are high enough, deconfinement may occur, resulting in a quark star or hybrid star. Some analyses, such as those of GW190425, suggest that the high mass of the remnant may be consistent with a stable quark star [49].

(iv) Primordial Quark Stars: In the early universe (around 10^{-5} seconds after the Big Bang), regions of deconfined quark matter could have survived hadronization during the QCD phase transition. If these "quark nuggets" converted into strange quark matter before pressure dropped significantly, they might have survived to the present day as stable relics [42].

In summary, while the existence of quark stars remains theoretical, several plausible formation scenarios have been proposed, ranging from stellar core collapse and binary mergers to early universe processes. The formation of such stars depends critically on the high-density equation of state, the nature of the quark–hadron phase transition, and the physical conditions required for deconfinement. Together, these possibilities provide a coherent framework for understanding how exotic compact stars composed of quark matter might arise in nature.

1.5 Inside the Compact Stars

1.5.1 Neutron Star

Surface: The surface of a neutron star, though only a few centimeters thick, plays a crucial role in shaping its thermal emission and observational characteristics. Its composition varies based on the neutron star's evolutionary history and environment, typically comprising hydrogen, helium, or heavier elements such as carbon. While hydrogen and helium atmospheres are common in accreting neutron stars, isolated neutron stars, such as the one in Cassiopeia A, often exhibit carbon-dominated atmospheres, likely due to nuclear burning or the lack of accretion [50, 51]. These differences in atmospheric composition significantly influence X-ray spectral modeling and, consequently, constraints on neutron star mass, radius, and cooling behavior.

Outer Crust: The outer crust consists of a dense lattice of neutron-rich nuclei embedded in a degenerate, ultra-relativistic electron gas. This crystalline structure extends from the surface to the neutron drip point. As one moves deeper, pressure increases due to the overlying material. This extreme environment, a remnant of the neutronization during the supernova collapse, drives beta capture reactions, i.e. electrons are captured by protons in nuclei, increasing their neutron content [52]. The stability of these increasingly neutron-

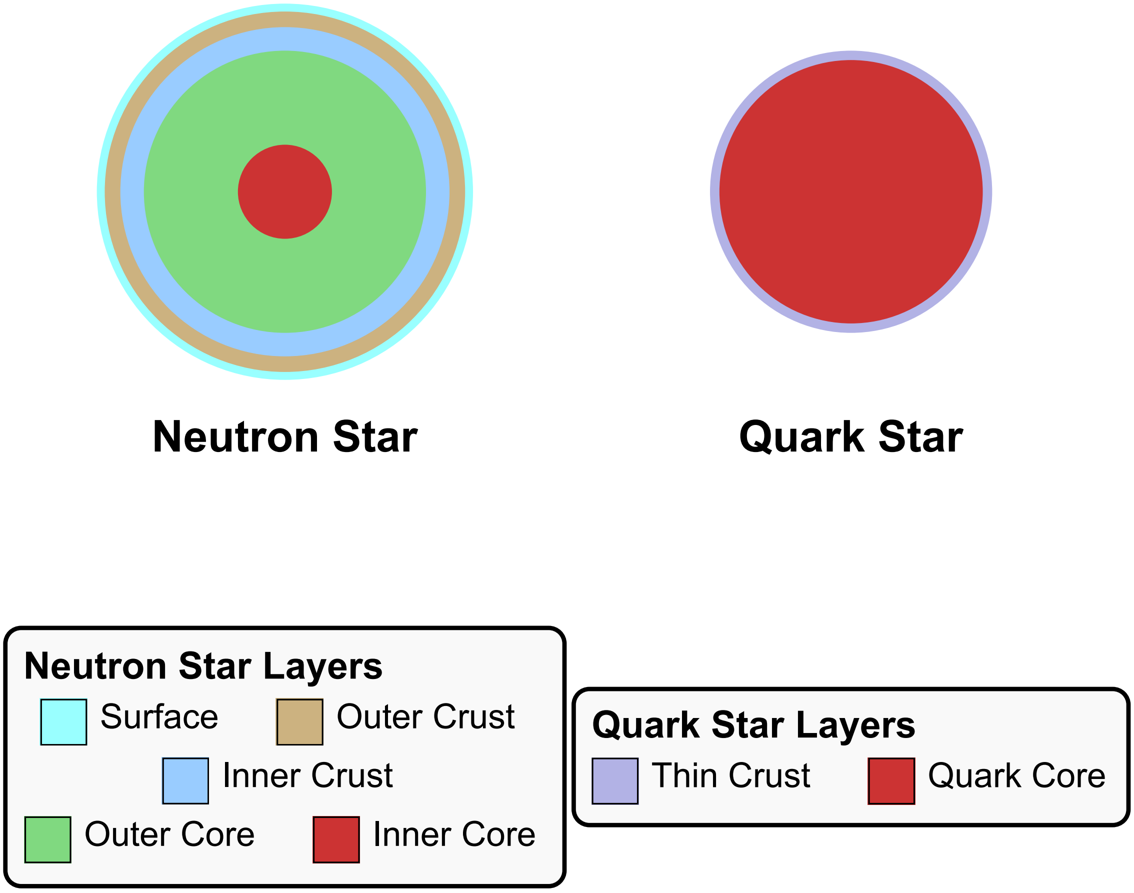

Figure 1.1: Schematic illustration of the internal structure of a neutron star and a quark star within the most established models. See text for details.

rich nuclei is governed by a competition between nuclear symmetry energy, Coulomb energy, and the electron Fermi energy, resulting in a stratified sequence of isotopes.

Inner Crust: Spanning densities from about 4.3×10^{11} g cm^{-3} to 2.0×10^{14} g cm^{-3}, the inner crust has a radial thickness of approximately 0.5 km. At the lower end of this range, neutrons begin to "drip" out of neutron-saturated nuclei, entering free states. This threshold defines the neutron drip density. The inner crust comprises extremely neutron-rich nuclei arranged in a Coulomb lattice, immersed in a sea of free neutrons and a highly degenerate, relativistic electron gas. At higher densities near the crust-core interface, complex configurations, commonly referred to as "nuclear pasta" phases may emerge due to the interplay of nuclear and Coulomb forces [53].

Outer Core: The outer core lies beneath the inner crust and spans densities from approximately 1.5×10^{14} g cm^{-3} to 2.0×10^{15} g cm^{-3} [54, 55]. This region is composed primarily of superfluid neutrons, a smaller fraction of protons (believed to form a type-II superconductor), and leptons such as electrons and muons to maintain charge neutrality. Superfluidity and superconductivity in this region profoundly influence thermal evolution, rotational dynamics, and magnetic field behavior, particularly in connection with pulsar glitches [56, 57]. Despite progress, the composition and interactions within the outer core remain uncertain and are central to constraining the dense matter equation of state.

Inner Core: The inner core, lying beneath the outer core, is characterized by densities exceeding approximately 2×10^{15} g cm^{-3}. Due to the extreme conditions, its composition is not well understood. Possible constituents include deconfined quark matter (in the form of a quark-gluon plasma), or hyperonic matter containing particles with strange quarks [57]. These exotic states could significantly affect the neutron star's maximum mass, radius, and oscillation modes, and are a major focus in the study of ultra-dense matter.

1.5.2 Quark Star

The potential existence of quark stars, compact stars composed entirely of deconfined quark matter, has garnered theoretical interest. Building on early ideas by Itoh [40], Bodmer [41], and Witten [42], quark stars are proposed as more compact, self-bound alternatives to neutron stars. Although still hypothetical, certain astrophysical candidates such as RX J1856.5−3754 and the remnant of HESS J1731−347 have been suggested as quark stars [2, 43].

Quark Matter Core: The core of a quark star consists of deconfined up, down, and strange quarks forming strange quark matter, hypothesized to be more stable than nuclear matter at sufficiently high densities [42]. In such stars, quarks are present in roughly equal numbers, with the inclusion of strange quarks reducing the energy per baryon. Unlike neutron stars, quark stars are primarily self-bound by the strong nuclear force, not gravity, which leads to a smooth density gradient without sharply defined layers [58]. At the center, matter is expected to be in the Color-Flavor Locked (CFL) phase, where quarks pair in a superconducting state locking color and flavor symmetries [59, 60]. At lower densities, the matter may transition to the 2SC phase, where only up and down quarks participate in superconductivity [61].

Outer Crust: The structure surrounding the quark matter core depends on whether the star is crusted or bare:

Crusted Quark Stars: These possess a thin nuclear crust composed of heavy ions and electrons, resembling the outer crust of neutron stars. However, the crust is significantly thinner, only a few hundred meters thick and has a mass around $10^{-5}M_{\odot}$ [62]. It is separated from the quark core by a sharp interface, and the density remains below neutron drip, ensuring no free neutrons exist.

Bare Quark Stars: In this configuration, no nuclear crust is present. The quark matter core extends directly to the surface, overlaid by a thin layer of electrons. A strong electric field, ranging from 10^{18} to 10^{19} V/cm, maintains this electron layer, generated by charge separation between the core and the surrounding electrons [63].

A schematic diagram illustrating the internal structures of a typical neutron star and a typical quark star is shown in Fig. 1.1.

1.6 Anisotropy Inside Compact Stars

In modeling the structure and physical properties of compact stars, it is commonly assumed that the pressure within the star is isotropic, i.e., equal in all directions. However, the possibility of anisotropic pressure, where radial and tangential components differ cannot be excluded. The concept of an anisotropic fluid was first introduced by Lemaitre [64] in the context of cosmological expansion. Subsequently, Bowers and Liang [65] investigated the equilibrium configurations of relativistic compact stars under the influence of pressure anisotropy. Their study revealed that even small local anisotropies could significantly alter global observables such as the mass and surface redshift of compact stars.

Several physical mechanisms have been proposed to induce anisotropy within compact stars. These include superfluidity [66, 67, 68], pion condensation [69], and skyrmion-based interactions [70]. Additionally, viscous effects are known to contribute to local pressure anisotropies in neutron stars [71, 72]. Yazadjiev [73] modeled magnetars in a nonperturbative general relativistic framework and demonstrated that the intense magnetic field could render the stellar matter anisotropic. Elastic deformations in neutron stars may also be effectively described using an anisotropic stress model [74, 75]. A comprehensive discussion of anisotropic pressures in self-gravitating systems, can be found in Herrera and Santos [76] and references therein.

1.7 Oscillations of Compact Stars

The theory of stellar oscillations originated from early studies of variable stars and was subsequently extended to compact objects such as neutron stars. A key historical insight is the period-density relation, which connects a star's pulsation period P to its mean density ρ_{avg}. In essence, denser stars exhibit shorter pulsation periods. Shapley (1914) applied this relation to argue that Cepheid variables are intrinsically pulsating stars rather than eclipsing binaries, noting that their observed periods match plausible average densities for oscillating bodies [77]. Later, Eddington (1918) laid the mathematical groundwork for stellar pulsation theory by modeling small radial oscillations of stars within Newtonian gravity [78].

Initially, attention focused on radial modes, spherically symmetric "breathing" oscillations. However, non-radial modes, involving complex surface patterns, became prominent with the discovery of the Sun's 5-minute oscillations in the 1960s [79], giving rise to the field of helioseismology. These developments motivated extensions of oscillation theory into the relativistic regime, particularly after the discovery of neutron stars and pulsars. Thorne and Campolattaro [80], followed by Price and Thorne [81], formulated a general relativistic treatment of non-radial perturbations, incorporating fluid dynamics and spacetime curvature.

The theory advanced significantly with numerical investigations by Lindblom and Detweiler [82] and Detweiler and Lindblom [83], who studied non-radial pulsations using realistic equations of state (EoS). These studies revealed that neutron star oscillations emit gravitational waves, giving rise to damped oscillations known as quasinormal modes (QNMs). Andersson and Kokkotas [84] later demonstrated that both the fundamental (f)-mode frequencies and their damping times are sensitive to the EoS, laying the foundation for gravitational wave asteroseismology. Using the same formalism, the non-radial oscillation modes are calculated for superfluid neutron stars [85], quark stars [86], neutron stars with density discontinuity [87, 88], etc. Recent studies on the impact of the equation of state on the neutron star oscillation modes reveal the fact that the inter-nuclei interactions have important effects on the quasi-normal modes [89]. Most of these studies assume pressure isotropy inside neutron stars.

Observational efforts to detect stellar oscillations initially focused on radio pulsar timing irregularities and pulse microstructure [90, 91, 92]. While direct detections remain elusive, the observation of gravitational waves from compact binary mergers by LIGO and Virgo [12, 93] has opened new avenues. Non-radial oscillation of compact stars are one of the prime candidate of gravitational waves. Phenomena such as pulsar glitches [94], non-spherical supernova explosions [95], and coalescence of compact stars [96, 97, 98, 99, 100] are among of the proposed causes of such non-radial, especially f-mode oscillations. These are the sources of gravitational wave in burst-like emission. Other than these sources, f-mode oscillation can also generate continuous gravitational waves by spinning compact stars. The instability of the f-mode sets in only above a critical spin rate, via the well-known Chandrasekhar-Friedman-Schutz (CFS) [101, 102] mechanism. In a rapidly rotating (millisecond-period) newborn neutron star, the CFS instability can drive the f-mode to grow and emit continuous gravitational waves [103, 104, 105]. Future observatories such as Cosmic Explorer and the Einstein Telescope are expected to be sensitive to high-frequency signals potentially linked to f-mode oscillations [106, 107].

The effects of anisotropy on non-radial oscillation modes were first studied by Hillebrandt and Steinmetz [108] in the Newtonian framework. This study revealed that pressure anisotropy plays a very important role in mode frequencies. Later, Doneva and Yazadjiev [109] calculated the frequencies for the f-mode and the p-mode oscillations using the Cowling approximation, where they ignored the metric perturbation. In a recent study, Curi et al. [110] extended this work for the case of realistic equations of state. All of the aforementioned studies showed that anisotropy in neutron stars can change the numerical value of the frequencies of the quasi-normal modes. Although the metric perturbation is ignored, the Cowling approximation provides sufficiently accurate results for fluid perturbations. However, the possibility of errors due to ignoring the metric perturbation might not be negligible. Recently, Sotani and Takiwaki [111] found that the mode frequencies under the Cowling approximation are estimated with approximately 20% accuracy. Another drawback of the Cowling approximation is that, as the metric perturbation is ignored, the energy loss due to gravitational waves is unaccounted for. In the full framework of general relativity that takes into account perturbations of the metric, the oscillation of the metric propagates as gravitational waves, which carry away the energy of the oscillations. As a result, the oscillation experiences damping, leading to a decrease in its amplitude over time.

Other than the study of oscillation modes of neutron stars, the oscillation modes of quark stars have been studied by several authors. Yip et al. [112] demonstrated that their f-mode frequencies differ significantly from those of neutron stars, implying stronger gravitational wave emission. Sotani and Harada [86] derived an empirical relation linking f-mode frequencies to EoS parameters of quark matter. Similar conclusions were reached in [113, 114], which showed that oscillation properties could help distinguish between quark and neutron stars. More recently, the Cowling approximation has been employed to analyze anisotropic quark stars [115, 116], though fully relativistic treatments remain relatively sparse.

In this thesis, we investigate the quasi-normal f-mode oscillations of anisotropic compact stars, both neutron stars and quark stars, within the framework of full general relativity. Starting from the equilibrium configurations of compact stars with pressure anisotropy, we derive and solve the linearized perturbation equations including both fluid and metric fluctuations. We compute the f-mode frequencies and damping times for a range of realistic equations of state and quantify the influence of anisotropy on these observables (frequency and damping time). The thesis is organized as follows. In Chapter 2, we present the basic theory of stellar oscillations in the Newtonian framework. Chapter 3 describes the equilibrium structure of anisotropic compact stars in general relativity. The derivation of the perturbation equations is detailed in Chapter 4. Chapter 5 presents the numerical results and analysis of the f-mode frequencies and damping times. Finally, we conclude with a summary of the main findings and future directions in Chapter 6.

Chapter 2

Equilibrium and f-mode Oscillations of Newtonian Stars

This chapter presents a review of the equilibrium structure and f-mode oscillations of stars in Newtonian gravity.

2.1 Equilibrium Stellar Structure

A star may be modeled as a self-gravitating, nearly spherical assembly of hot plasma, where the inward gravitational attraction is precisely balanced by the outward pressure arising from thermal and radiation forces. This balance, referred to as hydrostatic equilibrium, allows the star to maintain its structural integrity over extended timescales while generating energy through nuclear fusion at its core.

To derive the hydrostatic equilibrium condition within the framework of Newtonian gravity, let us analyze a cylindrical fluid element situated within the stellar interior. The element has a radial height dr and a cross-sectional area dS, located between radii r and $r + dr$. Assuming the local mass density ρ remains approximately uniform across this small region, the mass of the fluid element can be expressed as

$$\Delta m = \rho \, dr \, dS \,. \tag{2.1}$$

This fluid element is subjected to two opposing forces:

1. The gravitational attraction from the mass $m(r)$ enclosed within the radius r, which pulls the element inward.
2. The differential pressure across its radial faces, which exerts a net outward force.

The gravitational force acting on the element is

$$F_{\text{grav}} = -\frac{Gm(r)\Delta m}{r^2}, \tag{2.2}$$

where G is the gravitational constant, and $m(r)$ denotes the mass enclosed within the spherical region of radius r. On the other hand, the pressure difference between the top and bottom surfaces yields a net force given by

$$F_{\text{pressure}} = [P(r + dr) - P(r)] \, dS \, = \frac{dP}{dr} \, dr \, dS \,. \tag{2.3}$$

Substituting the expression for Δm from Eq. (2.1) and applying the equilibrium condition $F_{\text{grav}} + F_{\text{pressure}} = 0$, we get

$$-\frac{Gm(r)\Delta m}{r^2} = \frac{dP}{dr} \cdot \frac{\Delta m}{\rho}. \tag{2.4}$$

Canceling Δm and simplifying, we arrive at the hydrostatic equilibrium equation:

$$\frac{dP}{dr} = -\rho \, \frac{Gm(r)}{r^2}. \tag{2.5}$$

This equation expresses how the pressure must vary with radius in order to maintain mechanical stability under the influence of self-gravity.

The mass increment dm enclosed within a thin spherical shell of thickness dr at radius r is given by

$$\begin{aligned} dm &= \rho\, dV \\ &= \rho\, 4\pi r^2\, dr. \end{aligned} \tag{2.6}$$

This leads to the differential form:

$$\frac{dm}{dr} = 4\pi r^2 \rho, \tag{2.7}$$

which describes how the enclosed mass changes with radius in terms of the local mass density $\rho(r)$.

Another important quantity is the gravitational potential $\Phi(r)$ produced by the enclosed mass $m(r)$, defined in Newtonian theory as

$$\Phi(r) = -\frac{Gm(r)}{r}. \tag{2.8}$$

The corresponding gravitational field (acceleration experienced by a test particle) is then obtained from the negative gradient of the potential:

$$\begin{aligned} \vec{g} &= -\nabla\Phi \\ &= -\frac{Gm(r)}{r^2}\hat{r}, \end{aligned} \tag{2.9}$$

where $\hat{r}$ denotes the unit vector along the radial direction. Next, let us consider an infinitesimal surface element on a spherical shell of radius r:

$$d\vec{S} = r^2 \sin\theta\, d\theta\, d\phi\, \hat{r}. \tag{2.10}$$

The gravitational flux through this surface is given by the scalar product

$$\begin{aligned} \vec{g} \cdot d\vec{S} &= -\left(\frac{Gm(r)}{r^2}\hat{r}\right) \cdot \left(r^2 \sin\theta \, d\theta \, d\phi \, \hat{r}\right) \\ &= -Gm(r) \, \sin\theta \, d\theta \, d\phi \, . \end{aligned} \tag{2.11}$$

Integrating over the entire spherical surface, we obtain the total gravitational flux:

$$\begin{aligned} \oint \vec{g} \cdot d\vec{S} &= -Gm(r) \int_0^{2\pi} d\phi \int_0^{\pi} \sin\theta \, d\theta \\ &= -4\pi G m(r) \, . \end{aligned} \tag{2.12}$$

According to Gauss's divergence theorem,

$$\oint_{\partial V} \vec{g} \cdot d\vec{S} = \int_V (\nabla \cdot \vec{g}) \, d^3 r \, . \tag{2.13}$$

Comparing with the expression above, we find

$$\int_V (\nabla \cdot \vec{g}) \, d^3 r = -4\pi G \int_V \rho(r) \, d^3 r \, , \tag{2.14}$$

which leads to the pointwise identity:

$$\nabla \cdot \vec{g} = -4\pi G \rho(r) \, . \tag{2.15}$$

Since $\vec{g} = -\nabla\Phi$, we substitute this into the above to obtain:

$$\nabla \cdot (-\nabla\Phi) = -4\pi G \rho(r), \tag{2.16}$$

which simplifies to the Poisson equation for the Newtonian gravitational potential:

$$\nabla^2 \Phi = 4\pi G \rho(r) \, . \tag{2.17}$$

We now consider the dynamics of a non-rotating, incompressible fluid configuration to analyze the oscillatory behavior. Two essential equations from fluid dynamics are required.

The first is the continuity equation, derived from the conservation of mass:

$$\frac{\partial \rho}{\partial t} + \nabla \cdot (\rho \vec{u}) = 0 \, , \tag{2.18}$$

where $\vec{u}$ is the velocity field of the fluid. The second is the momentum conservation equation, also known as Euler's equation:

$$\frac{\partial \vec{u}}{\partial t} + (\vec{u} \cdot \nabla)\vec{u} + \frac{1}{\rho}\nabla p + \nabla \Phi = 0 \, . \tag{2.19}$$

For an incompressible fluid, the density ρ remains constant throughout the star. Therefore, the time derivative and the spatial divergence of ρ both vanish:

$$\frac{\partial \rho}{\partial t} = 0, \quad \nabla \cdot \rho = 0. \tag{2.20}$$

Inserting this into the continuity equation (Eq. 2.18) yields:

$$\nabla \cdot \vec{u} = 0 \, , \tag{2.21}$$

which implies that the velocity field is solenoidal.

2.2 f-mode Oscillations of a Newtonian Star

To study the oscillations of the star, we now introduce linear perturbations around the equilibrium configuration. The perturbed variables are defined as:

$$\vec{u} \to \vec{u} + \delta\vec{u}, \tag{2.22}$$

$$p \to p + \delta p, \tag{2.23}$$

$$\Phi \to \Phi + \delta\Phi. \tag{2.24}$$

Since the fluid is incompressible, the density remains constant, i.e., $\delta\rho = 0$. Substituting this into the Poisson equation (Eq. 2.17) gives:

$$\nabla^2\delta\Phi = 0\,, \tag{2.25}$$

since the source term $\delta\rho$ vanishes.

Similarly, the linearized form of the continuity equation, using Eq. (2.21), becomes:

$$\nabla\cdot\delta\vec{u} = 0\,. \tag{2.26}$$

This condition implies that the perturbed velocity field is irrotational and can therefore be expressed as the gradient of a scalar potential:

$$\delta\vec{u} = \nabla\Psi\,, \tag{2.27}$$

where Ψ is the velocity potential. Substituting this into Eq. (2.26), we obtain

$$\nabla^2\Psi = 0\,. \tag{2.28}$$

We now turn our attention to the Euler equation (Eq. 2.19). Linearizing it with respect to the perturbed quantities yields:

$$\frac{\partial \delta \vec{u}}{\partial t} + \frac{1}{\rho} \nabla \delta p + \nabla \delta \Phi = 0 \, . \tag{2.29}$$

Taking the divergence of Eq. (2.29) and employing Eqs. (2.26) and (2.25), we obtain:

$$\nabla^2 \delta p = 0 \, . \tag{2.30}$$

Thus, the perturbed velocity potential Ψ, the perturbed gravitational potential $\delta\Phi$, and the pressure perturbation δp all satisfy Laplace's equation.

Applying separation of variables and imposing regularity conditions at the stellar center, we obtain the following general solutions:

$$\Psi = a_l \, r^l \, Y_l^m(\theta, \phi), \tag{2.31}$$

$$\delta\Phi = b_l \, r^l \, Y_l^m(\theta, \phi), \tag{2.32}$$

$$\delta p = c_l \, r^l \, Y_l^m(\theta, \phi), \tag{2.33}$$

where a_l, b_l, and c_l are mode amplitudes (possibly time-dependent), and $Y_l^m(\theta, \phi)$ are spherical harmonics.

Integrating the linearized Euler equation (Eq. 2.29) gives:

$$\frac{\partial \Psi}{\partial t} + \frac{1}{\rho} \delta p + \delta \Phi = D \, , \tag{2.34}$$

where D is a constant of integration. Since all the terms on the left-hand side vanish at $r \to 0$, regularity at the center demands that we set $D = 0$ everywhere.

Assuming harmonic time dependence of the perturbations, $\Psi \propto e^{i\omega t}$, Eq. (2.34) leads to:

$$i\omega a_l + \frac{c_l}{\rho} + b_l = 0 \,. \tag{2.35}$$

To complete the system, we now apply the boundary condition for the Lagrangian pressure perturbation at the surface:

$$\Delta p = \delta p + \xi^r \frac{dp}{dr} = 0 \,. \tag{2.36}$$

The radial displacement ξ^r is related to the perturbed velocity via:

$$\delta u^r = \frac{\partial \xi^r}{\partial t} = \frac{d\Psi}{dr} = a_l \, l \, r^{l-1} \, Y_l^m \,. \tag{2.37}$$

For an incompressible fluid star in equilibrium, the pressure gradient is:

$$\frac{dp}{dr} = -\frac{4\pi G \rho^2 r}{3} \,. \tag{2.38}$$

Substituting the expressions for δp, ξ^r, and dp/dr into the boundary condition, we obtain:

$$c_l = \frac{4\pi G \rho^2 l}{3 i\omega} a_l \,. \tag{2.39}$$

The boundary condition for the gravitational potential requires continuity of $\delta\Phi$ and its derivative at the stellar surface:

$$\left. \frac{d\delta\Phi}{dr} + \frac{l+1}{R}\delta\Phi \right|_{r=R} = -4\pi G \rho \, \xi^r(R) \,, \tag{2.40}$$

which yields:

$$b_l = -\frac{4\pi G \rho l}{(2l+1) i\omega} a_l \,. \tag{2.41}$$

Substituting the results from Eqs. (2.39) and (2.41) into Eq. (2.35), we arrive at the expression for the square of the fundamental mode frequency:

$$\omega^2 = \frac{8\pi G\rho}{3} \cdot \frac{l(l-1)}{2l+1} \, . \tag{2.42}$$

This result clearly shows that the square of the f-mode frequency is proportional to the average density of the star. One point to notice, is the fact that, the frequency ω is real for Newtonian case, on the other hand when we consider full general relativistic treatment, we will find that ω becomes complex, which indicates the loss of energy of oscillation with time. We will discuss about this in Chapter 4. It serves as a foundational relation in stellar seismology, linking macroscopic stellar properties to measurable oscillation frequencies.

Chapter 3

Equilibrium Structure of Anisotropic Compact Stars in General Relativity

In this chapter, we examine the equilibrium structure of compact stars in the presence of pressure anisotropy. As discussed earlier, such stars can be modeled as massive, self-gravitating fluid spheres, whose stability arises from the interplay between two opposing forces: the inward pull of gravity due to the mass of the star and the outward push generated by internal pressure. For main-sequence stars, this pressure is predominantly maintained by thermal energy released through nuclear fusion. In contrast, for compact stars like white dwarfs and neutron stars, quantum degeneracy pressure becomes the primary source of support.

Gravitational interactions play a fundamental role in determining the equilibrium configurations of these objects. Under Newtonian gravity, the gravitational potential scales approximately with the ratio M/R, where M and R denote the mass and radius of the star, respectively. This dimensionless quantity is commonly referred to as the compactness parameter. For stars such as the Sun, the compactness is extremely small (on the order of $\sim 10^{-6}$), and Newtonian gravity offers a sufficiently accurate framework for understanding their structure. On the other hand, neutron stars and quark stars possess much higher compactness (typically around ~ 0.1), resulting in strong gravitational fields where Newtonian mechanics no longer provides an adequate description.

In such strongly relativistic regimes, Einstein's theory of general relativity must be employed to properly describe the internal structure of compact stars. Since the focus of this work is on neutron stars and quark stars, we shall adopt a general relativistic framework to investigate their equilibrium properties. To proceed, we begin with a brief overview of the essential concepts of general relativity relevant to our analysis.

3.1 A Brief Review of General Relativity

This section provides a concise overview of the general theory of relativity, focusing on the key mathematical framework and essential equations that will be used throughout the thesis. As general relativity is a geometric theory of gravitation, we begin by introducing the spacetime structure on which the theory is formulated.

We consider a four-dimensional differentiable manifold $\mathcal{M}$ (spacetime), equipped with local coordinates x^μ where $\mu = 0, 1, 2, 3$. The infinitesimal separation between neighboring points in spacetime is given by dx^μ, and the invariant interval is defined by the spacetime metric $g_{\mu\nu}$ as follows:

$$ds^2 = g_{\mu\nu} dx^\mu dx^\nu. \tag{3.1}$$

The metric tensor $g_{\mu\nu}$ encapsulates the curvature and causal structure of spacetime. To describe how objects move in this curved geometry, we introduce the Christoffel symbols, which depend on the metric and its first derivatives:

$$\Gamma^\mu{}_{\alpha\beta} = \frac{1}{2} g^{\mu\nu} \left(\partial_\beta g_{\nu\alpha} + \partial_\alpha g_{\beta\nu} - \partial_\nu g_{\alpha\beta} \right), \tag{3.2}$$

where ${\Gamma^{\mu}}_{\alpha\beta}$ are the connection coefficients that govern how vectors are transported across curved spacetime. The symmetry ${\Gamma^{\mu}}_{\alpha\beta} = {\Gamma^{\mu}}_{\beta\alpha}$ implies that the connection is torsion-free.

The curvature of spacetime is captured by the Riemann curvature tensor, constructed from the Christoffel symbols as:

$$ {R^{\rho}}_{\sigma\mu\nu} = \partial_{\mu}{\Gamma^{\rho}}_{\sigma\nu} - \partial_{\nu}{\Gamma^{\rho}}_{\sigma\mu} + {\Gamma^{\rho}}_{\lambda\mu}{\Gamma^{\lambda}}_{\sigma\nu} - {\Gamma^{\rho}}_{\lambda\nu}{\Gamma^{\lambda}}_{\sigma\mu}. \tag{3.3} $$

This tensor measures the tidal deformation caused by the gravitational field. If all components of the Riemann tensor vanish, the spacetime is flat, indicating an absence of gravitational effects.

By contracting the Riemann tensor, we obtain the Ricci tensor:

$$ R_{\alpha\beta} = g^{\gamma\sigma} R_{\alpha\gamma\beta\sigma}, \tag{3.4} $$

which encapsulates the portion of curvature directly related to the energy-momentum content. The trace of the Ricci tensor gives the Ricci scalar, $R = g^{\mu\nu} R_{\mu\nu}$.

These ingredients are combined to define the Einstein tensor:

$$ G_{\mu\nu} = R_{\mu\nu} - \frac{1}{2} g_{\mu\nu} R, \tag{3.5} $$

which is divergence-free by virtue of the Bianchi identities and serves as the left-hand side of Einstein's field equations.

The Einstein field equations, which form the cornerstone of general relativity, relate spacetime curvature to the energy and momentum of matter:

$$ G_{\mu\nu} = 8\pi T_{\mu\nu}, \tag{3.6} $$

where $T_{\mu\nu}$ is the energy-momentum tensor, representing the matter and energy content of the spacetime.

In the context of this thesis, which focuses on the equilibrium structure and oscillatory behavior of compact stars, the Einstein field equations will play a central role in describing how spacetime curvature responds to dense stellar matter distributions.

3.2 Stellar Structure in General Relativity

Since general relativity is a geometric theory of gravitation, the starting point for modeling stellar structure is the specification of the spacetime metric suitable for a static, spherically symmetric mass distribution. In such a scenario, the natural choice of coordinates is the spherical polar coordinate system (t, r, θ, ϕ). The spacetime line element, as introduced in Eq. (3.1), takes the form:

$$ds^2 = -e^{\nu(r)}dt^2 + e^{\lambda(r)}dr^2 + r^2 d\theta^2 + r^2 \sin^2\theta \, d\phi^2, \tag{3.7}$$

where $\nu(r)$ and $\lambda(r)$ are functions of the radial coordinate r alone. Here, $e^{\nu(r)}$ characterizes the temporal part of the metric, while $e^{\lambda(r)}$ describes the radial component. Once this metric is specified, the relevant geometric quantities needed for the Einstein equations can be calculated as outlined in the previous section.

To model matter in compact stars, we consider an anisotropic fluid, wherein the radial pressure p_r and tangential pressure p_t differ from each other. Like the metric functions, both pressures are functions of the radial coordinate, although we suppress the explicit dependence for notational simplicity.

The measure of anisotropy is defined as

$$\chi = p_t - p_r, \tag{3.8}$$

which follows the convention adopted by Horvat et al. [117]. (It is worth noting that some authors define this with the opposite sign, e.g., $\chi = p_r - p_t$ [109, 110].)

The energy-momentum tensor describing an anisotropic fluid is given by [118, 119]:

$$T^{\beta}_{\ \alpha} = (\rho + p_t)\, u^{\beta} u_{\alpha} + p_t\, \delta^{\beta}_{\ \alpha} + (p_r - p_t)\, s^{\beta} s_{\alpha}, \tag{3.9}$$

where ρ denotes the energy density of the fluid. The unit spacelike vector in the radial direction is defined as:

$$s^{\alpha} = (0, e^{-\lambda/2}, 0, 0), \tag{3.10}$$

and the four-velocity of the static fluid configuration is:

$$u^{\beta} = (e^{-\nu/2}, 0, 0, 0). \tag{3.11}$$

These vectors satisfy the following normalization and orthogonality conditions:

$$u^{\alpha} u_{\alpha} = -1, \tag{3.12a}$$

$$s^{\alpha} s_{\alpha} = 1, \tag{3.12b}$$

$$s^{\alpha} u_{\alpha} = 0. \tag{3.12c}$$

The only nonvanishing components of the energy-momentum tensor in a static, spherically symmetric configuration are given by $T^{\beta}_{\ \alpha} = \mathrm{diag}(-\rho, p_r, p_t, p_t)$. The Einstein field equations relate the spacetime geometry to the energy-momentum distribution as:

$$G^{\beta}_{\ \alpha} = 8\pi T^{\beta}_{\ \alpha}, \tag{3.13}$$

where $G^{\beta}_{\ \alpha}$ denotes the Einstein tensor constructed from the metric (3.7).

By substituting the metric from Eq. (3.7) and the energy-momentum tensor from Eq. (3.9) into the field equations, one obtains the following set of differential equations:

$$
e^{-\lambda}\left(\frac{\lambda'}{r}-\frac{1}{r^2}\right)+\frac{1}{r^2}=8\pi\rho, \tag{3.14}
$$

$$
e^{-\lambda}\left(\frac{\nu'}{r}+\frac{1}{r^2}\right)-\frac{1}{r^2}=8\pi p_r, \tag{3.15}
$$

$$
\frac{1}{2}e^{-\lambda}\left(\nu''-\frac{1}{2}\nu'\lambda'+\frac{1}{2}\nu'^2+\frac{\nu'-\lambda'}{r}\right)=8\pi p_t, \tag{3.16}
$$

where the prime denotes differentiation with respect to the radial coordinate r.

Combining Eqs. (3.14)–(3.16) leads to the generalization of the hydrostatic equilibrium condition for an anisotropic fluid:

$$
p_r' = -\frac{\nu'}{2}(\rho+p_r)+\frac{2\chi}{r}, \tag{3.17}
$$

where $\chi = p_t - p_r$ is the anisotropy parameter.

Integrating Eq. (3.14) yields the expression for the metric function $e^{-\lambda(r)}$:

$$
e^{-\lambda} = 1-\frac{2m(r)}{r}, \quad \text{with} \quad m(r)=4\pi\int_0^r \rho(r')\,r'^2\,dr', \tag{3.18}
$$

where $m(r)$ represents the mass enclosed within a radius r.

Inserting Eq. (3.18) into Eq. (3.15) and combining with Eq. (3.17) gives the modified Tolman–Oppenheimer–Volkoff (TOV) equation for anisotropic matter:

$$
p_r' = -\frac{(\rho+p_r)(m+4\pi p_r r^3)}{r(r-2m)}+\frac{2\chi}{r}. \tag{3.19}
$$

To solve this system of equations, one must provide an equation of state (EoS) relating the radial pressure p_r to the energy density ρ, along with a prescription for the anisotropy parameter χ. The boundary conditions require a finite central pressure and the vanishing of the radial pressure at the surface, i.e., $p_r(R) = 0$, which also implies $\rho(R) = 0$ at the stellar boundary.

The interior spacetime must match continuously to the Schwarzschild exterior solution at $r = R$, leading to the condition:

$$\lambda(R) = -\nu(R) = -\ln\left(1 - \frac{2M}{R}\right), \tag{3.20}$$

where $M = m(R)$ denotes the total gravitational mass of the star.

3.3 Equations of State of Compact Stars

To solve the equilibrium equations governing compact stars, namely Eq. (3.18) and Eq. (3.19), it is essential to prescribe how both the radial and tangential pressures vary with the energy density. While different physical mechanisms may give rise to pressure anisotropy, leading to distinct equations of state (EoS) in the radial and tangential directions, this work does not focus on any specific microscopic origin of anisotropy. Instead, we adopt a phenomenological framework, the radial pressure is computed from well established nuclear and quark matter EsoS, whereas the tangential pressure is constructed through an ansatz that consistently incorporates anisotropic effects.

3.3.1 Ansatz for Anisotropy

Various functional forms for the anisotropy parameter χ have been proposed in the literature, including models by Bowers and Liang [65], Cosenza et al. [120], and Horvat et al. [117]. In this work, we employ the formulation introduced by Horvat et al., which ensures regularity at the stellar center and consistency with Newtonian gravity in the low-compactness limit:

$$\chi = \tau \, p_r \, \mu, \tag{3.21}$$

where $\mu = 2m/r$ denotes the local compactness, and τ is a dimensionless parameter characterizing the strength of anisotropy. This choice ensures that $\chi \to 0$ near the center since $\mu \sim r^2$ as $r \to 0$, and anisotropy is naturally suppressed in the Newtonian regime where $\mu \ll 1$. Following earlier works [109, 121, 122], we consider the range $-2 \leq \tau \leq 2$, which includes values motivated by physical models such as $\tau \in [0, 1]$ for pion condensation [69] and $\tau = -2$ in skyrmionic matter [70].

3.3.2 Stability Criteria for Equilibrium Configurations

Although one can solve the modified TOV equation for a range of central densities (ρ_c) and anisotropy parameters (τ), not all resulting stellar models are physically stable. First, to prevent spontaneous collapse, the pressure must be a monotonically increasing function of energy density [123], requiring that $\partial p_r/\partial\rho > 0$ and $\partial p_t/\partial\rho > 0$.

Second, the speed of sound in both radial and tangential directions must be real and positive, i.e., $v_{sr} > 0$ and $v_{st} > 0$, where $v_{sr}^2 = \partial p_r/\partial\rho$ and $v_{st}^2 = \partial p_t/\partial\rho$. While a physically realistic EoS satisfies $v_{sr} > 0$, due to limited knowledge about pressure anisotropy, our use of phenomenological ansatzes means v_{st} may become negative for some density ranges, and this must be explicitly checked.

Third, causality imposes that the sound speed does not exceed the speed of light in the neutron star matter, i.e., $v_{sr} < v_{\text{light}}$ and $v_{st} < v_{\text{light}}$. As the precise value of v_{light} in dense matter is uncertain, we take $v_{\text{light}} = 0.95\,c$, where c is the speed of light in vacuum (set to 1 in natural units).

Fourth, stability against radial perturbations demands that $\partial M/\partial\rho_c > 0$ [58]. We will explicitly illustrate the corresponding bound and constraints in the forthcoming sections.

3.3.3 Equations of state for neutron stars

To describe the equation of state for neutron stars in the radial direction, i.e. $p_r(\rho)$, we use the analytical representation of the Brussels - Montreal unified EoS for the nuclear matter, known as BSk19, BSk20, BSk21 [124, 125, 126], which model $p_r(\rho)$ with two parameters ζ and σ that are parametrized as [127]:

$$\begin{aligned}\zeta =& \frac{a_1 + a_2\sigma + a_3\sigma^3}{1 + a_4\sigma} f(a_5(\sigma - a_6)) + (a_7 + a_8\sigma) f(a_9(a_6 - \sigma)) + (a_{10} + a_{11}\sigma) f(a_{12}(a_{13} - \sigma)) \\ &+ (a_{14} + a_{15}\sigma) f(a_{16}(a_{17} - \sigma)) + \frac{a_{18}}{1 + [a_{19}(\sigma - a_{20})]^2} + \frac{a_{21}}{1 + [a_{22}(\sigma - a_{23})]^2},\end{aligned} \tag{3.22}$$

where $\zeta = \log_{10}(p_r \text{ in dyn cm}^{-2})$, $\sigma = \log_{10}(\rho \text{ in g cm}^{-3})$, and $f(x) = [\exp(x) + 1]^{-1}$. The values of the coefficients $a_i (i = 1, \ldots, 23)$ are available in Potekhin et al. [127]. In this thesis, our analysis primarily uses BSk21 EoS. However, to compare our results across different levels of matter stiffness, we also consider BSk19 EoS in selected cases. We observe that, for both BSk21 and BSk19 EsoS, as the value of τ increases, the maximum value of the central density up to which we get neutron stars that are stable against radial oscillations decreases. To assess whether the chosen EsoS, the anisotropy model, and the range of τ satisfy these stability criteria, we solve the modified TOV equations for different central densities and values of τ in the range $[-2, 2]$. In Figs. 3.1 and 3.2, we plot the resulting total mass M against ρ_c for the BSk21 and BSk19 EsoS, respectively.

In these plots, filled circles indicate points where $\partial M/\partial\rho_c = 0$. Asterisks mark the maximum ρ_c values for which $v_{sr} \leq 0.95$ throughout the star. Filled squares denote central

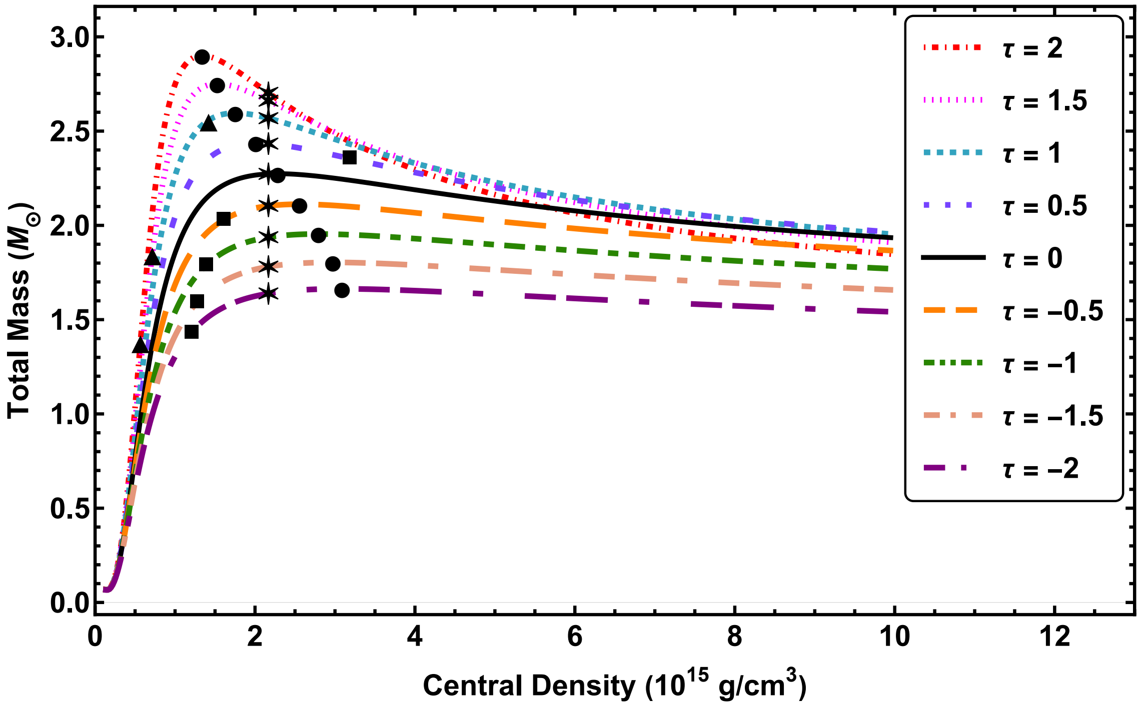

Figure 3.1: Mass (M)–central density (ρ_c) relations for anisotropic neutron stars with $-2 \leq \tau \leq 2$ using the BSk21 EoS. Filled circles mark configurations where $\partial M/\partial\rho_c = 0$. Asterisks indicate the maximum ρ_c for which $v_{sr} \leq 0.95$ throughout the star. Filled squares and triangles denote the central densities up to which $v_{st} \leq 0.95$ and $v_{st} \geq 0$ conditions are satisfied, respectively.

densities up to which $v_{st} \leq 0.95$, and filled triangles represent regions where $v_{st} \geq 0$ is maintained.

From the results, we observe that for both BSk21 and BSk19 EsoS, increasing the anisotropy parameter τ generally leads to a decrease in the maximum central density at which stars remain stable under radial oscillations. For $\tau \leq 0$, the radial sound speed v_{sr} reaches the causal limit (0.95) at a lower central density than the value corresponding to $\partial M/\partial\rho_c = 0$, while v_{st} hits this limit even earlier. In contrast, for $\tau \geq 0$, v_{st} often remains below 0.95 for most central densities; however, it may turn negative except at very low ρ_c. On the other hand, for the chosen set of EsoS, the anisotropy ansatz, and the range of the values of τ, v_{sr} always remain positive throughout the star.

Subsequently, we present the mass−radius profiles corresponding to different values of τ (within the range −2 to 2) for the BSk21 EoS in Fig. 3.3 and for the BSk19 EoS in

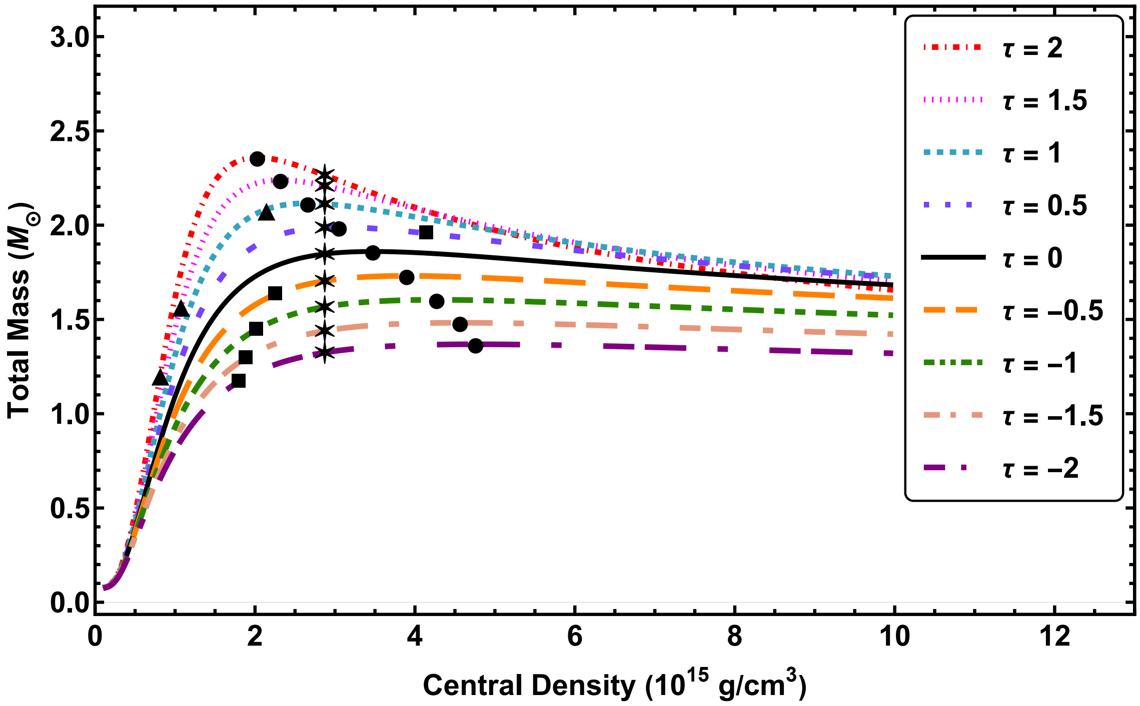

Figure 3.2: Mass (M)–central density (ρ_c) relations for anisotropic neutron stars with $-2 \leq \tau \leq 2$ using the BSk19 EoS. Filled circles mark configurations where $\partial M/\partial\rho_c = 0$. Asterisks indicate the maximum ρ_c for which $v_{sr} \leq 0.95$ throughout the star. Filled squares and triangles denote the central densities up to which $v_{st} \leq 0.95$ and $v_{st} \geq 0$ conditions are satisfied, respectively.

Fig. 3.4, restricting to those stellar configurations that satisfy all four stability conditions discussed earlier. In both figures, alongside the mass-radius curves, we display the observed mass intervals for PSR J2045+3633 [128] and PSR J0952−0607 [129], which represent a low-mass (1.252 ± 0.021 $M_\odot$) and a high-mass (2.35 ± 0.17 $M_\odot$) neutron star, respectively. We also show the mass band for the secondary component of GW190814 [25], whose gravitational wave inferred mass lies in the range 2.50–2.67 $M_\odot$ (90% credible interval). This object falls within the so-called 'mass gap', suggesting that it may either be an exceptionally massive neutron star or a low-mass black hole.

It is observed that, for a suitable range of the anisotropic strength, the BSk21 EoS allows the formation of neutron stars massive enough to be consistent with all three observational constraints. In contrast, the BSk19 EoS fails to produce stellar configurations with masses exceeding 2.1 $M_\odot$. Consequently, we adopt BSk21 EoS as our primary choice, although a softer EoS such as BSk19 cannot be definitively excluded. This is particularly relevant given the possibility that adopting a different anisotropy ansatz might enable the formation of neutron stars with masses above 2.1 $M_\odot$ even when using the BSk19 EoS.

It should be emphasized that all computations presented here, including the construction of stellar structures by solving the modified TOV equations (as detailed in this section) and the analysis of f-mode oscillations (to be discussed in the next two sections), are performed under the static limit, i.e., assuming non-rotating stars. Therefore, we do not include the region typically excluded by the so-called 'mass-shedding limit' that applies to low-mass, rapidly rotating neutron stars. Nevertheless, it is well-established that most observed neutron stars are fast rotators. Specifically, PSR J2045+3633 and PSR J0952−0607 exhibit spin frequencies of 31.56 Hz [128] and 707.31 Hz [130], respectively. Such high spin rates rule out the existence of low-mass neutron stars ($\lesssim 0.5$ $M_\odot$), which would be disrupted by centrifugal effects.

The use of the static configuration does not affect the stellar structure significantly for the neutron stars of high masses. As an example, Bagchi [131] showed that the maximum

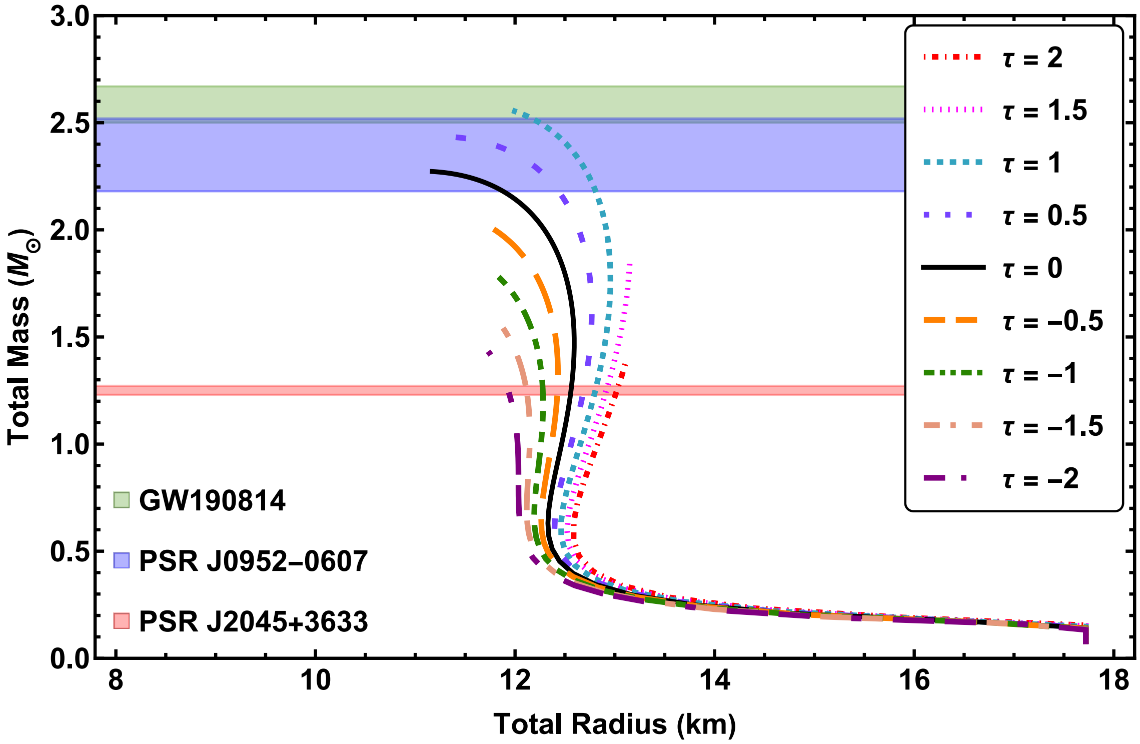

Figure 3.3: Mass-Radius profiles for anisotropic stable neutron stars with $-2 \leq \tau \leq 2$ and BSk21 EoS.

mass for a stable, non-rotating isotropic neutron star with APR EoS is 2.19 $M_\odot$ whereas the maximum mass for a stable isotropic neutron stars rotating with a spin frequency of 796 Hz (with APR EoS) is 2.20 $M_\odot$. This justifies our choice of studying even anisotropic neutron stars in the static limit. It will be interesting to study both the stellar structure and the f-mode oscillations of anisotropic neutron stars under full general relativistic framework including the rotation, in the future.

In Figure 3.5, we plot the radial coordinate (in km) inside the neutron star along the abscissa, and the corresponding enclosed mass in the unit of solar mass along the ordinate for BSk21 EoS. Various curves in this figure represent different values of τ, while the value of ρ_c is taken as 7.2955×10^{14} g cm^{-3} for all of the cases. This is the central density that gives a stable neutron star of a mass of $M = 1.4\ M_\odot$ for $\tau = 0$. However, this particular value of ρ_c gives stable neutron stars only in the range of $-1 \leq \tau \leq 1$. In particular, for $\tau = -1.0, -0.5, 0.5, 1.0$, we get neutron stars of mass 1.18 $M_\odot$, 1.28 $M_\odot$, 1.53 $M_\odot$, and 1.69 $M_\odot$, respectively, for $\rho_c = 7.2955 \times 10^{14}$ g cm^{-3}. Hence, whenever we

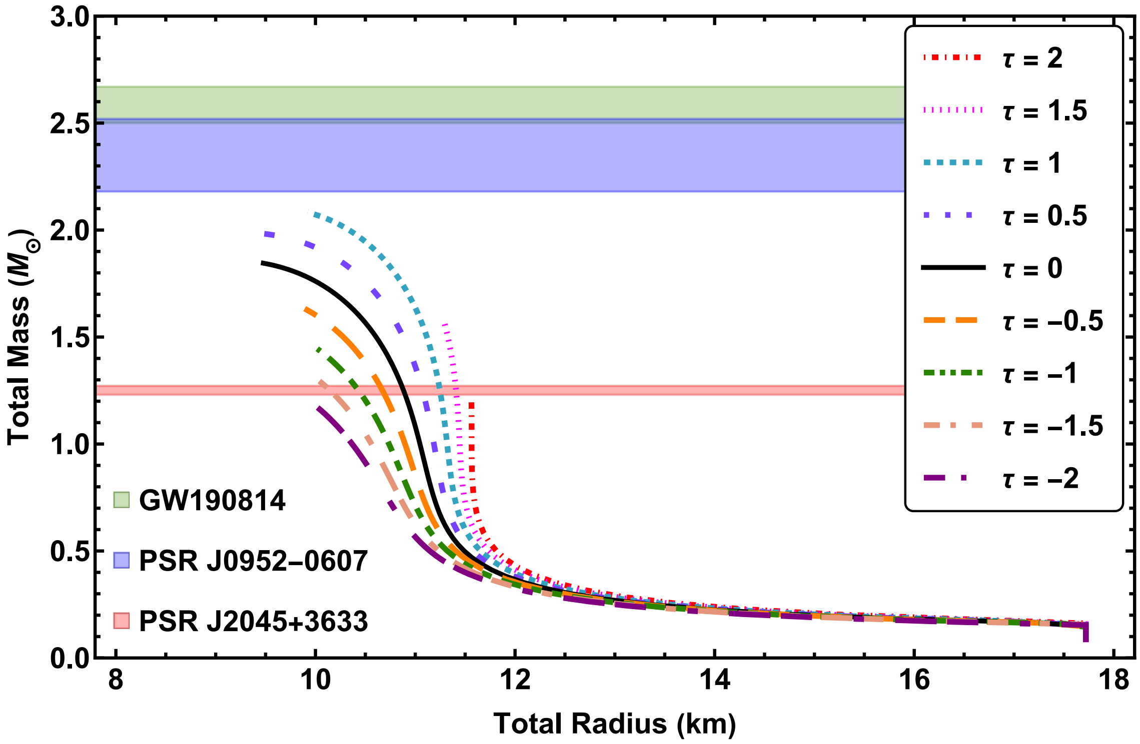

Figure 3.4: Mass-Radius profiles for anisotropic neutron stars with $-2 \leq \tau \leq 2$ and BSk19 EoS.

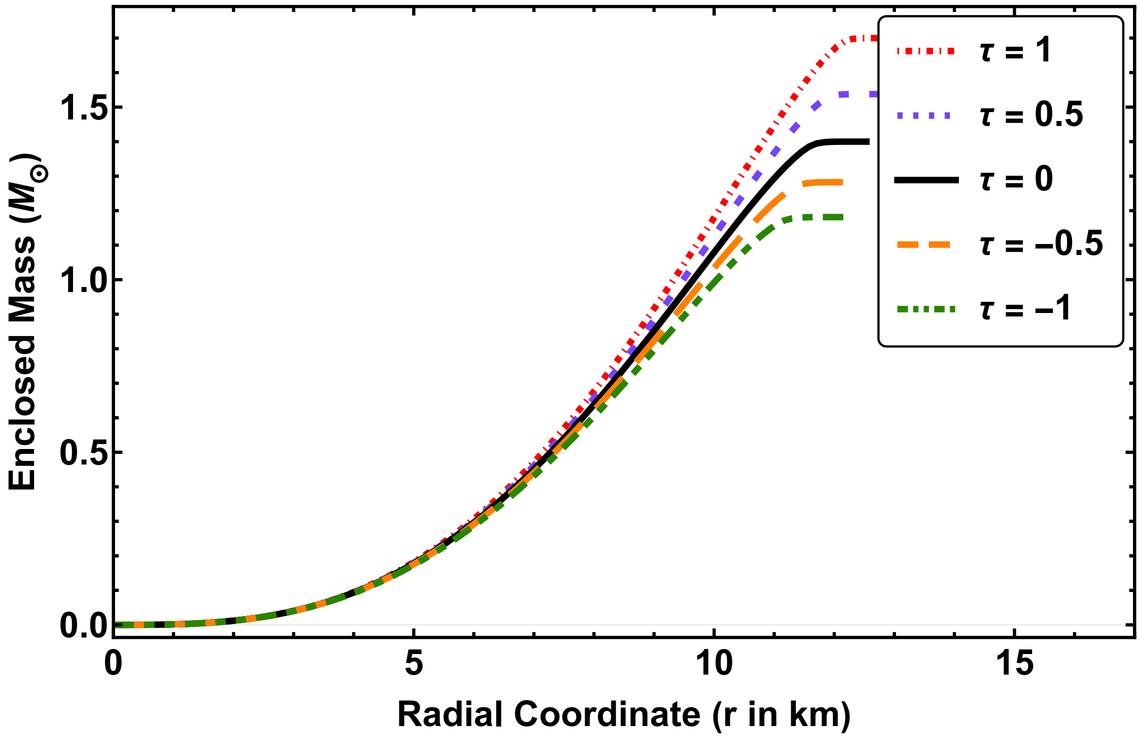

Figure 3.5: Radial profiles of enclosed mass for neutron stars with $\rho_c = 7.2955 \times 10^{14}\ \mathrm{g\,cm^{-3}}$, computed using the BSk21 EoS, for different values of the anisotropic strength τ.

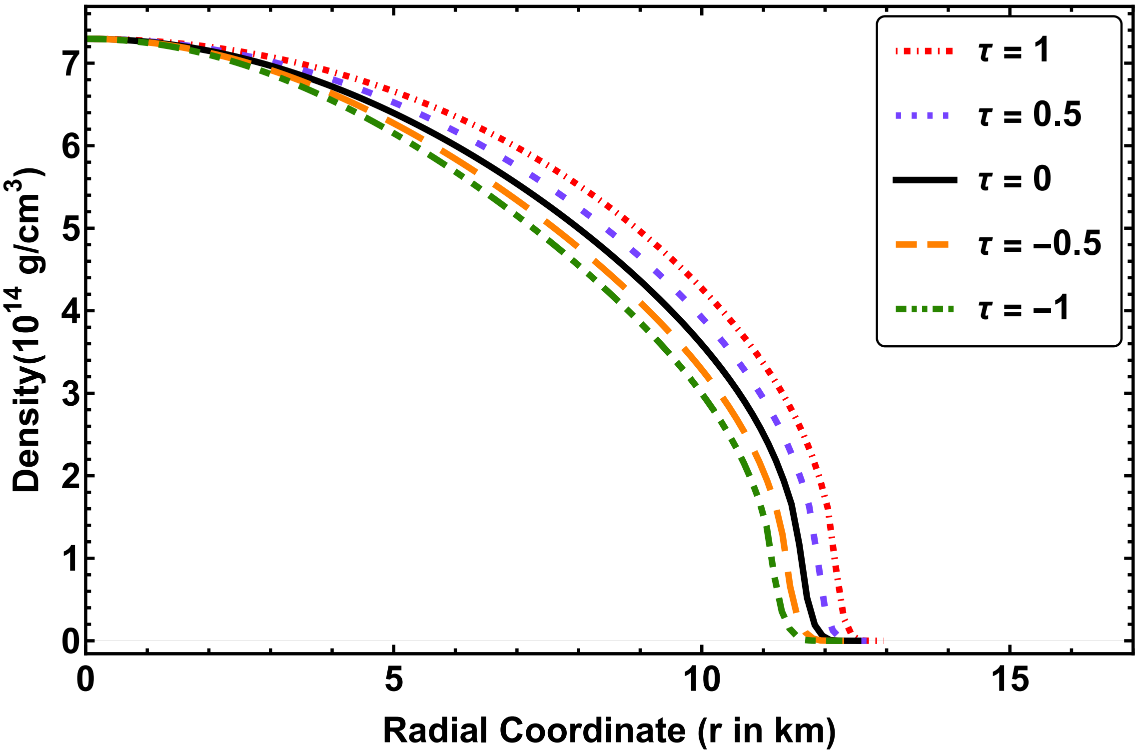

Figure 3.6: Density profiles with radius of neutron stars with central density $\rho_c = 7.2955 \times 10^{14}\ \mathrm{g\,cm^{-3}}$, computed using the BSk21 EoS, for various values of the anisotropic strength τ.

choose $\rho_c = 7.2955 \times 10^{14}\ \mathrm{g\,cm^{-3}}$, we restrict ourselves in the range of $-1 \leq \tau \leq 1$.

In Fig. 3.6, we plot the radial coordinate (in km) inside the neutron star along the horizontal axis and the corresponding density in $10^{14}\ \mathrm{g\,cm^{-3}}$ along the vertical axis, for BSk21 EoS and different values of τ, each with $\rho_c = 7.2955 \times 10^{14}\ \mathrm{g\,cm^{-3}}$ (the point where all the curves meet on the vertical axis). We see that for each of the cases, the density consistently decreases as the radial coordinate increases and eventually becomes almost zero at the surface of the star.

In Fig. 3.7, we plot the radial coordinate (in km) inside the neutron star along the abscissa and the corresponding pressure along the ordinate for BSk21 EoS and different values of τ. The left panel of the figure has the radial pressure along the ordinate while the right panel has the tangential pressure along the ordinate for the same values of τ. Both of the plots are for $\rho_c = 7.2955 \times 10^{14}\ \mathrm{g\,cm^{-3}}$. We see that for all values of τ, both p_r and p_t decreases monotonically with the increase of r and ultimately reaches zero at the surface of the star.

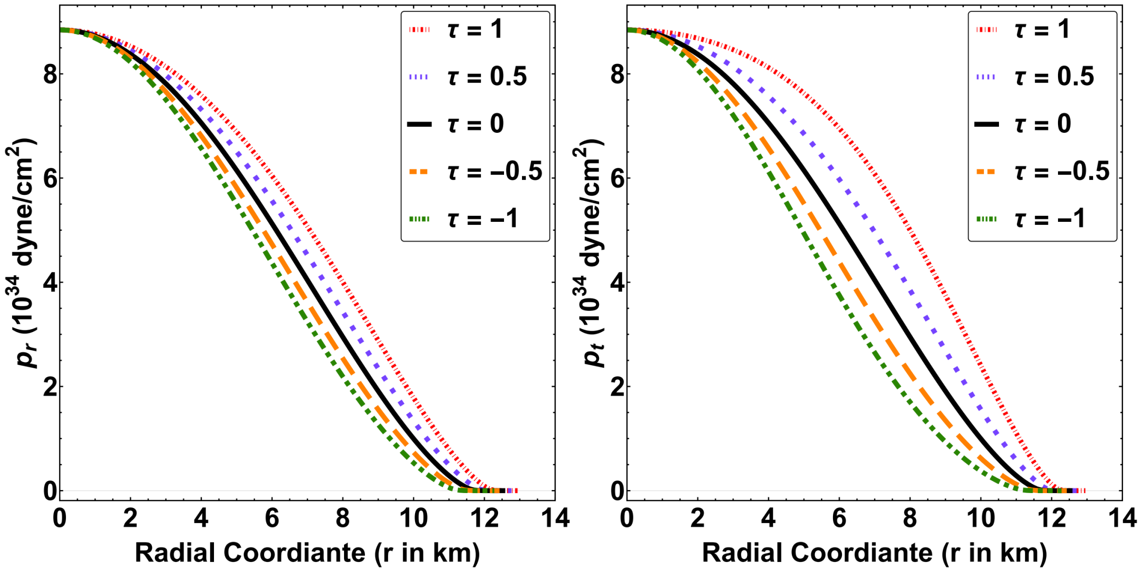

Figure 3.7: Variation of the radial pressure (left panel) and tangential pressure (right panel) inside neutron stars for different values of the anisotropic strength τ, computed for a central density of $\rho_c = 7.2955 \times 10^{14}\ \mathrm{g\,cm^{-3}}$ using the BSk21 EoS.

3.3.4 Equations of State of Quark Star

3.3.4.1 Noninteracting Quark Matter

The simplest EoS for quark stars is provided by the MIT bag model. In this framework, all three flavors of quarks (up, down, and strange quarks) are treated as non-interacting particles confined within a hypothetical bag. The radial pressure in this model is expressed as

$$p_r = -B + \sum_{i=u,d,s} p^i, \tag{3.23}$$

where p^i denotes the pressure contribution from each quark flavor, counterbalanced by the total external bag pressure B.

The total energy density ρ of the deconfined quarks inside the bag is given by

$$\rho = \sum_{i=u,d,s} \rho^i + B, \tag{3.24}$$

where $\rho^i = 3p^i$ represents the energy density of each quark flavor. Substituting this into the pressure equation, the EoS for quark matter can be simplified and written as

$$p_r = \frac{1}{3}(\rho - 4B). \tag{3.25}$$

In this study, the bag constant is fixed at $B = 56\ \mathrm{MeV\,fm^{-3}}$, ensuring consistency with prior works [132, 133, 86].

3.3.4.2 Interacting Quark Matter

A family of alternative EsoS for strange quark matter is given by Dey et al. [134], later improved by Bagchi et al. [135]. These EsoS are derived using a relativistic Hartree-Fock calculation for strange quark matter, incorporating a modified version of the phenomenological inter-quark interaction known as the Richardson potential [136]. The modified Richardson potential is given by

$$\begin{aligned} V_{ij} =& \frac{12\pi}{7}\left[\frac{1}{\ln\left(1+\frac{(\mathbf{k_i}-\mathbf{k_j})^2}{\Lambda}\right)} - \frac{\Lambda^2}{(\mathbf{k_i}-\mathbf{k_j})^2} + \frac{\Lambda'^2}{(\mathbf{k_i}-\mathbf{k_j})^2}\right] \\ & \times \frac{1}{(\mathbf{k_i}-\mathbf{k_j})^2}, \end{aligned} \tag{3.26}$$

where Λ and Λ' characterize the asymptotic freedom and confinement properties, respectively, and $(\mathbf{k_i}-\mathbf{k_j})$ represents the momentum transfer between the i-th and the j-th quarks. Applying the same potential in the baryonic sector [137, 138], it was found that the realistic values of Λ' can be taken in the range of 300 to 350 MeV, while the value of Λ is better fixed at 100 MeV.

In a medium, this bare potential undergoes screening due to pair creation and infrared divergence. As a result, $(\mathbf{k_i}-\mathbf{k_j})^2$ in Eq. (3.26) is replaced by $[(\mathbf{k_i}-\mathbf{k_j})^2 + D^{-2}]$, where D denotes the screening length. The inverse screening length (D^{-1}) is expressed at zero temperature to the lowest order as

$$(D^{-1})^2 = \frac{2\alpha_0}{\pi} \sum_{i=u,d,s} k_i^f \sqrt{\left(k_i^f\right)^2 + \mathcal{M}_{\mathrm{cur},i}^2}\,, \tag{3.27}$$

where k_i^f is the Fermi momentum of the i quark, $\mathcal{M}_{\mathrm{cur},i}$ is the current mass of the i quark, and α_0 is the perturbative quark-gluon coupling.

This model accounts for chiral symmetry restoration at high densities by considering the density-dependent quark mass $\mathcal{M}_i$, which decreases with increasing density as follows

$$\mathcal{M}_i = \mathcal{M}_{\mathrm{cur},i} + \mathcal{M}_Q \operatorname{sech}\left(\frac{n_B}{Nn_0}\right), \quad \text{for } i = u, d, s, \tag{3.28}$$

where $n_B = (n_u + n_d + n_s)/3$ is the baryon number density, $n_0 = 0.17\ \mathrm{fm}^{-3}$ is the nuclear matter saturation density, and n_u, n_d, and n_s denote the number densities of up, down, and strange quarks, respectively. The parameters $\mathcal{M}_Q$ and N are tuned to ensure that the minimum energy per baryon for strange quark matter remains below that of the most stable element, ^{56}Fe (930 MeV). This minimum energy per baryon is calculated at the surface of the star, where the radial pressure vanishes. The current quark masses are taken as $\mathcal{M}_{\mathrm{cur},u} = 4$ MeV, $\mathcal{M}_{\mathrm{cur},d} = 7$ MeV, and $\mathcal{M}_{\mathrm{cur},s} = 150$ MeV.

To maintain the charge neutrality of the matter, some electrons also need to be present. While the Fermi momenta (k_i^f) of the i-th quark is related to its number density (n_i) as $k_i^f = (n_i\pi^2)^{1/3}$, the relation between the Fermi momentum and number density of the electron is $k_e^f = (3n_e\pi^2)^{1/3}$. The values of Fermi momenta and chemical potentials of various particles are obtained in such a way that the charge neutrality and beta equilibrium conditions are satisfied throughout the matter. Then, using the laws of thermodynamics, the radial pressure p_r for various values of the density ρ, i.e., the EoS, is obtained. Different values of the model parameters Λ, α_0, $\mathcal{M}_Q$, and N give different EsoS. Out of various EsoS given by Bagchi et al. [135], we use EOS-A in the present work. EOS-A corresponds to $\Lambda' = 350$ MeV, $N = 3.0$, $\alpha_0 = 0.55$, and $\mathcal{M}_Q = 325$ MeV.

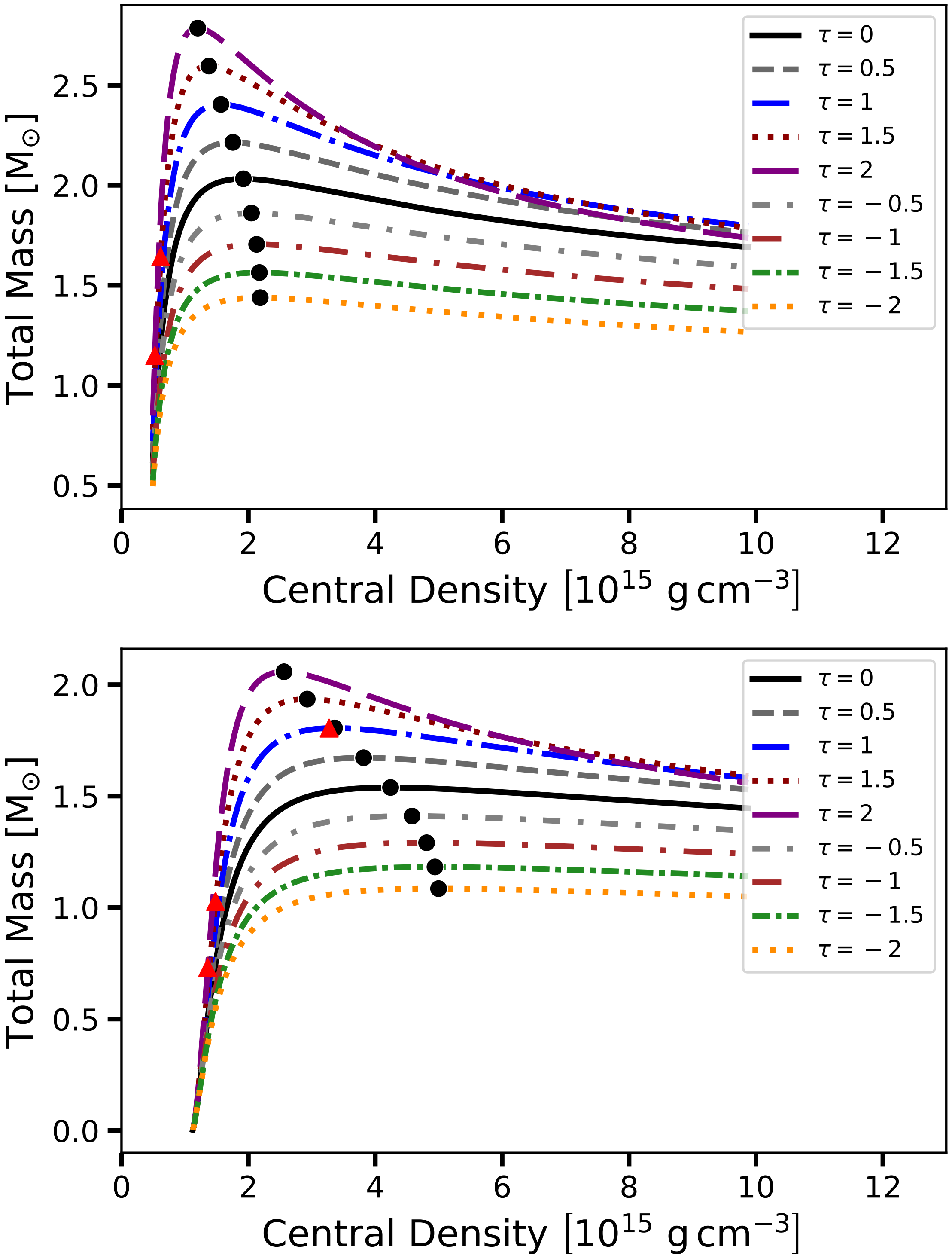

Figure 3.8: Mass (M)–central density (ρ_c) profiles for anisotropic quark stars with $-2 \leq \tau \leq 2$, using the MIT bag EoS (top panel) and EOS-A (bottom panel). Filled circles mark the points where $\partial M/\partial\rho_c = 0$, while red filled triangles denote the maximum values of ρ_c for which $v_{st} \geq 0$ is satisfied throughout the star.

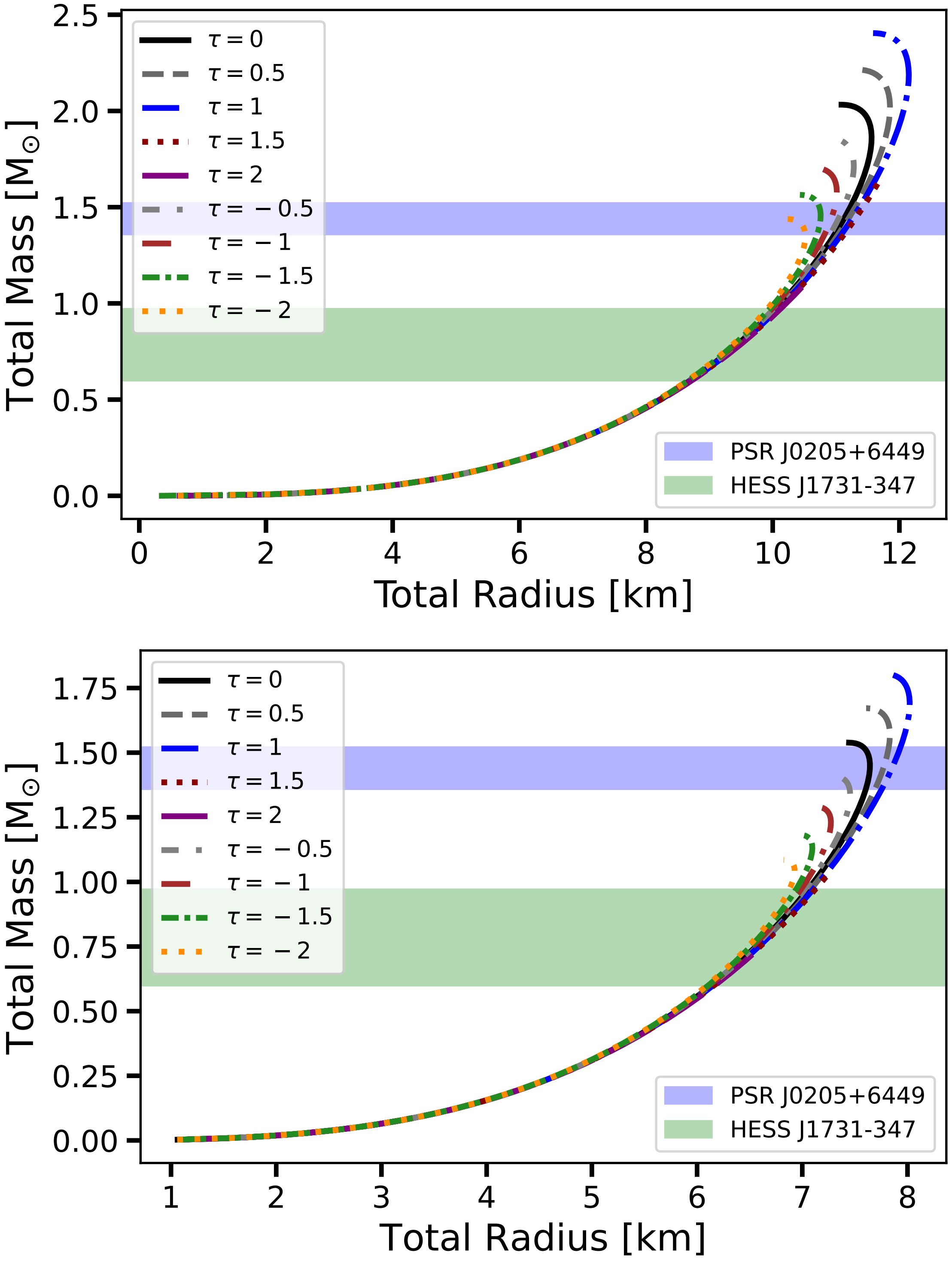

Figure 3.9: Mass–radius profiles for stable anisotropic quark stars with $-2 \leq \tau \leq 2$, using the MIT bag EoS (top panel) and EOS-A (bottom panel). The horizontal shaded bands represent the observationally inferred mass ranges of two compact star candidates: the blue band corresponds to PSR J0205+6449 $(1.36, 1.52\ \mathrm{M}_\odot)$ [1], and the green band corresponds to the central object in the supernova remnant HESS J1731−347 $(0.60, 0.97\ \mathrm{M}_\odot)$ [2].

As seen in the case of neutron stars, Fig. 3.8 reveals that an increase in tangential pressure relative to radial pressure ($\tau > 0$) leads to a higher enclosed mass for a fixed central density, whereas a reduction in tangential pressure ($\tau < 0$) results in a lower enclosed mass. However, once the stability criteria discussed in Sec. 3.3.2 are taken into account, we find that the maximum stable mass decreases for $\tau > 1$ for both the MIT bag EoS and EOS-A. For instance, within the MIT bag model, the maximum mass of a stable anisotropic quark star reaches approximately 2.45 $\mathrm{M}_{\odot}$ at $\tau = 1$, while for EOS-A, the corresponding value is around 1.75 $\mathrm{M}_{\odot}$, also at $\tau = 1$. In Fig. 3.9, we show the mass, radius relations for stable configurations, where each curve corresponds to a fixed value of the anisotropic strength τ.

To conclude, this chapter has developed a comprehensive treatment of the equilibrium structure of compact stars incorporating pressure anisotropy within the general relativistic framework. We formulated the governing field equations, introduced a well-motivated ansatz to describe anisotropy, and analyzed how variations in the anisotropic strength influence the mass, radius, and internal matter distributions of neutron stars and quark stars. Using multiple realistic equations of state, we explored the resulting structural differences and applied several stability conditions to identify physically viable configurations. Additionally, we compared our findings with existing observational mass constraints, illustrating how pressure anisotropy can significantly affect the macroscopic characteristics of compact stars. These insights provide the foundation for the following chapter, where we explore how such anisotropic pressure influences the fundamental f-mode oscillations and associated damping times.

Chapter 4

Perturbation of Anisotropic Compact Stars in General Relativity

4.1 Linear Perturbation of Compact Stars

In order to investigate the impact of pressure anisotropy on the non-radial oscillations of compact stars, this chapter develops the full general relativistic perturbation formalism which will later be used to compute the oscillation spectra.

Having described the equilibrium structure of compact stars in general relativity, we now present the theoretical framework for studying their linear order perturbations in full general relativity. Since Einstein's field equations govern the equilibrium configuration, we begin by perturbing these equations. The linearized Einstein field equations take the form:

$$\delta G^{\beta}{}_{\alpha} = 8\pi \delta T^{\beta}{}_{\alpha}, \tag{4.1}$$

where $\delta G^{\beta}{}_{\alpha}$ and $\delta T^{\beta}{}_{\alpha}$ represent the first-order perturbations of the Einstein tensor and the energy-momentum tensor, respectively. We first describe the perturbation of the geometrical part of the field equations (the left-hand side) and then address the perturbation of the energy-momentum tensor (the right-hand side), ultimately combining both to derive the perturbation equations of the relativistic stellar structure.

4.1.1 Perturbation of the Spacetime Geometry

Since the Einstein tensor is entirely determined by the spacetime metric and its derivatives, we begin by introducing a perturbation to the metric itself. Let $g^{(B)}_{\alpha\beta}$ represent the unperturbed background metric, and let $h_{\alpha\beta}$ denote the linear-order perturbation. Then, the total metric can be expressed as

$$g_{\alpha\beta} = g^{(B)}_{\alpha\beta} + h_{\alpha\beta}\,. \tag{4.2}$$

As the background spacetime is spherically symmetric, it is convenient to expand $h_{\alpha\beta}$ in terms of tensor spherical harmonics. These involve scalar spherical harmonics $Y_l^m(\theta, \phi)$ and their angular derivatives (forming vector and tensor harmonics, as outlined in Appendix A), multiplied by time and radius-dependent amplitude functions. Such perturbations also induce corresponding changes in the curvature tensors.

The interaction between the perturbed geometry and matter is governed by the linearized Einstein equations, expressed in Eq. (4.1). The expression for the first-order (linear) perturbation of the Einstein tensor, $\delta G_{\mu\nu}$, is given by [139]:

$$\begin{aligned} \delta G_{\mu\nu} = -\frac{1}{2}[\nabla^{\alpha}\nabla_{\alpha}h_{\mu\nu} - (\nabla_{\nu}f_{\mu} + \nabla_{\mu}f_{\nu}) + 2\mathcal{R}^{\alpha}{}_{\mu}{}^{\beta}{}_{\nu}h_{\alpha\beta} + \nabla_{\nu}\nabla_{\mu}h^{\alpha}{}_{\alpha} \\ -(\mathcal{R}^{\alpha}{}_{\nu}h_{\mu\alpha} + \mathcal{R}^{\alpha}{}_{\mu}h_{\nu\alpha}) + g^{(B)}_{\mu\nu}(\nabla^{\alpha}f_{\alpha} + \nabla^{\beta}\nabla_{\beta}h^{\alpha}{}_{\alpha}) + \mathcal{R}h_{\mu\nu} - g^{(B)}_{\mu\nu}\mathcal{R}^{\alpha\beta}h_{\alpha\beta}], \end{aligned} \tag{4.3}$$

where $f_{\nu} = \nabla^{\beta}h_{\nu\beta}$, and $\mathcal{R}_{\alpha\beta\gamma\delta}$, $\mathcal{R}_{\alpha\beta}$, and $\mathcal{R}$ denote the Riemann tensor, Ricci tensor, and Ricci scalar of the background geometry, respectively. The operator ∇_{σ} represents the covariant derivative with respect to the coordinate x^{σ}.

To simplify the analysis, we employ the Regge–Wheeler gauge, which separates the metric perturbations by parity and allows the perturbation equations to be written in a tractable form. The formalism of this gauge is summarized in Appendix A. In this work, we focus exclusively on even-parity (polar-type) perturbations for fixed spherical harmonic indices l and m. Within this gauge, the even-parity part of the metric perturbation is given by [140]:

$$h_{\alpha\beta} = -r^l \begin{pmatrix} e^{\nu} H_0(r) & i\omega r H_1(r) & 0 & 0 \\ i\omega r H_1(r) & e^{\lambda} H_2(r) & 0 & 0 \\ 0 & 0 & r^2 K(r) & 0 \\ 0 & 0 & 0 & r^2 \sin^2\theta K(r) \end{pmatrix} Y_l^m(\theta, \phi) e^{i\omega t} , \tag{4.4}$$

where $H_0(r)$, $H_1(r)$, $H_2(r)$, and $K(r)$ are functions of the radial coordinate r, and ω denotes the angular frequency of the oscillation.

Further simplification is achieved by examining the difference between the $(\theta\theta)$ and $(\phi\phi)$ components of the perturbed Einstein equations:

$$\begin{aligned} \delta(G^2{}_2 - G^3{}_3) &= 8\pi\, \delta(T^2{}_2 - T^3{}_3) \\ &= 8\pi(\delta p_t - \delta p_t) = 0 , \end{aligned} \tag{4.5}$$

where we have used that the background energy-momentum tensor is diagonal with equal tangential pressures, i.e., $T^{\beta}_{\ \alpha} = \mathrm{diag}(-\rho, p_r, p_t, p_t)$. The right-hand side thus vanishes identically. To compute the left-hand side, we substitute the metric perturbation form into Eq. (4.3). Upon evaluating the difference, $(\delta G^2{}_2 - \delta G^3{}_3)$, we find that this component of the perturbed Einstein tensor vanishes if and only if $H_0(r) = H_2(r)$. Accordingly, we define a new function $H(r)$ such that $H_0(r) = H_2(r) \equiv H(r)$ for the rest of the analysis.

4.1.2 Perturbation of the Energy-Momentum Tensor

In this section, we formulate the perturbation of the energy-momentum tensor, which appears on the right-hand side of Eq. (4.1). In the linear theory of perturbations, two standard approaches are used: the Eulerian and the Lagrangian formalisms. The details of these methods, along with their interrelation, are outlined in Appendix B. The Lagrangian and Eulerian perturbations are related through the following identity (see Appendix B):

$$\Delta = \delta + \mathcal{L}_{\xi}, \tag{4.6}$$

where δ denotes the Eulerian variation and $\mathcal{L}_{\xi}$ is the Lie derivative along the displacement vector ξ^{α}.

The perturbation of the stellar fluid is characterized by the Lagrangian displacement vector ξ^{α}, whose components are given by [141, 109, 83]:

$$\xi^{\mu} = \begin{pmatrix} 0 \\ r^{l-1}\, e^{-\lambda/2} W(r) \\ -r^{l-2}\, V(r)\, \partial_{\theta} \\ -\dfrac{r^{l-2}}{\sin^2\theta}\, V(r)\, \partial_{\phi} \end{pmatrix} Y_l^m(\theta, \phi)\, e^{i\omega t}, \tag{4.7}$$

where $W(r)$ and $V(r)$ are the radial functions associated with the fluid perturbations. This displacement vector will be used extensively to derive the perturbed components of the energy-momentum tensor.

By perturbing the normalisation condition of 4-velocity, i.e. Eq. (3.12a), we can calculate the Lagrangian variation of the four-velocity u^{μ}, which is given by [142]:

$$\Delta u^{\mu} = \frac{1}{2} u^{\mu} u^{\nu} u^{\sigma} \Delta g_{\nu\sigma}, \tag{4.8}$$

where $\Delta g_{\alpha\beta}$ is the Lagrangian variation of the metric tensor. Using Eq. (4.6), we can show that $\Delta g_{\alpha\beta}$ is related to Eulerian variation of metric tensor ($\delta g_{\alpha\beta} = h_{\alpha\beta}$) as:

$$\Delta g_{\alpha\beta} = h_{\alpha\beta} + \nabla_\alpha \xi_\beta + \nabla_\beta \xi_\alpha \ . \tag{4.9}$$

Using Eqs. (4.6), (4.8), and (4.9), the Eulerian variation of the four-velocity can be expressed as

$$\delta u^\mu = \left(\delta^\mu{}_\rho + u^\mu u_\rho\right)(u^\sigma \nabla_\sigma \xi^\rho - \xi^\sigma \nabla_\sigma u^\rho) + \frac{1}{2} u^\mu u^\sigma u^\rho h_{\sigma\rho}. \tag{4.10}$$

After substituting the expressions of u^σ, ξ^σ and $h_{\alpha\beta}$ to Eq. (4.10), we get

$$\delta u^\sigma = \begin{pmatrix} -\frac{H}{2} \\ i\omega r^{-1}\, e^{-\lambda/2} W(r) \\ -i\omega r^{-2}\, V(r)\partial_\theta \\ -i\omega (r\sin\theta)^{-2}\, V(r)\partial_\phi \end{pmatrix} r^l e^{-\nu/2} Y_l^m(\theta,\phi) e^{i\omega t}. \tag{4.11}$$

We also expand the perturbation of the radial unit vector, s^μ, in harmonics as follows:

$$\delta s^\sigma = \begin{pmatrix} i\omega S_0(r) \\ S_1(r) \\ 0 \\ 0 \end{pmatrix} r^l\, Y_l^m(\theta,\phi)\, e^{i\omega t}, \tag{4.12}$$

where $S_0(r)$ and $S_1(r)$ are two functions of the radial coordinates, which we need to determine. For the sake of brevity, we will drop the independent variables (coordinates) from the functions for the rest of the thesis, i.e., instead of $H(r)$, $H_1(r)$, $K(r)$, $W(r)$, $V(r)$, $S_0(r)$, $S_1(r)$, and $Y_l^m(\theta,\phi)$, we will simply write H, H_1, K, W, V, S_0, S_1, and Y_l^m, respectively.

As s^σ is a unit radial vector orthogonal to the fluid flow, its normalization and orthogonality conditions should hold up to linear order. This requires that $\delta s^\sigma s_\sigma + s^\sigma \delta s_\sigma = 0$ and

$\delta s^\sigma u_\sigma + s^\sigma \delta u_\sigma = 0$. These constraints yield the following expressions for S_0 and S_1:

$$S_0 = \frac{e^{-\nu}}{r} W - e^{-(\nu+\lambda/2)}\, r\, H_1 \,, \tag{4.13}$$

$$S_1 = \frac{e^{-\lambda/2}}{2} H \,. \tag{4.14}$$

To derive the perturbations in energy density and pressures, we must first evaluate the variation in the particle number density. The Lagrangian perturbation in number density, Δn, can be obtained using the conservation law $\nabla_\alpha n^\alpha = 0$, where $n^\alpha = n u^\alpha$, and n is the number density of particles[1]. The Lagrangian perturbation is given by [142, 143]

$$\Delta n = -\frac{1}{2} n \perp^{\mu\nu} \Delta g_{\mu\nu} \,, \tag{4.15}$$

where $\perp^{\mu\nu}$ is the projection tensor orthogonal to u^μ, defined as

$$\perp^{\mu\nu} = u^\mu u^\nu + g^{\mu\nu} \,. \tag{4.16}$$

After evaluating the contractions and simplifying the result, one obtains

$$\Delta n = -\frac{1}{2} n \perp_g Y_l^m e^{i\omega t} \,, \tag{4.17}$$

where the function $\perp_g$ is given by

$$\perp_g = -2r^l \left[\left(K + \frac{1}{2} H \right) - \frac{l(l+1)}{r^2} V - \frac{e^{-\lambda/2}}{r} W' - \left(\frac{l+1}{r^2} e^{-\lambda/2} \right) W \right] , \tag{4.18}$$

which agrees with the form found in [85].

We now follow the assumptions outlined in [80, 82]: (i) There is no structural anisotropy

---

[1] In some studies [75], anisotropic modifications of number density are introduced using linear components n_1, n_2, and n_3 such that $n = n_1 n_2 n_3$, with n being the volume number density. A further simplification often used is $n_1 = n_r$ and $n_2 = n_3 = n_t$, where n_r and n_t represent the linear number densities along the radial and tangential directions. In this work, however, we do not incorporate anisotropy in the number density.

in the stellar interior, implying the Lagrangian variation of the strain tensor vanishes. While this condition might break down in presence of magnetic fields or rotational effects, it holds in the present context. (ii) The work done within an infinitesimal fluid element is given by $p_{\rm avg}\, dV$, where $p_{\rm avg}$ denotes the pressure averaged over all directions. (iii) The matter is barotropic, i.e., the energy density ρ depends only on the number density, $\rho = \rho(n)$. Under these assumptions, we can write the Lagrangian perturbation of the energy density as

$$\Delta\rho = \frac{d\rho}{dn}\Delta n = \kappa\,\Delta n\,, \tag{4.19}$$

where $\kappa = \frac{d\rho}{dn}$ is the chemical potential. Furthermore, the Gibbs relation provides a useful identity [142]:

$$\rho + p_{\rm avg} = \kappa n\,, \tag{4.20}$$

where the averaged pressure is defined as [144]

$$p_{\rm avg} = \frac{1}{3}\left(T^1{}_1 + T^2{}_2 + T^3{}_3\right) = \frac{p_r + 2p_t}{3} = p_r + \frac{2}{3}\chi\,. \tag{4.21}$$

Although $p_{\rm avg}$ depends on r, for notational simplicity we continue to write $p_{\rm avg}$ instead of $p_{\rm avg}(r)$. Note that, additional terms would appear in Eq. (4.20) if structural anisotropy were included [145, 146].

Substituting Eq. (4.17) into Eq. (4.19) and using the Gibbs relation, we obtain

$$\Delta\rho = -\frac{1}{2}(p_{\rm avg} + \rho)\perp_g\; Y_l^m e^{i\omega t}\,. \tag{4.22}$$

The Lagrangian variation of the radial pressure follows as

$$\Delta p_r = \frac{dp_r}{d\rho}\Delta\rho = -\frac{1}{2}\frac{dp_r}{d\rho}(p_{\rm avg} + \rho)\perp_g\; Y_l^m e^{i\omega t}\,. \tag{4.23}$$

By defining the radial sound speed as $v_{sr}^2 = \frac{\partial p_r}{\partial\rho} = \frac{dp_r}{d\rho}$, as in Sec. 3.3.2, we can express

Eq. (4.23) in a more compact form:

$$\Delta p_r = -\frac{1}{2} v_{sr}^2 (p_{\text{avg}} + \rho) \perp_g \; Y_l^m e^{i\omega t} \, . \tag{4.24}$$

Using Eq. (4.6), we relate Lagrangian and Eulerian variations of the radial pressure:

$$\begin{aligned}
\Delta p_r &= \delta p_r + \xi^r \, p_r' \\
&= \delta p_r + r^{l-1} e^{-\lambda/2} \left[-\frac{\nu'}{2} (\rho + p_r) + \frac{2\chi}{r} \right] W \, Y_l^m e^{i\omega t} \, .
\end{aligned} \tag{4.25}$$

By combining Eqs. (4.23) and (4.25), we obtain the Eulerian variation of p_r, i.e., δp_r. From this, we further derive the Eulerian variations of energy density and tangential pressure:

$$\delta\rho = \frac{d\rho}{dp_r} \delta p_r \, , \tag{4.26}$$

$$\delta p_t = \delta p_r + \delta\chi \, . \tag{4.27}$$

These expressions enable us to compute the perturbed energy-momentum tensor components. The full expression is

$$\begin{aligned}
\delta T^{\beta}{}_{\alpha} &= (\delta\rho + \delta p_t) u^{\beta} u_{\alpha} + (\rho + p_t)(u^{\beta} \delta u_{\alpha} + \delta u^{\beta} u_{\alpha}) \\
&+ \delta^{\beta}{}_{\alpha} \delta p_t + (\delta p_r - \delta p_t) s^{\beta} s_{\alpha} + (p_r - p_t)(s^{\beta} \delta s_{\alpha} + \delta s^{\beta} s_{\alpha}) \, .
\end{aligned} \tag{4.28}$$

Substituting Eqs. (4.11), (4.12), and (4.28), along with the definitions of u^{β} and s^{β}, we obtain the non-zero components of $\delta T^{\beta}{}_{\alpha}$:

$$\delta T^{0}{}_{0} = -\delta\rho = -\delta\tilde{\rho}(r) \, r^l Y_l^m e^{i\omega t} \, , \tag{4.29a}$$

$$\delta T^{1}{}_{0} = -i\omega e^{-\lambda/2} r^{-1} (\rho + p_r) W r^l Y_l^m e^{i\omega t} \, , \tag{4.29b}$$

$$\delta T^{2}{}_{0} = i\omega r^{-2} (\rho + p_r + \chi) V r^l \partial_\theta Y_l^m e^{i\omega t} \, , \tag{4.29c}$$

$$\delta T^3_{\ 0} = i\omega r^{-2}(\rho + p_r + \chi) V r^l (\sin\theta)^{-2} \partial_\phi Y_l^m e^{i\omega t} \,, \tag{4.29d}$$

$$\delta T^1_{\ 1} = \delta p_r = \delta\tilde{p}_r(r)\, r^l Y_l^m e^{i\omega t} \,, \tag{4.29e}$$

$$\delta T^2_{\ 2} = \delta p_t = [\delta\tilde{p}_r(r) + \delta\tilde{\chi}(r)]\ r^l Y_l^m e^{i\omega t} \,, \tag{4.29f}$$

$$\delta T^3_{\ 3} = \delta p_t = [\delta\tilde{p}_r(r) + \delta\tilde{\chi}(r)]\ r^l Y_l^m e^{i\omega t} \,. \tag{4.29g}$$

Here, the radial, angular, and temporal dependencies of $\delta\rho$, δp_r, and $\delta\chi$ have been separated as follows: $\delta\rho = r^l \delta\tilde{\rho}(r) Y_l^m e^{i\omega t}$, $\delta p_r = r^l \delta\tilde{p}_r(r) Y_l^m e^{i\omega t}$, and $\delta\chi = r^l \delta\tilde{\chi}(r) Y_l^m e^{i\omega t}$. In the limit $\chi = 0$ and $\delta\chi = 0$, the above equations reduce to the isotropic case derived in [80].

We now proceed to derive the governing equations for non-radial oscillations of anisotropic compact stars by employing the linearized Einstein field equations, Eq. (4.1), along with the conservation of energy-momentum tensor up to linear order, $\delta(\nabla_\nu T^{\mu\nu}) = 0$. These equations yield the dynamics of both the metric perturbation variables (H, H_1, K) and the fluid perturbation variables (V, W). First, we perform a change of variable, which simplifies the boundary condition. We know that, at the surface of the star $(r = R)$, the Lagrangian perturbation of the radial pressure is zero, i.e., $\Delta p_r = 0$. We introduce a new variable X to write Δp_r in the form

$$\Delta p_r = -r^l e^{-\nu/2} X Y_l^m e^{i\omega t}. \tag{4.30}$$

This substitution enables us to write the perturbation equations in terms of X and conveniently impose the boundary condition $X(R) = 0$ in numerical integrations. Using the expressions from equations (4.18), (4.24), and (4.30), we write the expression of X, which is given by:

$$\begin{aligned} X = (\rho + p_{\text{avg}}) v_{sr}^2 \Big[&\frac{e^{\nu/2-\lambda/2}}{r} W' + \frac{(l+1) e^{\nu/2-\lambda/2}}{r^2} W \\ &+ \frac{l(l+1) e^{\nu/2}}{r^2} V - e^{\nu/2} K - \frac{e^{\nu/2}}{2} H \Big]. \end{aligned} \tag{4.31}$$

Using Eqs. (4.25) and (4.30), we can write the Eulerian perturbation of the radial pressure as:

$$\begin{aligned}\delta p_r = \delta\tilde{p}_r r^l Y_l^m e^{i\omega t} = \Big[- e^{-\nu/2} X + \frac{W}{2r^2} e^{-\lambda/2} \Big\{ -4\chi \\ + r\nu'(p_r+\rho) \Big\} \Big] r^l Y_l^m e^{i\omega t} \,. \end{aligned} \tag{4.32}$$

Noting that X is purely a function of r, we simplify notation and refer to it as X hereafter. Using this new variable X, we write the governing equations of oscillations as:

$$H_1' = \frac{e^\lambda}{r} H + \frac{e^\lambda}{r} K - \frac{(l+1) + 2mr^{-1}e^\lambda + 4\pi r^2 e^\lambda (p_r - \rho)}{r} H_1 - \frac{16\pi e^\lambda (\rho + p_r + \chi)}{r} V, \tag{4.33a}$$

$$K' = \frac{1}{r} H - \left[(l+1) r^{-1} - \frac{1}{2}\nu' \right] K + \frac{l(l+1)}{2r} H_1 - \frac{8\pi e^{\lambda/2}(p_r+\rho)}{r} W, \tag{4.33b}$$

$$W' = \frac{1}{2} e^{\lambda/2} r H + e^{\lambda/2} r K - \frac{e^{\lambda/2} l(l+1)}{r} V - \frac{(l+1)}{r} W + \frac{r e^{\frac{\lambda-\nu}{2}}}{v_{sr}^2 \left(p_r + \rho + \frac{2\chi}{3} \right)} X, \tag{4.33c}$$

$$\begin{aligned} X' = & -2\frac{e^{\nu/2}}{r}\delta\tilde{\chi} - \left[\frac{l}{r} + \frac{\chi(6+r\nu')}{r v_{sr}^2 (3(p_r+\rho)+2\chi)} \right] X + (p_r+\rho) e^{\nu/2} \left[\frac{1}{2r} - \frac{\nu'}{4} \right] H \\ & - \left[\frac{e^{\nu/2} l(l+1)(p_r+\rho)\nu'}{2r^2} - \chi \frac{2l(l+1)e^{\nu/2}}{r^3} \right] V \\ & + \left[\frac{e^{\nu/2}(p_r+\rho)}{2} \left(\frac{l(l+1)}{2r} + r\omega^2 e^{-\nu} \right) + \frac{\chi e^{\nu/2} l(l+1)}{2r} \right] H_1 \\ & + \left[\frac{1}{2} e^{\nu/2} (p_r+\rho) \left(\frac{3}{2}\nu' - \frac{1}{r} \right) + \chi \frac{e^{\nu/2}(-6+r\nu')}{2r} \right] K \\ & + \left[-\frac{e^{\nu/2}(p_r+\rho)}{r} \left(e^{\lambda/2-\nu}\omega^2 + 4\pi e^{\lambda/2}(p_r+\rho) - \frac{1}{2} r^2 (r^{-2} e^{-\lambda/2}\nu')' \right) \right. \\ & \left. -\chi' \frac{2e^{(\nu-\lambda)/2}}{r^2} + \frac{e^{(\nu+\lambda)/2}}{r^3} \chi \left(6 - 14mr^{-1} - 8\pi r^2 p_r \right) \right] W, \end{aligned} \tag{4.33d}$$

where H_1 and K were introduced in Eq. (4.4), W in Eq. (4.7), and X in Eq. (4.30). The remaining functions in Eq. (4.4) and (4.7), namely $H_0 = H_2 = H$ and V are related to other functions by following algebraic relations:

$$\left[3m+\frac{1}{2}(l-1)(l+2)r+4\pi r^3 p_r\right]H = 8\pi e^{-\nu/2}r^3X-\left[-e^{-\nu-\lambda}r^3\omega^2+\frac{1}{2}l(l+1)(m+4\pi r^3p_r)\right]H_1 \\ +\chi 16e^{-\lambda/2}\pi rW-\left[-\frac{1}{2}(l-1)(l+2)r+e^{-\nu}r^3\omega^2+\frac{e^\lambda}{r}(m+4\pi r^3p_r)(3m-r+4\pi r^3p_r)\right]K, \tag{4.34}$$

$$\omega^2(\rho+p_r+\chi)V = e^{\nu/2}X-\frac{1}{2}e^\nu(p_r+\rho)H+\frac{e^{\nu-\lambda/2}p_r'}{r}W-e^\nu\delta\tilde{\chi}\,. \tag{4.35}$$

These are the set of equations that govern the oscillations of anisotropic compact stars in general relativity. The equations for the metric perturbation dynamics, i.e., the equation for H_1' has been obtained from $\delta G^2{}_0 = 8\pi\delta T^2{}_0$ and the equation for K' has been obtained from $\delta G^1{}_0 = 8\pi\delta T^1{}_0$. The expressions for $\delta G^\mu{}_\nu$ are obtained by putting $h_{\mu\nu}$ from Eq. (4.4) in Eq. (4.3) and raising one index. The explicit expressions for $\delta T^\nu{}_\mu$ is given in Eq. (4.29). On the other hand, the dynamics of the fluid perturbations, which are given by W' and X', have been obtained with the help of Eq. (4.31) and $\delta(\nabla_\mu T^\mu{}_1) = 0$, respectively. Eq. (4.34), which relates the metric perturbation variable H to other variables, has been obtained by combining $\delta G^1{}_1 = 8\pi\delta T^1{}_1$ and $\delta G^2{}_1 = 8\pi\delta T^2{}_1$. Eq. (4.35) relates the fluid perturbation variable V to other variables and has been obtained from $\delta(\nabla_\mu T^\mu{}_2) = 0$. The effect of anisotropy is manifested in these equations through terms having χ, χ', and $\delta\chi$. These terms are zero in the isotropic case and our equations take the well known forms given by Detweiler and Lindblom [83].

For the anisotropy ansatz adopted in this work, the perturbation of the anisotropy parameter takes the following form,

$$\delta\chi = \frac{\partial\chi}{\partial p_r}\delta p_r+\frac{\partial\chi}{\partial\mu}\delta\mu\,. \tag{4.36}$$

Note that, unlike Cowling approximation, in our full general relativistic framework, the variable μ is perturbed. The quantity $\mu = 2m/r = 1-e^{-\lambda}$, which describes the local compactness of the star, can be perturbed as $\delta\mu = e^{-\lambda}\delta\lambda$, where $\delta\lambda$ represents the perturbation of λ. As we are interested up to the linear order perturbation, so from the perturbation of the metric, we can write

$$e^{\lambda+\delta\lambda} = e^{\lambda}(1 - Hr^{l}Y_{l}^{m}e^{i\omega t})\ . \tag{4.37}$$

Neglecting the higher order perturbation terms ($\mathrm{O}((\delta\lambda)^2)\ldots$), we can write

$$\delta\lambda = -Hr^{l}Y_{l}^{m}e^{i\omega t}\ . \tag{4.38}$$

Using Eqs. (3.21), (4.29e), and (4.38) in Eq. (4.36), we get

$$\delta\chi = \tau\left[\left(\frac{2m}{r}\right)\delta\tilde{p}_r - \left(p_r\left(1 - \frac{2m}{r}\right)H\right)\right]r^{l}Y_{l}^{m}e^{i\omega t}\ , \tag{4.39}$$

where $\delta\tilde{p}_r$ is given in equation (4.32).

To summarize, in this chapter we have developed the full general relativistic formalism for analyzing the polar-type quasinormal oscillations of anisotropic compact stars. Starting from the linearized Einstein field equations and the perturbed energy-momentum tensor, we derived a closed set of coupled differential equations governing the spacetime and fluid perturbations. The effects of anisotropy are incorporated in a covariant manner through the anisotropy parameter χ and its perturbation $\delta\chi$, which naturally vanish in the isotropic limit. The formalism derived here forms the basis for the numerical computation of f-mode frequencies and damping times of anisotropic neutron stars and quark stars. In the next chapter, we apply this framework to obtain and analyze the numerical results, and examine how pressure anisotropy influences the oscillation spectra of compact stars for various EosS.

Chapter 5

Numerical procedure and results for f-mode oscillations of neutron stars and quark stars

In this chapter, we aim to explore the impact of pressure anisotropy on the quasi-normal modes of compact stars using full general relativistic perturbation theory developed in the previous chapter.

We describe the numerical technique to solve the system of perturbation equations derived in the previous chapter. We also compute the fundamental (f-mode) oscillation frequencies and their corresponding damping times for both neutron stars and quark stars, and analyze the role of pressure anisotropy in modifying these quantities. Since our primary objective is to determine the quasi-normal modes, it is important to carefully consider the specific initial value and boundary value conditions. Unlike the background stellar configuration, which involves solving a simpler set of equations, the perturbation analysis entails integrating seven coupled first-order differential equations, three describing the equilibrium background and four governing the perturbations, alongside two additional algebraic relations. Inside the star, it is crucial to ensure that the equations remain regular at the center of the star, while the boundary condition dictates that the Lagrangian perturbation of the radial pressure (Δp_r) must be zero at the outermost surface of the perturbed star. By examining the set of equations in Eq. (4.33), we observe that they exhibit singularity at $r = 0$.

To ensure regularity at the center, we expand all the variables at a point $r = R/10^6$ as a Taylor series around $r = 0$. The variables for which we do such expansions include the variables that describe the unperturbed star, e.g., λ, ν, m, ρ, p_r, χ as well as the perturbation variables H, H_1, K, V, W, and X. We substitute these expansions into the equations that govern the unperturbed star (Eqs. (3.15), (3.18), (3.19)), as well as perturbation equations (Eqs. (4.33a), (4.33b), (4.33c), (4.33d), (4.34), and (4.35)) to derive the necessary conditions. The initial conditions are given by:

$$H_1(0) = \frac{1}{l(l+1)}\left[2lK(0) + 16\pi\left\{\rho(0) + p_r(0)\right\}W(0)\right], \tag{5.1}$$

$$\begin{aligned} X(0) = \{p_r(0) + \rho(0)\}\, e^{\nu(0)/2} \Bigg[\Bigg\{ & \frac{4\pi}{3}\{\rho(0) + 3p_r(0)\} \\ & -\frac{\omega^2 e^{-\nu(0)}}{l}\Bigg\} W(0) + \frac{1}{2}K(0)\Bigg] - e^{\nu(0)/2}\chi_2(0)W(0), \end{aligned} \tag{5.2}$$

where $\chi_2(0)$ is the second order in the expansion of $\chi(r)$ around $r = 0$. Here one has to keep in mind that, the leading order nonzero term in the expansion of χ is $\chi = (1/2)\chi_2(0)r^2$. Since the radial and the tangential pressures are equal at the center, we have $\chi(0) = \delta\chi(0) = 0$. This condition guarantees that at the center, the radial pressure is equal to the tangential pressure, and the Eulerian perturbation of the radial pressure is equal to the Eulerian perturbation of the tangential pressure. Based on our ansatz (Eq.(3.21)), we can express $\chi_2(0)$ as $\chi_2(0) = \tau\frac{16\pi}{3}\rho(0)p_r(0)$. From Eqs. (5.1) and (5.2), we see that $H_1(0)$ and $X(0)$ depend on two independent variables $K(0)$ and $W(0)$. These expressions exhibit similarity to those of the isotropic case described by Detweiler and Lindblom [83], with the addition of the term containing $\chi_2(0)$ that arises due to the presence of the anisotropy. Now, we need to set the values of $W(0)$ and $K(0)$ in such a way that after integrating

Eqs. (4.33a), (4.33b), (4.33c), and (4.33d) along with Eqs. (3.15), (3.18), (3.19), radially outward from the point $R/10^6$, we would get $X(R) = 0$. To do this, following Detweiler and Lindblom [83], we use two sets of values of $W(0)$ and $K(0)$, namely, $W(0) = 1$, $K(0) = +[\rho(0) + p_r(0)]$ and $W(0) = 1$, $K(0) = -[\rho(0) + p_r(0)]$. We perform outward integration with each of the sets independently and get two independent values of X at $r = R$, say X_+ and X_-. Then, we combine these two solutions as $X(R) = c_+X_+ + c_-X_-$ and choose the values of the coefficients c_+ and c_- to ensure $X(R) = 0$. For the integration process, we have employed the 'LSODA' [147, 148] method of integration, which dynamically switches between the BDF (Backward Differentiation Formula) method and the Adams method based on the stiffness of the coupled equations. In our implementation, we have set both the relative and the absolute tolerances to 10^{-10}. This completes the discussion on the integration inside the neutron star.

Outside the star, all the fluid perturbation variables become zero but the metric perturbation variables remain non-zero. This results in a reduction of the number of the equations to two, specifically, the equations for H_1' and K'. Following the standard technique, we perform another transformation of variables given by

$$r^l K = \frac{n_l(n_l+1)r^2 + 3n_lMr + 6M^2}{r^2(n_lr + 3M)} Z + \frac{dZ}{dr^*}, \tag{5.3}$$

$$r^{l+1} H_1 = \frac{n_lr^2 - 3n_lMr - 3M^2}{(r-2M)(n_lr + 3M)} Z + \frac{r^2}{(r-2M)} \frac{dZ}{dr^*}, \tag{5.4}$$

where $n_l = [l(l+1)/2] - 1$, and $r^* = r + 2M \ln[(r/2M) - 1]$. With these transformations, the differential equations for H_1' and K' can be combined into a single second order differential equation as:

$$\frac{d^2}{dr^{*2}} \{Z(r^*)\} + \left[\omega^2 - V_z(r^*)\right] Z(r^*) = 0, \tag{5.5}$$

where,

$$V_z(r^*) = \frac{(1 - 2M/r)}{r^3(n_lr + 3M)^2} \left[2n_l^2(n_l+1)r^3 + 6n_l^2Mr^2\right.$$

$$+18n_l M^2 r + 18M^3\Big] . \tag{5.6}$$

This equation was first derived by Zerilli [149] for perturbations of Schwarzschild black holes. The function $Z(r^*)$, referred to as the Zerilli function, encapsulates the dynamics of even-parity perturbations in the vacuum exterior. The method was subsequently adapted to study neutron star oscillations by Lindblom and Detweiler [82], making it a standard tool for computing quasi-normal modes of compact stars in full general relativity.

To compute the quasi-normal modes, one must identify the complex frequencies ω for which the Zerilli equation admits solutions that are purely outgoing at spatial infinity. This condition serves as the defining boundary condition for the eigenvalue problem. In practice, this requires integrating the Zerilli equation numerically from the stellar surface ($r = R$) to a sufficiently large radius where the asymptotic behavior of the solution becomes manifest. In our implementation, we carry out the integration up to $r \sim 50\,\omega^{-1}$, which has been shown to be adequate for capturing the asymptotic behavior of the Zerilli function and its derivative [82, 150]. Here, ω is the angular frequency of the perturbation, introduced earlier in Eq. (4.4).

At large distances from the star, the Zerilli function $Z(r^*)$ behaves like a linear combination of ingoing and outgoing waves. Specifically, we write

$$Z(r^*) = B_{\rm in} Z_{\rm in}(r^*) + B_{\rm out} Z_{\rm out}(r^*) \,, \tag{5.7}$$

where $Z_{\rm in}(r^*)$ and $Z_{\rm out}(r^*)$ represent the ingoing and outgoing wave components, respectively, and $B_{\rm in}$, $B_{\rm out}$ are their complex amplitudes. In the quasi-normal mode spectrum, the physically admissible solutions correspond to those for which $B_{\rm in} = 0$, i.e., no incoming radiation at infinity.

The asymptotic form of the solutions can be expressed as a power series expansion multiplied by an oscillatory factor:

$$Z_{\text{out}}(r^*) = e^{-i\omega r^*} \sum_{j=0}^{\infty} \beta_j \, r^{-j} \,, \tag{5.8}$$

$$Z_{\text{in}}(r^*) = e^{i\omega r^*} \sum_{j=0}^{\infty} \bar{\beta}_j \, r^{-j} \,, \tag{5.9}$$

where the β_j are complex expansion coefficients and $\bar{\beta}_j$ denote their complex conjugates. The coefficients β_js can be obtained through a recursion relation by substituting equations (5.8) and (5.9) into equation (5.5). To determine the asymptotic behavior of $Z(r^*)$, we consider the expansion up to $O(r^{-2})$. The relevant expressions are as follows:

$$\beta_1 = -i\omega^{-1}(n_l + 1)\beta_0 \,, \tag{5.10}$$

$$\beta_2 = -\frac{1}{2\omega^2}\left[n_l(n_l + 1) - 3iM\omega\left(1 + \frac{2}{n_l}\right)\right]\beta_0 \,, \tag{5.11}$$

where β_0 is an arbitrary constant. For numerical implementation, we have considered $\beta_0 = p_r(0)/\rho(0)$, as suggested by Chandrasekhar and Ferrari [151]. This choice provides a convenient normalization for the coefficients β_j in the recursion relation. From these expressions, we can observe that for a fixed mass of the neutron star and for a specific angular mode ($l = 2$ in the present work), the coefficients B_{in} and B_{out} depend solely on the angular frequency ω. To determine the numerical values of B_{in} and B_{out}, we can compare the numerically integrated values of the Zerilli function and its first derivative with the corresponding asymptotic analytical values described above. By calculating B_{in} for various frequencies, we can treat it as a function of ω. Consequently, we can find the root of this function, which implies $B_{\text{in}}(\omega) = 0$, i.e., purely outgoing wave for that particular ω. The frequency of the oscillation is given by $\mathcal{F} = \text{Re}(\omega)/2\pi$ where $\text{Re}(\omega)$ is the real part of the root. The inverse of the imaginary part of the root $(1/\text{Im}(\omega))$, which we will denote as $\mathfrak{T}$, is the damping time of the oscillation. The values of the mode frequency and corresponding damping time obtained by our code for $\tau = 0$ agrees with earlier results reported by Lu and Suen [152] and Kunjipurayil et al. [89]. In the following sections, we present and analyze the f-mode frequencies and damping times of neutron stars and quark stars, considering the various EsoS and anisotropy ansatz introduced earlier.

5.1 Neutron star

In this section, we aim to quantify the effect of anisotropy on f-mode oscillations of neutron stars. As mentioned earlier, we primarily employ the BSk21 equation of state (EoS) to compute both the background equilibrium structure and the corresponding oscillation modes. In select cases, we also compare the results with those obtained using the softer BSk19 EoS to examine how the stiffness of the EoS influences the behavior of f-mode oscillations in anisotropic stars.

To proceed, we first examine a structural feature of anisotropic stars before delving into their oscillation characteristics. Table 5.1, along with Figs. 3.3 and 3.4, displays various physical parameters across different central densities and anisotropic strengths. From these, it is evident that for a fixed value of the anisotropic parameter τ, increasing the central density ρ_c initially results in simultaneous growth in mass (M) and radius (R) up to a certain point. In this regime, the average density $\rho_{\rm avg} = M[(4/3)\pi R^3]^{-1}$ increases slowly. For example, with $\tau = 0$, this trend persists up to $\rho_c = 8.2817 \times 10^{14}$ g cm^{-3}, where the stellar mass is 1.6 $\mathrm{M}_\odot$.

Beyond this central density, for each value of τ, further increase in ρ_c leads to a decrease in radius and a continued increase in mass, resulting in a rapid rise in average density. To demonstrate this behavior, in Fig. 5.1 we plot τ along the horizontal axis and $\sqrt{\rho_{\rm avg}}$ along the vertical axis for neutron stars with masses 1.0 $\mathrm{M}_\odot$, 1.4 $\mathrm{M}_\odot$, and 2.274 $\mathrm{M}_\odot$. These represent a low-mass neutron star, the canonical mass, and a high-mass configuration, respectively. The highest mass shown, 2.274 $\mathrm{M}_\odot$, corresponds to the maximum stable mass of an isotropic star with the BSk21 EoS.

We find that stars with $M = 1\ \mathrm{M}_\odot$ remain stable for τ in the range $[-2, 2]$, while for 1.4 $\mathrm{M}_\odot$

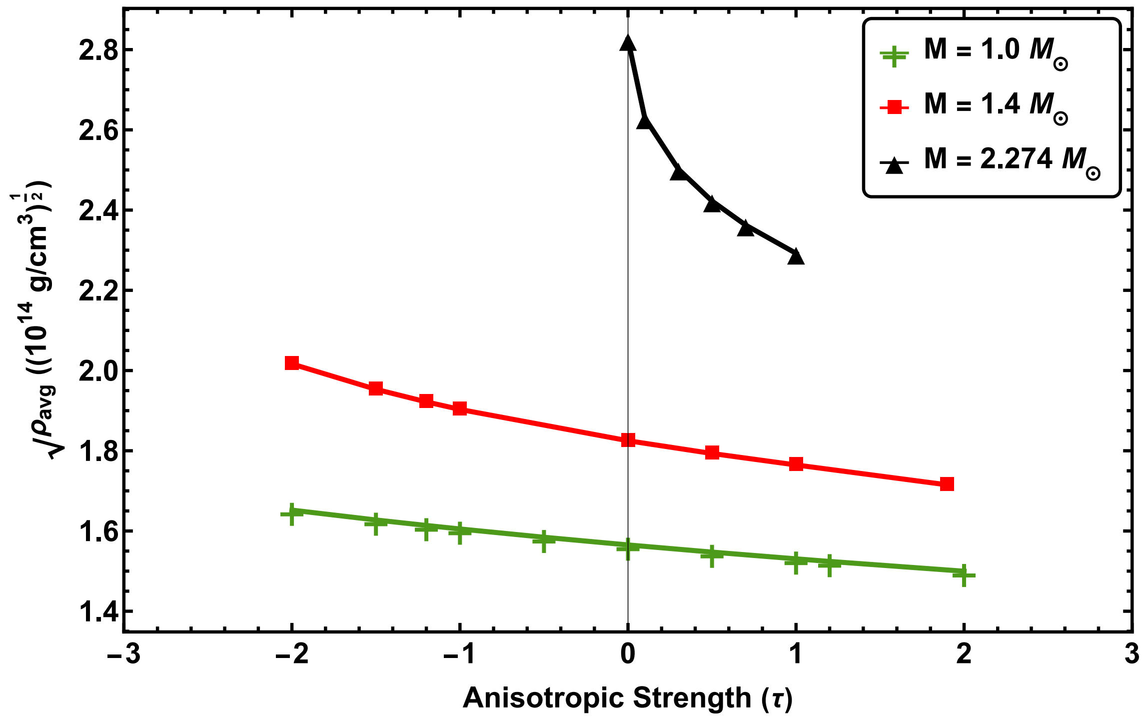

Figure 5.1: Dependence of $\sqrt{\rho_{\text{avg}}}$ on the anisotropic strength τ for neutron stars with masses 1.0 M$_\odot$, 1.4 M$_\odot$, and 2.274 M$_\odot$, based on the BSk21 EoS. The figure illustrates that the influence of anisotropy on the average density becomes increasingly significant as the stellar mass increases.

and 2.274 M$_\odot$, the stable ranges are $[-2, 1.9]$ and $[0, 1]$, respectively. As seen in Fig. 5.1, increasing τ from 0 to 1 leads to a reduction in $\sqrt{\rho_{\text{avg}}}$ by 2.21%, 3.30%, and 18.86% for stars with masses 1.0 M$_\odot$, 1.4 M$_\odot$, and 2.274 M$_\odot$, respectively. This clearly demonstrates that the influence of anisotropy on average density becomes increasingly significant for more massive stars.

5.1.1 Effect of anisotropy on frequency

Next, we investigate the effect of the anisotropy on the properties of the f-mode oscillation of neutron stars. In Fig. 5.2, we plot the frequency of the f-mode along the abscissa and the square root of the average density along the ordinate. From the calculations within the Newtonian theory, as described in Chapter 2, we know that the f-mode frequency is proportional to the square root of the average density of a neutron star. This phenomenon

Table 5.1: Tabulated values of the anisotropic strength (τ), central density (ρ_c), stellar mass (M), radius (R), average density (ρ_{avg}), f-mode frequency ($\mathcal{F}$), and damping time ($\mathfrak{T}$) for neutron stars modeled using the BSk21 EoS.

τ	ρ_c (10^{14} g cm^{-3})	M ($M_\odot$)	R (km)	ρ_{avg} (10^{14} g cm^{-3})	$\mathcal{F}$ (kHz)	$\mathfrak{T}$ (ms)
0.0	5.7661	1.000	12.466	2.4501	1.564	430.098
0.0	6.4801	1.200	12.545	2.8846	1.638	313.507
0.0	7.2955	1.400	12.589	3.3307	1.713	243.028
0.0	8.2817	1.600	12.580	3.8148	1.790	197.672
0.0	9.5711	1.800	12.496	4.3779	1.874	167.387
0.0	11.4921	2.000	12.294	5.1085	1.975	149.810
0.0	22.6476	2.274	11.059	7.9803	2.317	154.280
0.5	5.5206	1.000	12.562	2.3944	1.585	396.740
0.5	6.1758	1.215	12.671	2.8365	1.668	278.210
0.5	6.7874	1.400	12.737	3.2155	1.737	217.250
0.5	8.0285	1.711	12.762	3.9071	1.858	155.940
0.5	9.1689	1.925	12.689	4.4731	1.949	130.850
0.5	12.4966	2.274	12.252	5.8688	2.146	108.880
0.5	20.1137	2.436	11.209	8.2100	2.421	114.960
1.0	5.3021	1.000	12.654	2.3427	1.601	370.810
1.0	5.8204	1.200	12.776	2.7310	1.679	263.490
1.0	6.3670	1.400	12.874	3.1139	1.754	198.690
1.0	7.6519	1.800	12.955	3.9296	1.905	128.780
1.0	10.0875	2.274	12.712	5.2539	2.115	91.680
1.0	14.0191	2.552	12.003	7.0065	2.335	85.390
-0.5	6.0447	1.000	12.365	2.5104	1.537	474.480
-0.5	6.9786	1.217	12.421	3.0149	1.613	345.960
-0.5	7.9262	1.400	12.425	3.4638	1.677	281.400
-0.5	11.4870	1.819	12.170	4.7917	1.847	208.400
-0.5	15.0573	2.000	11.796	5.7837	1.959	201.840
-0.5	16.0571	2.028	11.693	6.0217	1.985	203.134
-1.0	6.3643	1.000	12.259	2.5762	1.502	535.910
-1.0	7.1212	1.150	12.279	2.9480	1.548	438.040
-1.0	8.7378	1.400	12.242	3.6215	1.623	344.180
-1.0	10.6688	1.600	12.109	4.2775	1.687	307.820
-1.0	13.8956	1.788	11.816	5.1462	1.760	302.630

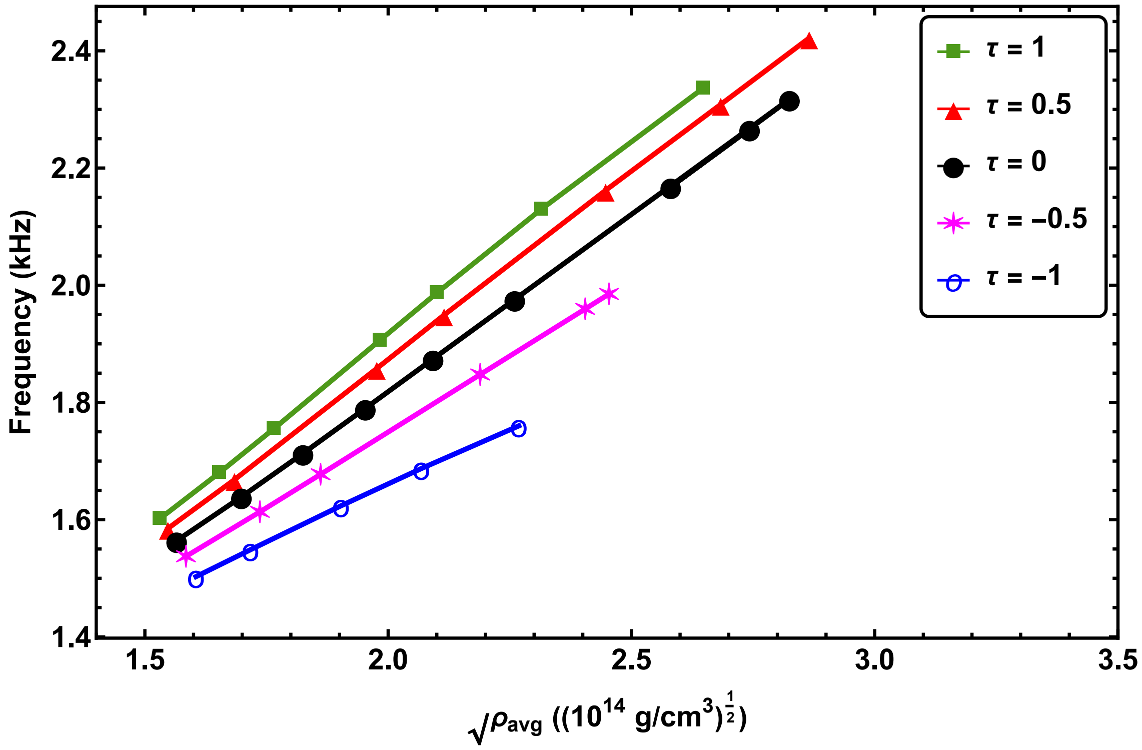

Figure 5.2: Variation of the f-mode frequency with the square root of the average density for neutron stars modeled with the BSk21 EoS, for different values of the anisotropic strength τ.

holds in the case with anisotropy for Newtonian stars [108]. This property also holds in the case of general relativistic results of f-modes of neutron stars [153]. From Fig. 5.2, we see that this frequency versus the square root of the average density ($\mathcal{F} - \sqrt{\rho_{\mathrm{avg}}}$) relation remains unchanged even when full general relativistic calculations are performed for anisotropic neutron stars. The higher values of the anisotropic strength results in higher values of the slope of the $\mathcal{F} - \sqrt{\rho_{\mathrm{avg}}}$ lines. From this figure, it is clear that the f-mode frequency can be written as a functional form as:

$$\mathcal{F}(\rho_{\mathrm{avg}}, \tau) \approx C(\tau)\,\sqrt{\rho_{\mathrm{avg}}} + D(\tau), \tag{5.12}$$

where $C(\tau)$ and $D(\tau)$ are functions of τ that capture the slope of the linear fit and the vertical axis intercept, respectively, in Fig. 5.2. The explicit forms of $C(\tau)$ and $D(\tau)$, along with their dependence on τ, are derived and discussed in detail in Sec. 5.3.

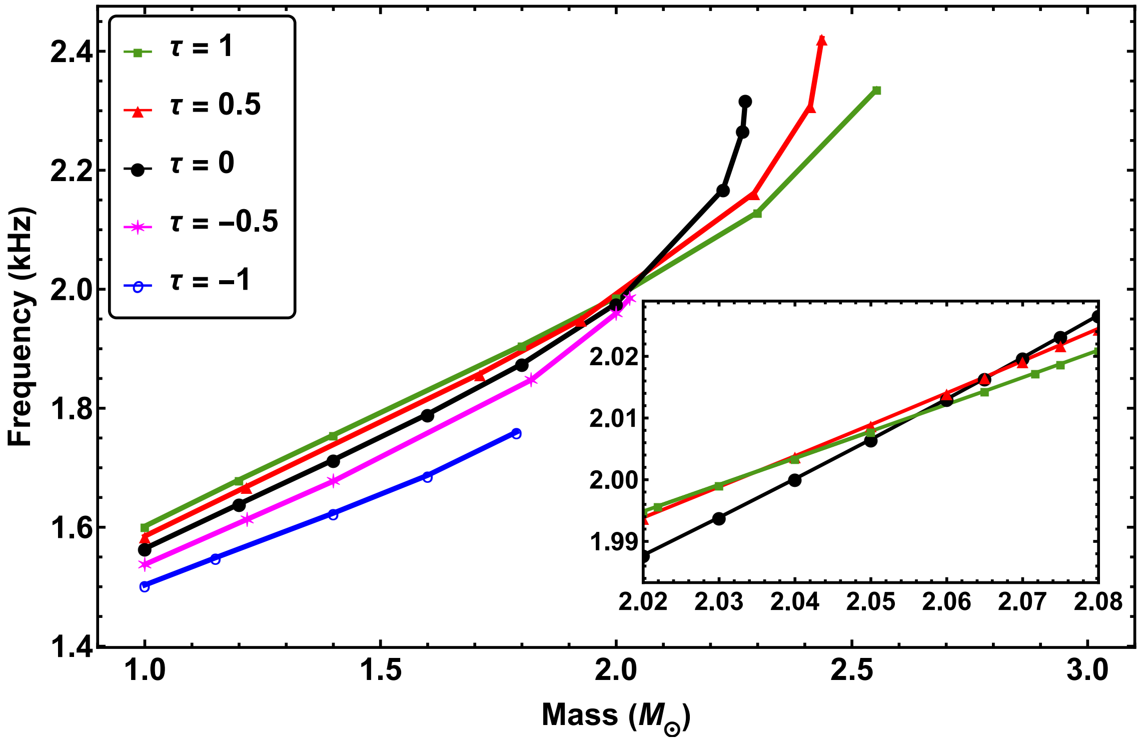

Figure 5.3: Variation of the f-mode frequency with the mass of neutron stars for different values of the anisotropic strength τ, using the BSk21 EoS.

In Fig. 5.3, we plot the frequencies against the mass of the neutron stars for several values of the anisotropic strength. From this figure, we see that, for any given value of the anisotropic strength, neutron stars of higher masses have higher values of the f-mode frequency. For lower masses (less than about 2 $\mathrm{M}_\odot$), the increase of the frequency with the mass is linear, but for massive stars, the frequency increases rapidly with the increase in the value of the mass. However, this non-linear rise of the frequency with the mass is not prominent for negative values of τ. We also see that, for a fixed mass below about 2 $\mathrm{M}_\odot$, a higher value of τ has a larger frequency, but above that mass, a higher value of τ corresponds to a smaller value of the frequency. The crossing points of two constant-τ lines vary slightly depending on the values of τ as shown in the inset, which zooms in on the crossing region. Specifically, the lines for $\tau = 1$ and $\tau = 0.5$ intersect at $M = 2.036\ \mathrm{M}_\odot$, the lines for $\tau = 1$ and $\tau = 0.5$ intersect at $M = 2.055\ \mathrm{M}_\odot$, and the lines for $\tau = 0.5$ and $\tau = 0$ intersect at $M = 2.065\ \mathrm{M}_\odot$.

The rapid increase in the values of the f-mode frequency with the mass for high values

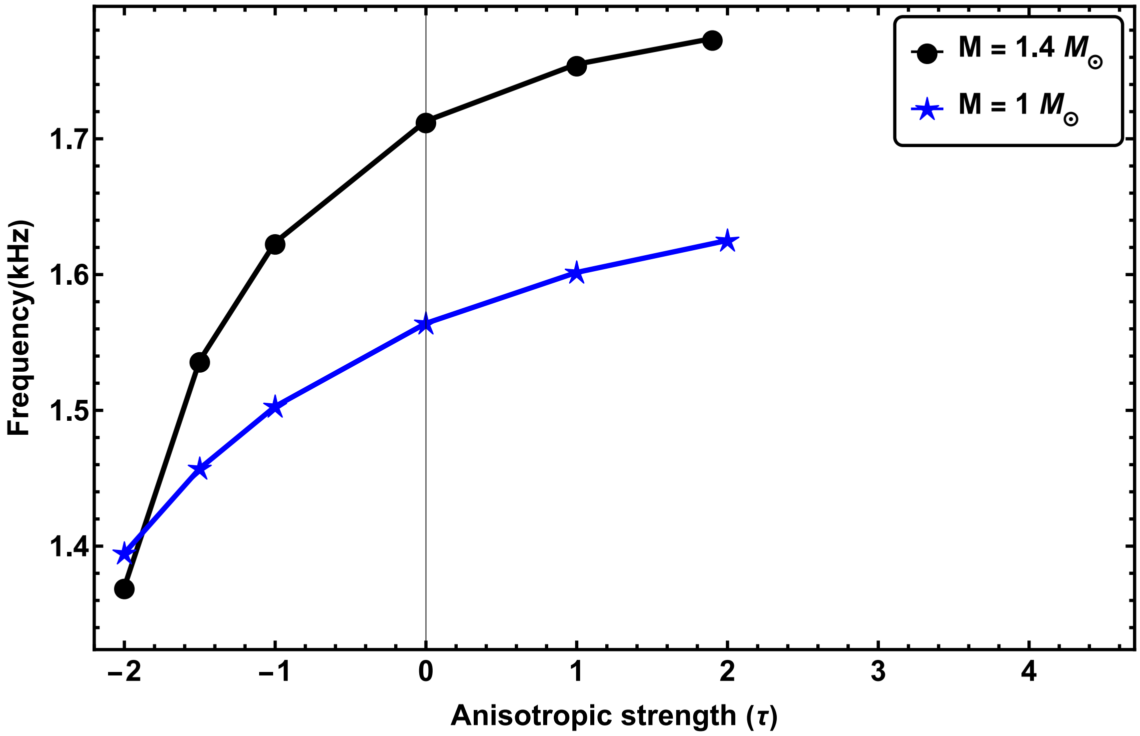

(a) The variation of the f-mode frequency with the anisotropic strength for near solar mass neutron stars.

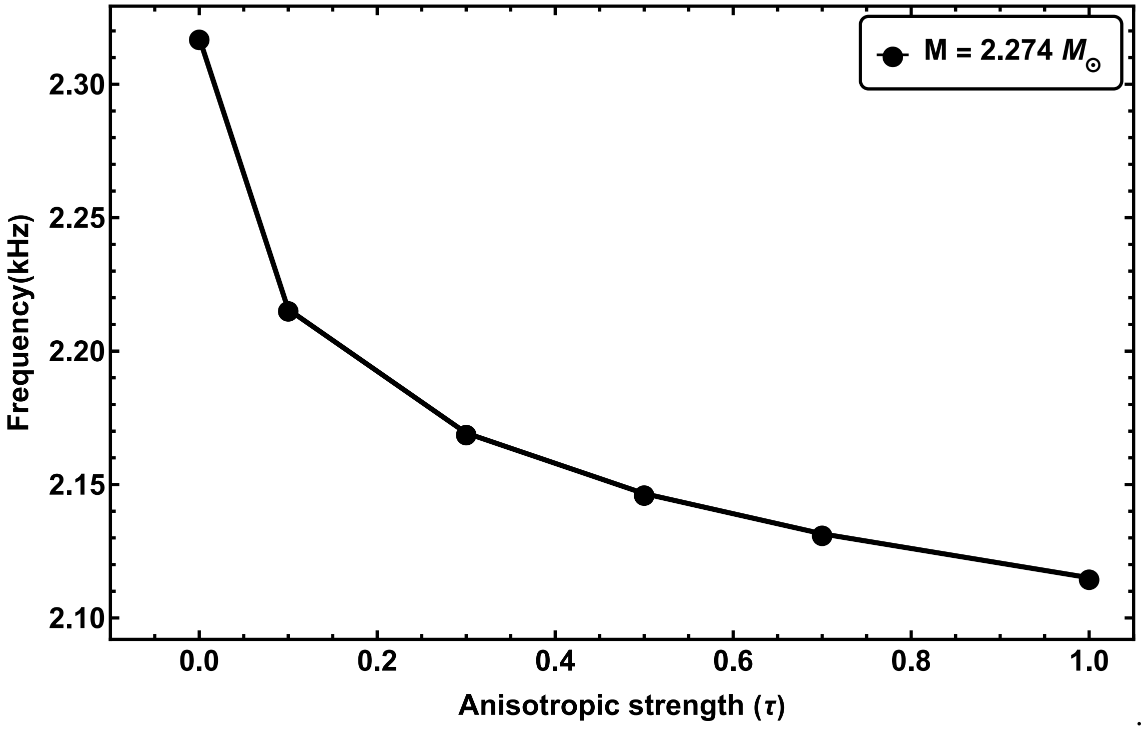

(b) The variation of the f-mode frequency with the anisotropic strength for massive neutron stars.

Figure 5.4: Frequencies of f-modes for different values of the anisotropic strength τ for neutron stars of masses 1.0 $M_\odot$, 1.4 $M_\odot$, and 2.274 $M_\odot$, using the BSk21 EoS.

of masses (as seen in Fig. 5.3) can be understood from Eq. (5.12) and Figs. 5.1 and 5.2. Fig. 5.1 demonstrates the fact that for a fixed value of the anisotropic strength, the value of $\sqrt{\rho_{\rm avg}}$ of a neutron star increases with its mass, and this increase becomes faster for higher values of the mass. For example, when $\tau = 0$, if the mass of the neutron star increases from 1.0 $\mathrm{M}_\odot$ to 1.4 $\mathrm{M}_\odot$, i.e, $\Delta M = 0.4$ $\mathrm{M}_\odot$, the value of $\sqrt{\rho_{\rm avg}}$ rises from 1.56×10^7 $\mathrm{g}^{1/2}\,\mathrm{cm}^{-3/2}$ to 1.82×10^7 $\mathrm{g}^{1/2}\,\mathrm{cm}^{-3/2}$, i.e., $\Delta\sqrt{\rho_{\rm avg}} = 0.26 \times 10^7$ $\mathrm{g}^{1/2}\,\mathrm{cm}^{-3/2}$ giving $\Delta\sqrt{\rho_{\rm avg}}/\Delta M = 0.65 \times 10^7$ $\mathrm{g}^{1/2}\,\mathrm{cm}^{-3/2}\,\mathrm{M}_\odot^{-1}$. On the other hand, keeping τ fixed at 0, if the mass increases from 1.4 $\mathrm{M}_\odot$ to 2.274 $\mathrm{M}_\odot$, i.e, $\Delta M = 0.874$ $\mathrm{M}_\odot$, the value of $\sqrt{\rho_{\rm avg}}$ increases from 1.82×10^7 $\mathrm{g}^{1/2}\,\mathrm{cm}^{-3/2}$ to 2.82×10^7 $\mathrm{g}^{1/2}\,\mathrm{cm}^{-3/2}$, i.e, $\Delta\sqrt{\rho_{\rm avg}} = 1.0 \times 10^7$ $\mathrm{g}^{1/2}\,\mathrm{cm}^{-3/2}$ giving $\Delta\sqrt{\rho_{\rm avg}}/\Delta M = 1.14 \times 10^7$ $\mathrm{g}^{1/2}\,\mathrm{cm}^{-3/2}\,\mathrm{M}_\odot^{-1}$. In summary, the value of $\Delta\sqrt{\rho_{\rm avg}}/\Delta M$ increases as the mass increases, a trend true for any fixed value of τ. Furthermore, Fig. 5.2 shows that for a fixed value of τ, the f-mode frequency is proportional to $\sqrt{\rho_{\rm avg}}$. These two facts jointly result in the rapid non-linear rise in the value of the frequency with the increase in the value of the mass in the high-mass regime (for any constant τ value), as seen in Fig. 5.3.

Fig. 5.2 shows that $C(\tau)$ of Eq. (5.12) is a monotonically increasing function of τ, and Fig. 5.1 illustrates that in the low-mass regime, the variation of $\sqrt{\rho_{\rm avg}}$ with τ is minimal. Consequently, in this regime, the monotonically increasing function $C(\tau)$ dominates the behavior of $\mathcal{F}(\rho_{\rm avg}, \tau)$ as defined in Eq. (5.12). This explains why, in the low-mass region of Fig. 5.1, higher values of τ correspond to higher frequency values for a fixed mass. On the other hand, in the high-mass regime, $\sqrt{\rho_{\rm avg}}$ decreases rapidly with increasing τ as shown in Fig. 5.1. Hence, in this regime, $\sqrt{\rho_{\rm avg}}$ has a greater influence on $\mathcal{F}(\rho_{\rm avg}, \tau)$, leading to lower f-mode frequencies for larger values of τ as observed for higher mass values in Fig. 5.3.

To examine the effect of anisotropy on the f-mode frequency for a given neutron star mass, we present in Fig. 5.4 the variation of the frequency with the anisotropic strength τ for the same three mass values considered earlier in Fig. 5.1. It is to be noted that the mass

2.274 $M_\odot$ used in Fig. 5.4b lies above the threshold beyond which increasing τ results in a reduction of the f-mode frequency at fixed mass, as observed in Fig. 5.3. In contrast, the masses 1.0 $M_\odot$ and 1.4 $M_\odot$ in Fig. 5.4a are below this threshold. From Fig. 5.4a, we find that for neutron stars of 1.0 $M_\odot$ and 1.4 $M_\odot$, the f-mode frequency increases monotonically with increasing τ. In particular, for a 1.4 $M_\odot$ star, the frequency rises by 3.62% when τ is increased from 0 to 1.9, compared to the isotropic case. Conversely, at $\tau = -1.9$, the frequency drops by 17.37% relative to the isotropic star of the same mass. Similarly, for a 1.0 $M_\odot$ star, the frequency increases by 3.78% for $\tau = 1.9$, and decreases by 9.91% for $\tau = -1.9$, compared to the isotropic configuration. On the other hand, for a neutron star of mass 2.274 $M_\odot$, the frequency decreases as τ increases. From Fig. 5.4b, we observe a reduction of about 9.56% in the frequency when τ increases from 0 to 1. This trend, where the f-mode frequency decreases with increasing anisotropic strength for high-mass stars, also appears under the Cowling approximation [110].

Next, we examine the role of the stiffness of the EoS on the f-mode frequency. In Fig. 5.5, we present the variation of the frequency with the anisotropic strength τ for both BSk19 and BSk21 EsoS. To directly compare the effects of stiffness, we consider a fixed neutron star mass of 1.4 $M_\odot$ for both EoSs. For the BSk21 EoS, stable neutron stars of this mass exist within the anisotropic strength range $-2 \lesssim \tau \lesssim 1.9$, whereas for the BSk19 EoS, the corresponding range is $-1 \lesssim \tau \lesssim 1.5$. From the figure, we observe that both curves follow a qualitatively similar trend, indicating a common behavior. However, neutron stars with the softer EoS (BSk19) consistently exhibit higher f-mode frequencies across the entire range of τ. Furthermore, the influence of anisotropy appears to be less significant for the softer EoS, especially for $\tau > 0$. The numerical values of the relevant parameters for the BSk19 EoS are listed in Table 5.2.

We have also performed a comparison between the f-mode frequencies computed using full general relativity and those obtained under the Cowling approximation for both BSk19 and BSk21 equations of state, as presented in Appendix C.

Table 5.2: Tabulated values of the anisotropic strength (τ), central density (ρ_c), stellar mass (M), radius (R), average density (ρ_{avg}), f-mode frequency ($\mathcal{F}$), and damping time ($\mathfrak{T}$) for neutron stars modeled using the BSk19 EoS.

τ	ρ_c (10^{14} g cm^{-3})	M (M$_\odot$)	R (km)	ρ_{avg} (10^{14} g cm^{-3})	$\mathcal{F}$ (kHz)	$\mathfrak{T}$ (ms)
-1.0	10.81	1.000	10.737	3.84	1.837	358.403
-1.0	12.12	1.100	10.632	4.35	1.898	311.810
-1.0	13.70	1.200	10.506	4.91	1.959	279.255
-1.0	18.44	1.400	10.139	6.38	2.091	247.387
-1.0	22.23	1.480	9.874	7.30	2.162	249.933
-0.5	9.96	1.000	10.897	3.67	1.875	312.225
-0.5	10.99	1.100	10.819	4.12	1.942	264.725
-0.5	12.16	1.200	10.726	4.62	2.010	229.696
-0.5	15.27	1.400	10.468	5.79	2.157	184.730
-0.5	20.93	1.600	10.011	7.57	2.344	165.454
0.0	9.25	1.000	11.047	3.52	1.900	281.522
0.0	10.08	1.100	10.989	3.93	1.969	235.179
0.0	13.22	1.400	10.738	5.37	2.185	154.214
0.0	20.91	1.750	10.041	8.21	2.527	117.733
0.0	25.68	1.825	9.663	9.60	2.666	118.646
0.5	8.65	1.000	11.187	3.39	1.916	260.344
0.5	9.33	1.100	11.147	3.77	1.984	215.519
0.5	11.74	1.400	10.971	5.03	2.195	136.536
0.5	13.94	1.600	10.764	6.09	2.351	108.761
0.5	20.42	1.900	10.085	8.79	2.676	88.566
1.0	8.14	1.000	11.319	3.27	1.925	244.381
1.0	8.71	1.100	11.295	3.62	1.993	201.176
1.0	10.61	1.400	11.179	4.76	2.196	124.926
1.0	14.33	1.800	10.794	6.79	2.501	80.238
1.0	21.87	2.090	9.873	10.31	2.886	70.134

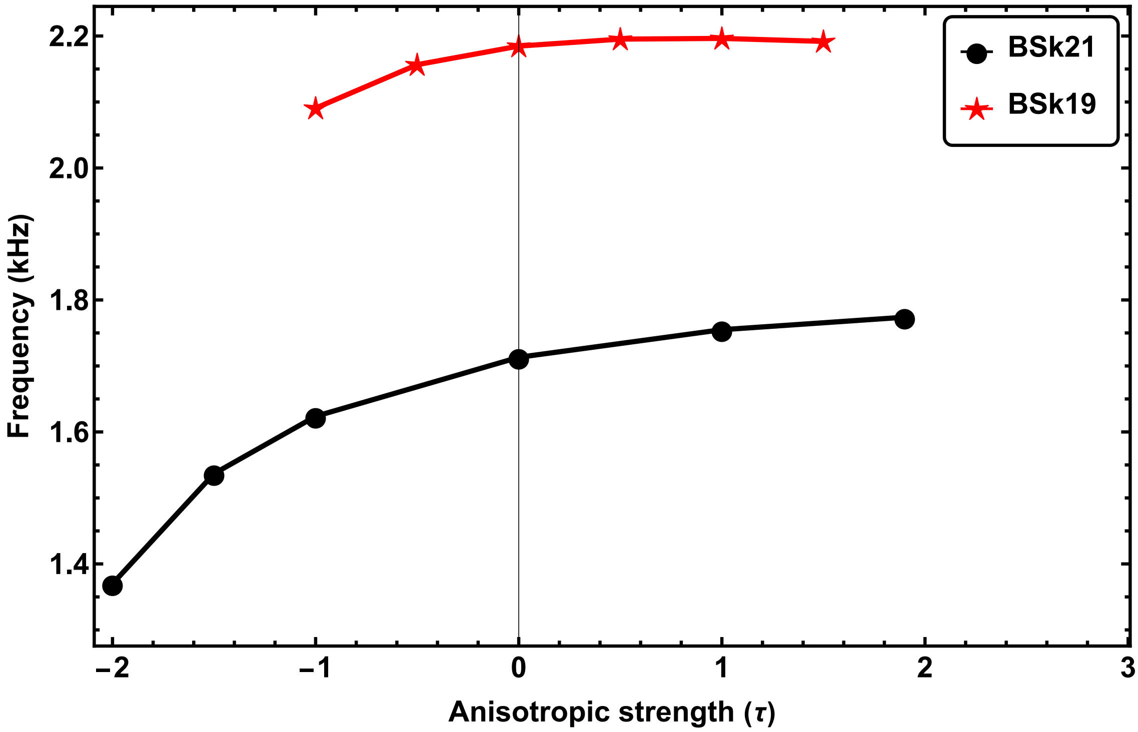

Figure 5.5: Variation of the f-mode frequency with anisotropic strength τ for neutron stars of mass 1.4 $M_{\odot}$, using the BSk19 and BSk21 EsoS.

5.1.2 Effect of anisotropy on damping time

We now turn to the damping time of f-modes, which characterizes the rate at which energy dissipates due to gravitational wave emission from stellar oscillations. As mentioned earlier, the damping time is given by $\mathfrak{T} = 1/\mathrm{Im}(\omega)$. Detweiler [154] showed that $\mathfrak{T}$ scales as R^4/M^3, where M and R are the total mass and radius of the star. Subsequently, Andersson and Kokkotas [84] expressed the normalized inverse damping time, $(\mathfrak{T}M^3/R^4)^{-1}$, as a function of the compactness, M/R. Following this approach, we plot $(\mathfrak{T}M^3/R^4)^{-1}$ versus M/R for BSk21 EoS in Fig. 5.6. From this figure, we observe a linear decrease in the normalized inverse damping time with increasing compactness. The effect of anisotropy is encoded in the slope and intercept of each line. As a result, we approximate the normalized damping time analytically as

$$\frac{R^4}{\mathfrak{T}M^3} \approx J(\tau)\frac{M}{R} + K(\tau), \tag{5.13}$$

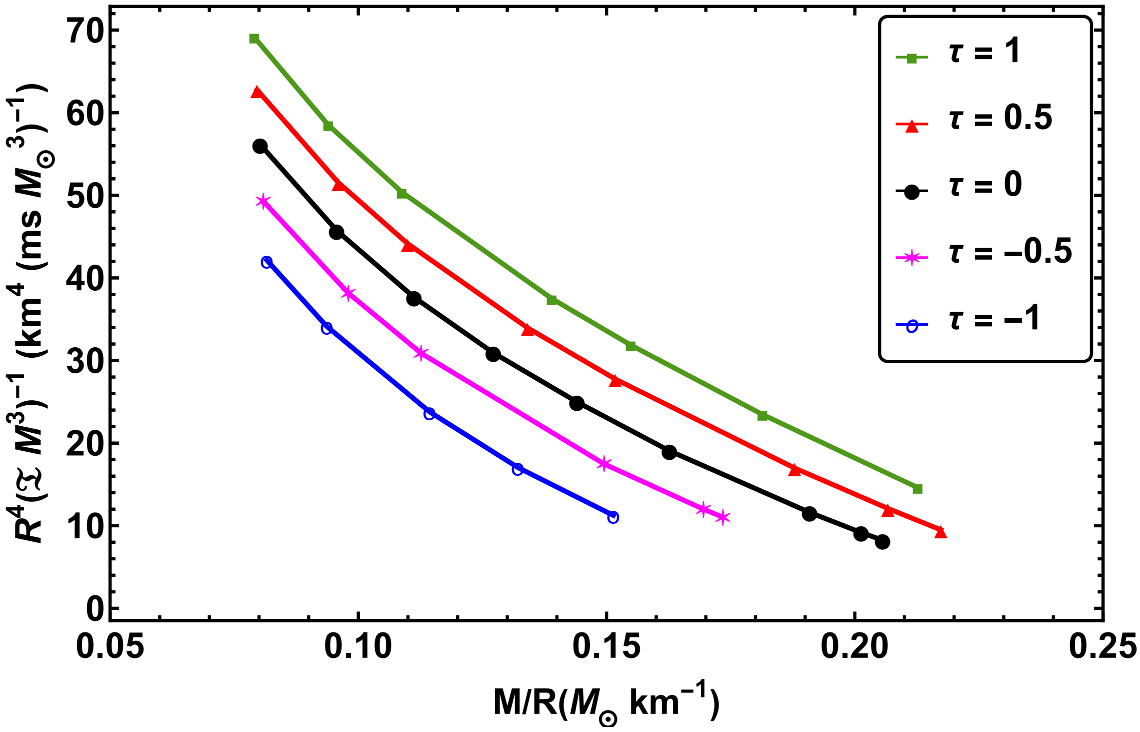

Figure 5.6: Variation of the normalized inverse damping time ($R^4/\mathfrak{I}M^3$) with compactness (M/R) for neutron stars modeled using the BSk21 EoS, for various values of the anisotropic strength τ.

where $J(\tau)$ and $K(\tau)$ represent the slope and vertical-axis intercept, respectively, of the fitted $(\mathfrak{I}M^3/R^4)^{-1}$ versus M/R curves. A more detailed discussion of this analytical expression is presented in Sec. 5.3.

In Fig. 5.7, we show how the damping time varies with the mass of the neutron star for different values of the anisotropic strength. The damping time decreases with increasing stellar mass for all values of τ. However, a slight rise in the damping time near the stable maximum mass is observed for isotropic or mildly anisotropic stars.

In Fig. 5.8, we present the damping time as a function of the anisotropic strength for neutron stars of mass 1.4 $M_\odot$ for both BSk21 and BSk19 EsoS. From the figure, we observe that both curves follow a similar trend. However, for the entire range of τ, neutron stars with the softer EoS (BSk19) exhibit shorter damping times than those with the stiffer EoS (BSk21). For BSk21, when $\tau = 2$, the damping time decreases by 28% relative to the isotropic case. In contrast, decreasing τ from 0 to -2 increases the damping time by

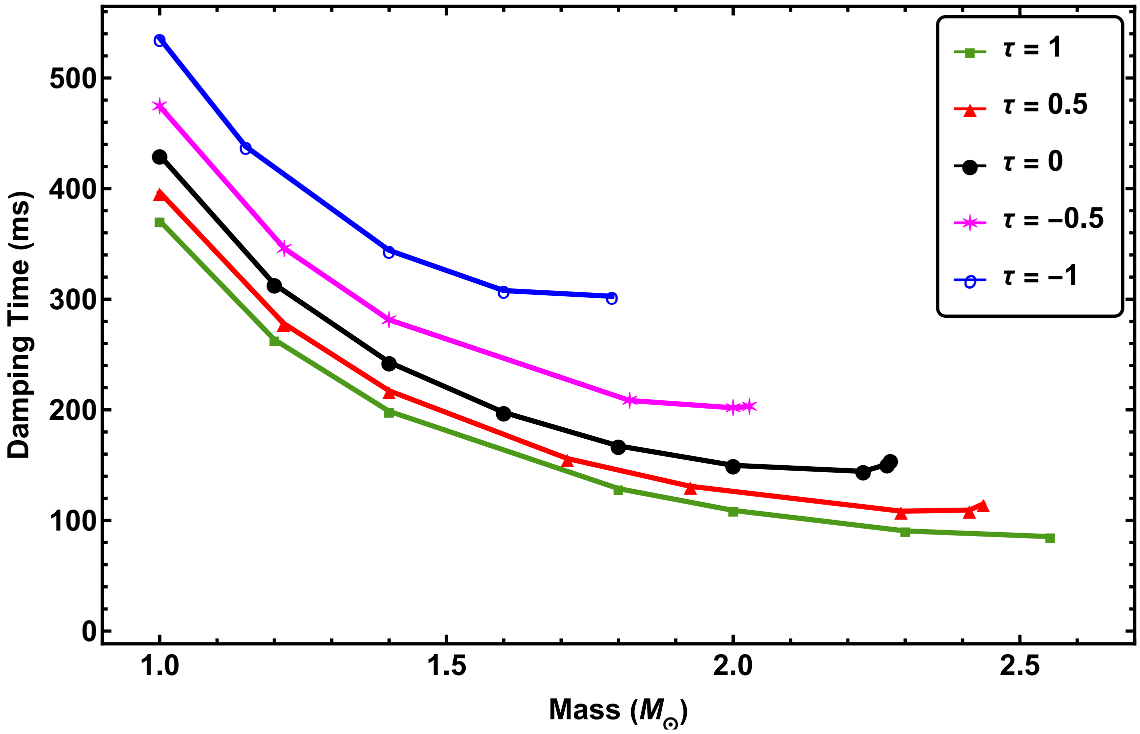

Figure 5.7: Variation of the f-mode damping time with neutron star mass for different values of the anisotropic strength, using the BSk21 EoS.

about 300% compared to the isotropic value. For the BSk19 EoS, increasing τ from 0 to 1.5 results in a 24% reduction in damping time, whereas decreasing τ from 0 to -1 increases it by 60%.

5.2 Quark star

After discussing the effect of anisotropy on the f-mode oscillation in neutron stars, we now present the results of our analysis of f-mode oscillations in anisotropic quark stars within the framework of full general relativity, considering both the MIT bag EoS and EOS-A as introduced in Sec. 3.3.4.

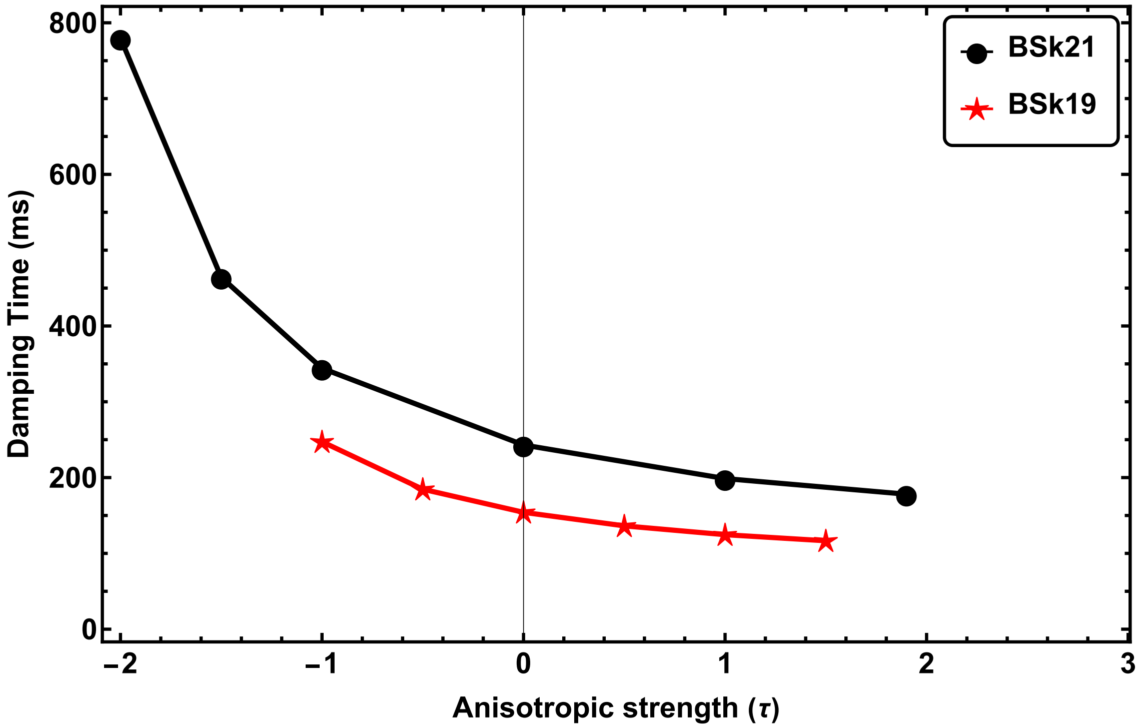

Figure 5.8: Variation of the damping time with anisotropic strength τ for neutron stars of mass 1.4 $M_\odot$, using the BSk19 and BSk21 EsoS.

5.2.1 Effect of anisotropy on f-mode frequency

As in the case of neutron stars discussed in Sec. 5.1, we begin this subsection by examining how the anisotropic parameter τ affects the square root of the average density of quark stars. As mentioned earlier, the average density is given by $\rho_{\rm avg} = M\left[(4/3)\pi R^3\right]^{-1}$. In Fig. 5.9, we plot $\sqrt{\rho_{\rm avg}}$ as a function of τ for quark stars described by the MIT bag EoS (top panel) and EOS-A (bottom panel). These figures clearly demonstrate that $\sqrt{\rho_{\rm avg}}$ decreases as τ increases. Moreover, the decline is steeper for higher mass quark stars, a trend similar to that observed in the neutron star case.

Quantitatively, for the MIT bag EoS, we find that $\sqrt{\rho_{\rm avg}}$ decreases by 0.4%, 0.7%, 1.56%, and 12.19% for quark stars with masses 0.8 $M_\odot$, 1 $M_\odot$, 1.4 $M_\odot$, and 2.03 $M_\odot$, respectively, as τ varies from 0 to 1. Here, 2.03 $M_\odot$ corresponds to the maximum mass of a stable isotropic quark star for the MIT bag EoS. Similarly, for EOS-A, we observe that $\sqrt{\rho_{\rm avg}}$ decreases by 0.68%, 1.1%, 3.37%, and 9.30% for quark stars with masses 0.8 $M_\odot$, 1 $M_\odot$,

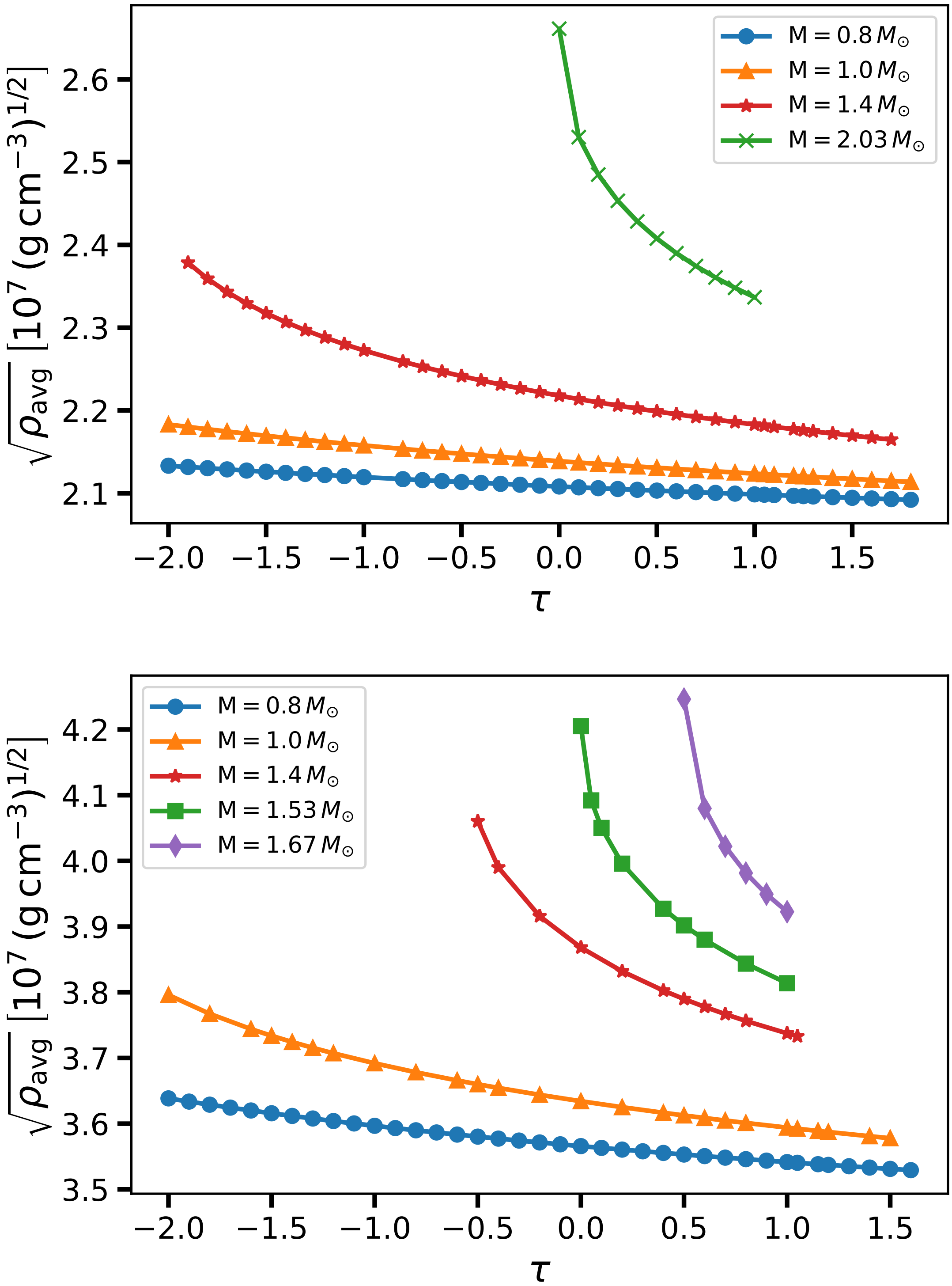

Figure 5.9: Variation of $\sqrt{\rho_{\mathrm{avg}}}$ with anisotropic strength τ for quark stars modeled using the MIT bag EoS (top panel) and EOS-A (bottom panel).

Table 5.3: Numerical values of various parameters for the MIT bag EoS with a bag constant of $B = 56$ MeV fm^{-3}. The columns list the anisotropic strength (τ), central density (ρ_c), stellar mass (M), radius (R), average density (ρ_{avg}), f-mode frequency ($\mathcal{F}$), and damping time ($\mathfrak{T}$).

τ	ρ_c (10^{15} g cm^{-3})	M (M$_\odot$)	R (km)	ρ_{avg} (10^{15} g cm^{-3})	$\mathcal{F}$ (kHz)	$\mathfrak{T}$ (ms)
-1.0	0.549	0.800	9.455	0.449	1.547	652.074
-1.0	0.609	1.000	10.065	0.466	1.562	497.486
-1.0	0.648	1.100	10.318	0.475	1.572	446.413
-1.0	0.696	1.200	10.539	0.487	1.584	406.271
-1.0	0.838	1.400	10.877	0.516	1.617	348.390
-1.0	1.156	1.600	11.009	0.569	1.682	309.611
-1.0	2.121	1.705	10.643	0.671	1.830	287.123
-0.5	0.535	0.800	9.473	0.447	1.590	578.295
-0.5	0.584	1.000	10.096	0.461	1.613	428.998
-0.5	0.650	1.200	10.594	0.479	1.642	339.828
-0.5	0.692	1.300	10.800	0.490	1.659	307.919
-0.5	0.745	1.400	10.977	0.502	1.679	281.665
-0.5	0.904	1.600	11.228	0.537	1.734	240.985
-0.5	1.307	1.800	11.224	0.604	1.846	208.929
-0.5	2.041	1.862	10.861	0.690	1.992	193.163
0.0	0.524	0.800	9.489	0.444	1.628	521.297
0.0	0.543	0.900	9.823	0.451	1.642	440.111
0.0	0.564	1.000	10.124	0.457	1.657	379.063
0.0	0.615	1.200	10.641	0.473	1.689	294.337
0.0	0.779	1.600	11.367	0.517	1.777	200.625
0.0	0.944	1.800	11.547	0.555	1.848	172.070
0.0	1.093	1.900	11.554	0.585	1.903	159.869
0.0	1.417	2.000	11.404	0.640	2.003	147.122
0.5	0.513	0.800	9.504	0.442	1.661	476.069
0.5	0.547	1.000	10.149	0.454	1.694	341.141
0.5	0.566	1.100	10.428	0.460	1.711	296.538
0.5	0.587	1.200	10.681	0.467	1.729	261.280
0.5	0.637	1.400	11.119	0.483	1.768	209.541
0.5	0.702	1.600	11.469	0.503	1.813	173.781
0.5	0.954	2.000	11.850	0.570	1.948	127.738
0.5	1.756	2.215	11.328	0.723	2.228	105.031
1.0	0.504	0.800	9.518	0.440	1.691	439.494
1.0	0.518	0.900	9.861	0.446	1.709	366.225
1.0	0.532	1.000	10.172	0.451	1.727	311.536
1.0	0.564	1.200	10.716	0.463	1.763	236.335
1.0	0.582	1.300	10.954	0.469	1.781	209.705
1.0	0.602	1.400	11.172	0.477	1.801	187.935
1.0	0.624	1.500	11.371	0.484	1.821	169.886
1.0	0.935	2.200	12.148	0.583	2.031	98.730
1.0	1.567	2.405	11.585	0.734	2.301	83.160

1.4 $M_\odot$, and 1.54 $M_\odot$, respectively, over the same range of τ. The value 1.54 $M_\odot$ denotes the maximum mass of a stable isotropic ($\tau = 0$) quark star modeled using EOS-A. It is important to note that this decreasing trend of $\sqrt{\rho_{\text{avg}}}$ with increasing τ also appears in the case of neutron stars, as discussed in Sec. 5.1.

Next, we investigate the effect of anisotropy on the f-mode frequency. In the previous section, for neutron stars, we found that the f-mode frequency exhibits a linear dependence on $\sqrt{\rho_{\text{avg}}}$, with the slope and intercept determined by the specific value of τ. It is therefore natural to examine whether a similar relation holds for quark stars.

In Fig. 5.10, we plot $\sqrt{\rho_{\text{avg}}}$ along the abscissa and the corresponding f-mode frequency along the ordinate for various values of τ for the MIT bag EoS (top panel) and EOS-A (bottom panel). For both EsoS, the isotropic case ($\tau = 0$) shows a clear linear relation between the frequency and $\sqrt{\rho_{\text{avg}}}$. When anisotropy is introduced, the relation remains approximately linear; however, both the slope and the intercept are significantly influenced by the value of τ. These effects are more prominent for configurations with $p_t < p_r$ ($\tau < 0$) in both EsoS. The explicit form of this dependence is discussed in detail in Sec. 5.3.

In Fig. 5.11, we plot the f-mode frequency against the total mass of quark stars for different values of the anisotropic strength. The top panel corresponds to the MIT bag EoS, and the bottom panel presents the results for EOS-A. For $\tau \geq 0$, the MIT bag EoS shows a linear rise in frequency with increasing mass up to about 2 $M_\odot$, beyond which the frequency grows nonlinearly. A similar trend is observed with EOS-A for $\tau \geq 0$, though the linear region is limited to lower masses around $1.4 \sim 1.5$ $M_\odot$. For $\tau < 0$, the qualitative behavior remains comparable, but the linear rise is restricted to lower mass ranges: $1.5 \sim 1.6$ $M_\odot$ for the MIT bag EoS and $1.2 \sim 1.3$ $M_\odot$ for EOS-A. Beyond these ranges, the frequency increases nonlinearly for $\tau = -0.5, -1.0$, and -1.5. Notably, for $\tau = -2$, the behavior deviates, frequency decreases monotonically with mass for both EsoS.

As mass is a fundamental and measurable parameter of stars, we next examine the influ-

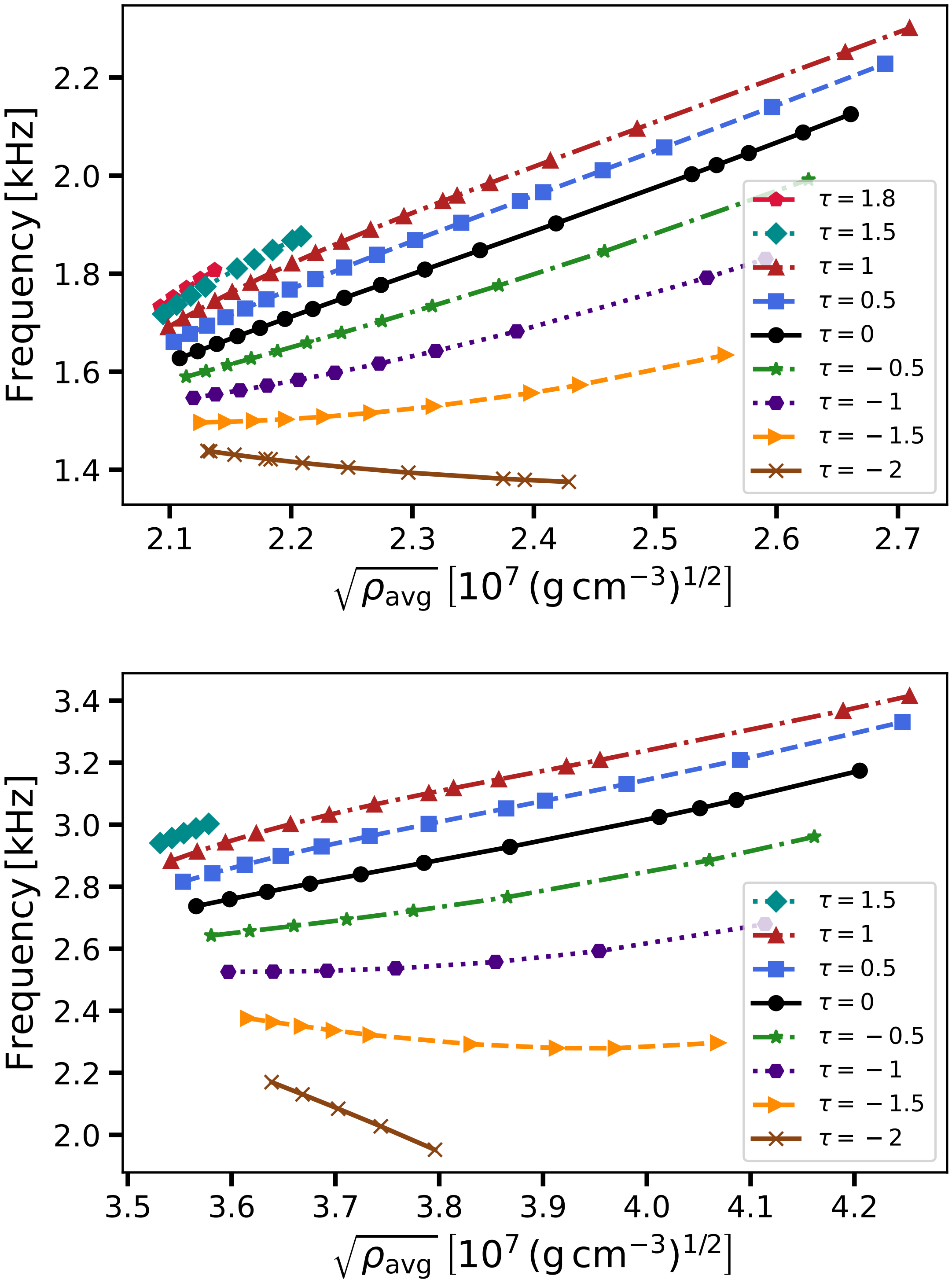

Figure 5.10: Variation of the f-mode frequency with the square root of the average density for quark stars with different anisotropic strengths. The top panel shows results for the MIT bag EoS, while the bottom panel corresponds to EOS-A.

Table 5.4: Numerical values of various parameters for the EOS-A EoS. The columns list, from left to right, the anisotropic strength (τ), central density (ρ_c), stellar mass (M), radius (R), average density (ρ_{avg}), f-mode frequency ($\mathcal{F}$), and damping time ($\mathfrak{T}$).

τ	ρ_c (10^{15} g cm^{-3})	M (M$_\odot$)	R (km)	ρ_{avg} (10^{15} g cm^{-3})	$\mathcal{F}$ (kHz)	$\mathfrak{T}$ (ms)
-1.0	1.626	0.800	6.646	1.294	2.526	242.800
-1.0	1.743	0.900	6.857	1.325	2.526	223.400
-1.0	1.902	1.000	7.036	1.363	2.529	211.800
-1.0	2.141	1.100	7.177	1.412	2.537	206.600
-1.0	2.586	1.200	7.265	1.486	2.558	208.300
-1.0	4.809	1.290	7.127	1.692	2.679	222.300
-0.5	1.563	0.800	6.666	1.282	2.643	197.400
-0.5	1.650	0.900	6.886	1.308	2.657	175.900
-0.5	1.759	1.000	7.076	1.340	2.674	160.700
-0.5	2.114	1.200	7.366	1.425	2.722	143.300
-0.5	2.477	1.300	7.447	1.494	2.766	139.900
-0.5	3.652	1.400	7.387	1.649	2.885	140.700
0.0	1.512	0.800	6.684	1.272	2.737	167.200
0.0	1.578	0.900	6.910	1.295	2.760	146.100
0.0	1.657	1.000	7.110	1.321	2.784	130.600
0.0	1.754	1.100	7.284	1.351	2.810	119.100
0.0	1.878	1.200	7.433	1.387	2.840	110.700
0.0	2.053	1.300	7.552	1.433	2.877	104.700
0.0	2.330	1.400	7.630	1.496	2.928	100.800
0.0	2.957	1.500	7.619	1.610	3.025	99.230
0.0	4.223	1.540	7.447	1.768	3.174	99.530
0.5	1.469	0.800	6.700	1.262	2.816	145.900
0.5	1.521	0.900	6.932	1.283	2.843	125.700
0.5	1.580	1.000	7.138	1.305	2.871	110.800
0.5	1.649	1.100	7.322	1.330	2.900	99.570
0.5	1.731	1.200	7.484	1.359	2.930	91.060
0.5	1.973	1.400	7.735	1.436	3.002	79.880
0.5	2.177	1.500	7.812	1.494	3.052	76.640
0.5	2.554	1.600	7.826	1.584	3.131	74.980
0.5	3.815	1.670	7.607	1.803	3.331	75.490
1.0	1.433	0.800	6.715	1.254	2.883	130.000
1.0	1.475	0.900	6.951	1.272	2.913	110.900
1.0	1.520	1.000	7.163	1.292	2.943	96.860
1.0	1.571	1.100	7.354	1.313	2.972	86.200
1.0	1.629	1.200	7.524	1.337	3.002	78.020
1.0	1.780	1.400	7.807	1.397	3.065	66.860
1.0	2.274	1.700	8.020	1.564	3.209	59.430
1.0	3.019	1.800	7.867	1.755	3.367	60.170

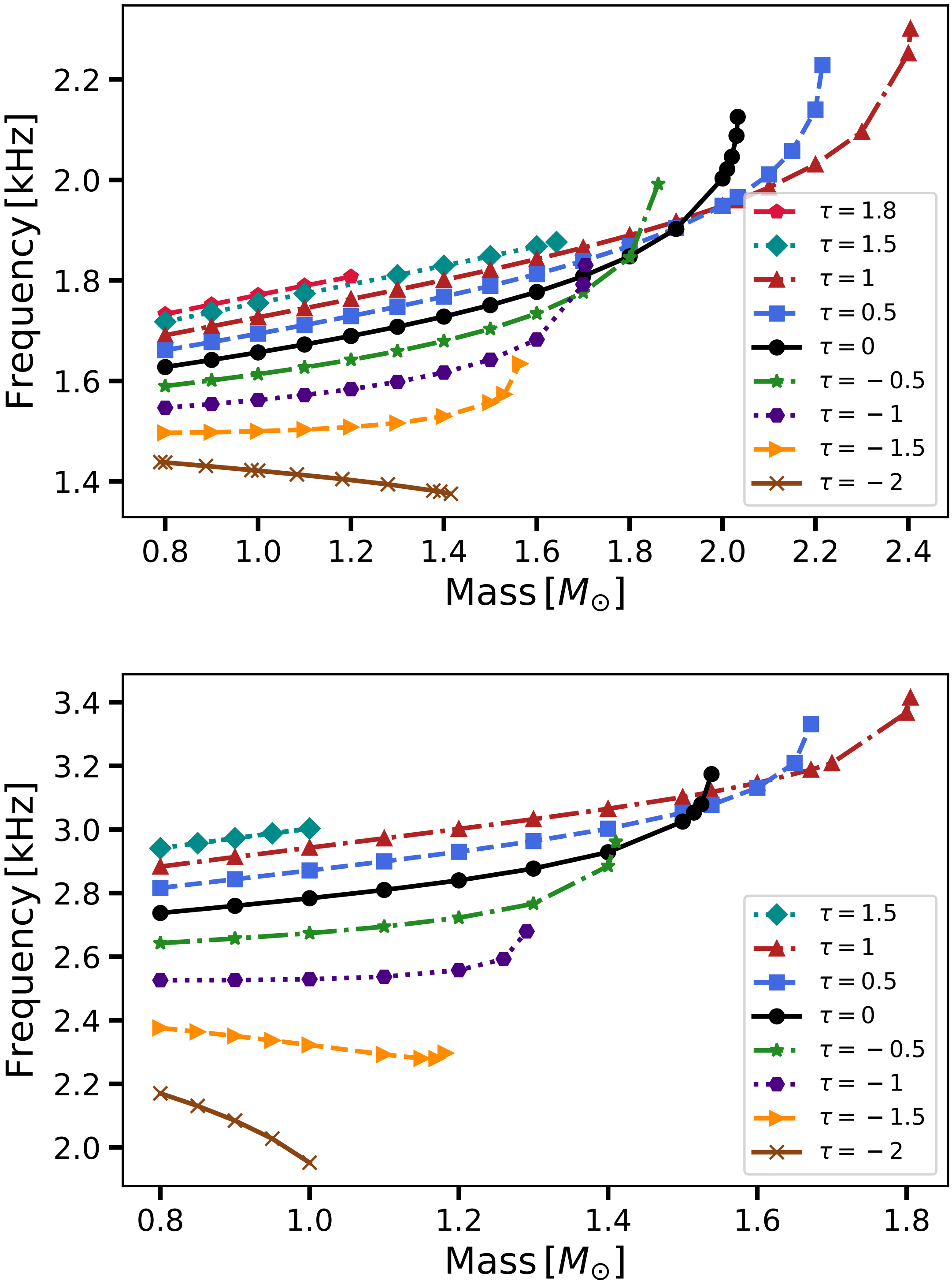

Figure 5.11: Variation of the f-mode frequency with the stellar mass for quark stars at different values of the anisotropic strength. The top panel presents results for the MIT bag EoS, while the bottom panel corresponds to EOS-A.

ence of anisotropy on the f-mode frequency for quark stars of fixed masses. For this purpose, we plot the f-mode frequency as a function of τ for several mass values in Fig. 5.12, where the top panel corresponds to the MIT bag EoS and the bottom panel to EOS-A. For quark stars described by the MIT bag EoS, an increase in the anisotropic strength τ from 0 to 1.7 results in a frequency rise of 6.16% and 6.42% for stars with masses 0.8 $M_\odot$ and 1.4 $M_\odot$, respectively. Conversely, as τ decreases from 0 to -1.7, the f-mode frequency decreases by 9.4%, 11.2%, and 14.2% for quark stars with masses of 0.8 $M_\odot$, 1 $M_\odot$, and 1.4 $M_\odot$, respectively. For a more massive star with $M = 2.03\ M_\odot$, a decrease of 7.81% in the frequency is observed as τ increases from 0 to 1. This behavior arises due to the rapid decline of $\sqrt{\rho_{\rm avg}}$ with increasing τ, as seen earlier in Fig. 5.9. According to Eq. (5.12), the frequency is directly proportional to $\sqrt{\rho_{\rm avg}}$, and hence, this decline leads to a corresponding drop in the frequency. A similar trend has also been observed in the case of neutron stars, as discussed in the previous section.

A comparable pattern is noted for quark stars modeled with EOS-A. For masses of 0.8 $M_\odot$, 1 $M_\odot$, and 1.4 $M_\odot$, the f-mode frequency increases by 5.3%, 5.7%, and 4.66%, respectively, when τ increases from 0 to 1. On the other hand, a decrease of 7.72% and 9.14% is observed as τ varies from 0 to -1 for stars of mass 0.8 $M_\odot$ and 1 $M_\odot$, respectively. These behaviors are clearly visible in the bottom panel of Fig. 5.12.

From the same panel (bottom panel of Fig. 5.12), we also observe that for a 1.53 $M_\odot$ quark star, the frequency initially drops by about 3.3% as τ changes from 0 to 0.2, and then increases by 1.57% as τ increases further from 0.2 to 1. This behavior results from a combined effect of the trends in Fig. 5.9 and Fig. 5.10. Specifically, Fig. 5.9 shows that $\sqrt{\rho_{\rm avg}}$ decreases with increasing τ, and this drop is steeper for lower values of τ. The $\sqrt{\rho_{\rm avg}}$ vs. τ curves vary in shape depending on mass. Additionally, Fig. 5.10 illustrates that for a fixed τ, $\mathcal{F}$ increases with $\sqrt{\rho_{\rm avg}}$ (except for $\tau = -2$), and for a fixed $\sqrt{\rho_{\rm avg}}$, $\mathcal{F}$ increases with τ. The $\mathcal{F}$ vs. $\sqrt{\rho_{\rm avg}}$ curves are not parallel, leading to a nontrivial interplay between the frequency, density, and anisotropy, which manifests differently across stellar masses in Fig. 5.12. This motivates the introduction of an empirical relation among $\mathcal{F}$, $\sqrt{\rho_{\rm avg}}$, and τ as given in Eq. (5.12), and the same involving $\mathcal{F}$, M, R, and τ as presented in Eq. (5.14). We will discuss Eq. (5.14) in details afterward.

For more massive stars, such as a 1.67 $\mathrm{M}_\odot$ quark star, the f-mode frequency decreases by 4.29% as τ increases from 0.5 to 1. This reduction is attributed to the rapid decline in $\sqrt{\rho_{\rm avg}}$ with increasing τ, as illustrated in the bottom panel of Fig. 5.9.

We have also performed a comparison between the f-mode frequencies computed using full general relativity and those obtained under the Cowling approximation for both MIT-bag and EOS-A equations of state, as presented in Appendix C.

5.2.2 Effect of anisotropy on damping time

We now turn to the analysis of the damping time associated with f-mode oscillations in quark stars. As discussed previously for neutron stars (see Sec. 5.1.2), the normalized inverse damping time, $(\mathfrak{T}M^3/R^4)^{-1}$, shows a linear dependence on the compactness, M/R. Motivated by this observation, we apply the same formalism to quark stars described by the MIT bag model and EOS-A to investigate how anisotropy influences this relation in quark matter.

Figure 5.13 presents the variation of $(\mathfrak{T}M^3/R^4)^{-1}$ with M/R for several values of the anisotropic strength τ. Similar to the neutron star case, the normalized inverse damping time decreases approximately linearly as the compactness increases. However, due to differences in the internal structure and the equations of state, the slope and intercept vary. The anisotropy modifies this linear trend, with its effect captured in the fitting coefficients, as also discussed in Sec. 5.1.2.

To explore the anisotropy effect further, we examine how the damping time varies with the stellar mass. In Fig. 5.14, the damping time is plotted as a function of mass for different values of τ for both EsoS. For $\tau \geq 0$, the damping time decreases monotonically with

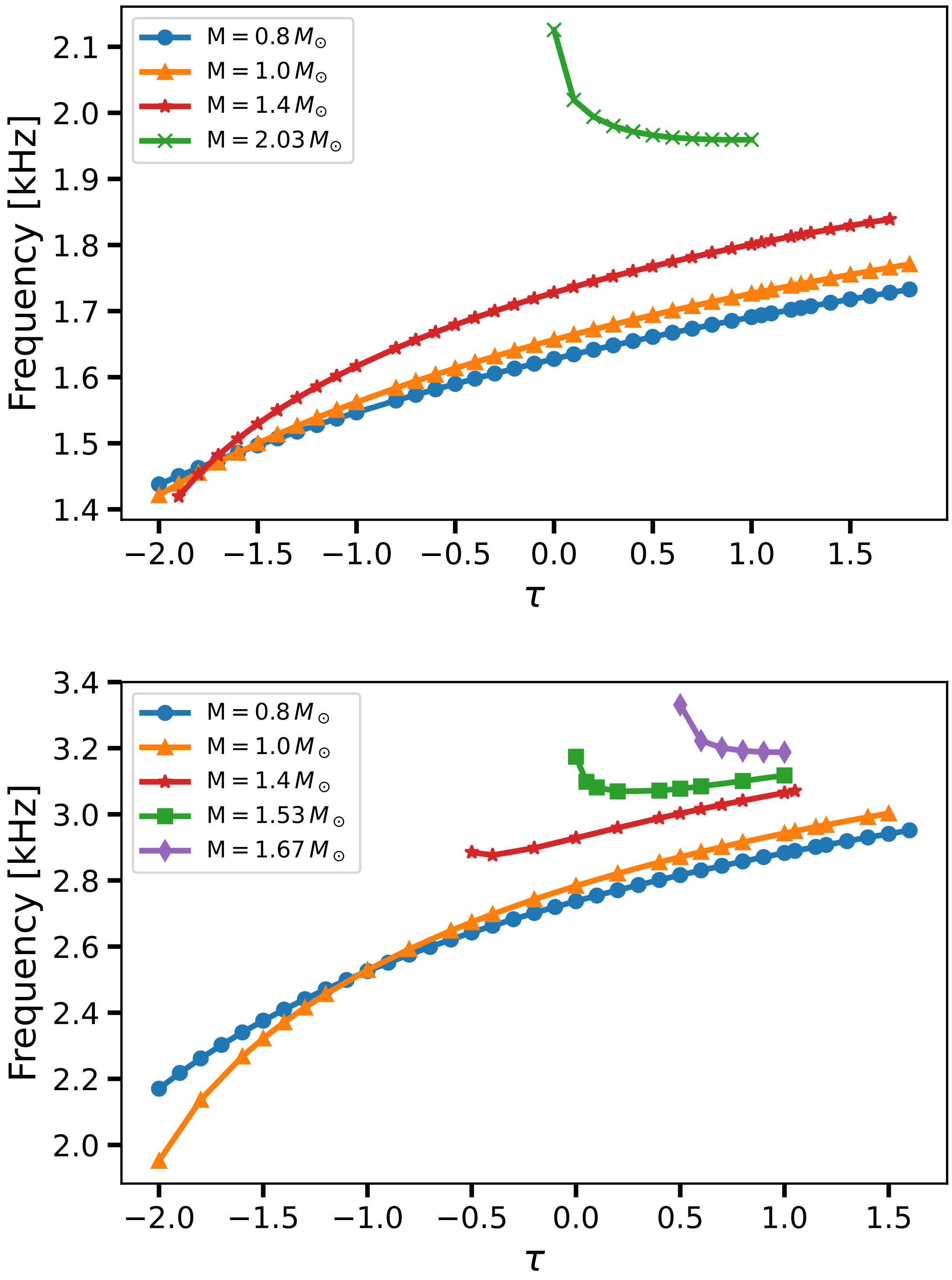

Figure 5.12: Variation of the f-mode frequency with anisotropic strength for quark stars of fixed masses. The top panel shows results for the MIT bag EoS, and the bottom panel corresponds to EOS-A.

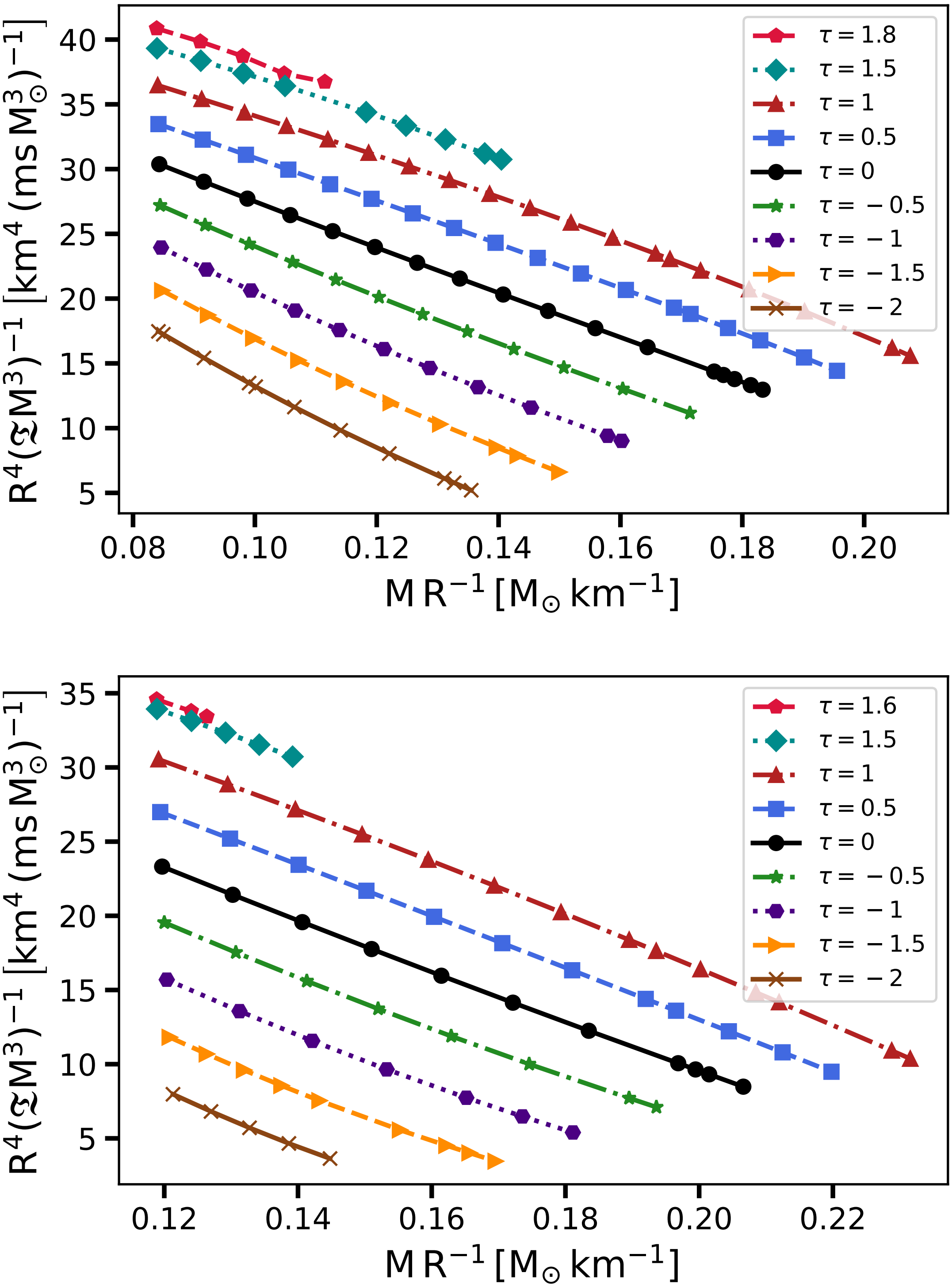

Figure 5.13: Variation of the inverse normalized damping time ($R^4/\mathfrak{I}M^3$) with compactness (M/R) for quark stars at different values of the anisotropic strength τ. The top panel corresponds to the MIT bag EoS, while the bottom panel represents EOS-A.

increasing mass for both EsoS. For the MIT bag EoS, a sharp increase in damping time is observed for high-mass stars when $\tau \leq -1.5$, as shown in the top panel of Fig. 5.14. The bottom panel, corresponding to EOS-A, exhibits a similar trend for $\tau \leq -1$. Interestingly, for $\tau = -2$, the damping time increases monotonically with mass for EOS-A, whereas no such monotonic trend is evident for the MIT bag EoS.

To investigate the influence of anisotropy on the damping time of quark stars with fixed masses, we plot the damping time as a function of the anisotropic strength τ for stars of masses 0.8 $M_\odot$, 1 $M_\odot$, and 1.4 $M_\odot$ for both of the EsoS in Fig. 5.15. For the MIT bag EoS (top panel), as τ increases from 0 to 1.7, the damping time decreases by 23.29%, 25.65%, and 31.90% for the stars with masses 0.8 $M_\odot$, 1 $M_\odot$, and 1.4 $M_\odot$, respectively. Conversely, as τ decreases from 0 to -1.7, the damping time increases significantly by 53.56%, 71.55%, and 131.48% for the same masses.

For EOS-A (bottom panel of Fig. 5.15), we observe a reduction in damping time by 29.48% and 33.59% for 0.8 $M_\odot$ and 1 $M_\odot$ quark stars, respectively, as τ increases from 0 to 1.5. On the other hand, as τ decreases from 0 to -1.5, the damping time increases significantly by 90.15% and 141.40%, respectively. For a 1.4 $M_\odot$ quark star, the damping time decreases by 34.69% as τ increases from 0 to 1.05. For $\tau < 0$, stable and physical quark stars with mass 1.4 $M_\odot$ are not found (see bottom panels of Figs. 3.8 and 3.9).

These results clearly demonstrate that for both EsoS, the f-mode frequency and damping time are significantly affected by the mass, radius, and anisotropic strength of quark stars. Although the overall trends in $\mathcal{F}$ and $\mathfrak{T}$ are similar across both EsoS, the specific parameter ranges differ. For the MIT bag EoS, the f-mode frequency lies between 1.3 kHz and 2.3 kHz, while for EOS-A it spans a higher range of 1.8 kHz to 3.4 kHz. Similarly, the damping time ranges from 83 ms to 900 ms for the MIT bag EoS, and from 60 ms to 761 ms for EOS-A. These results highlight the role of the equation of state, along with stellar structure and anisotropy, in determining the f-mode oscillation properties of quark stars.

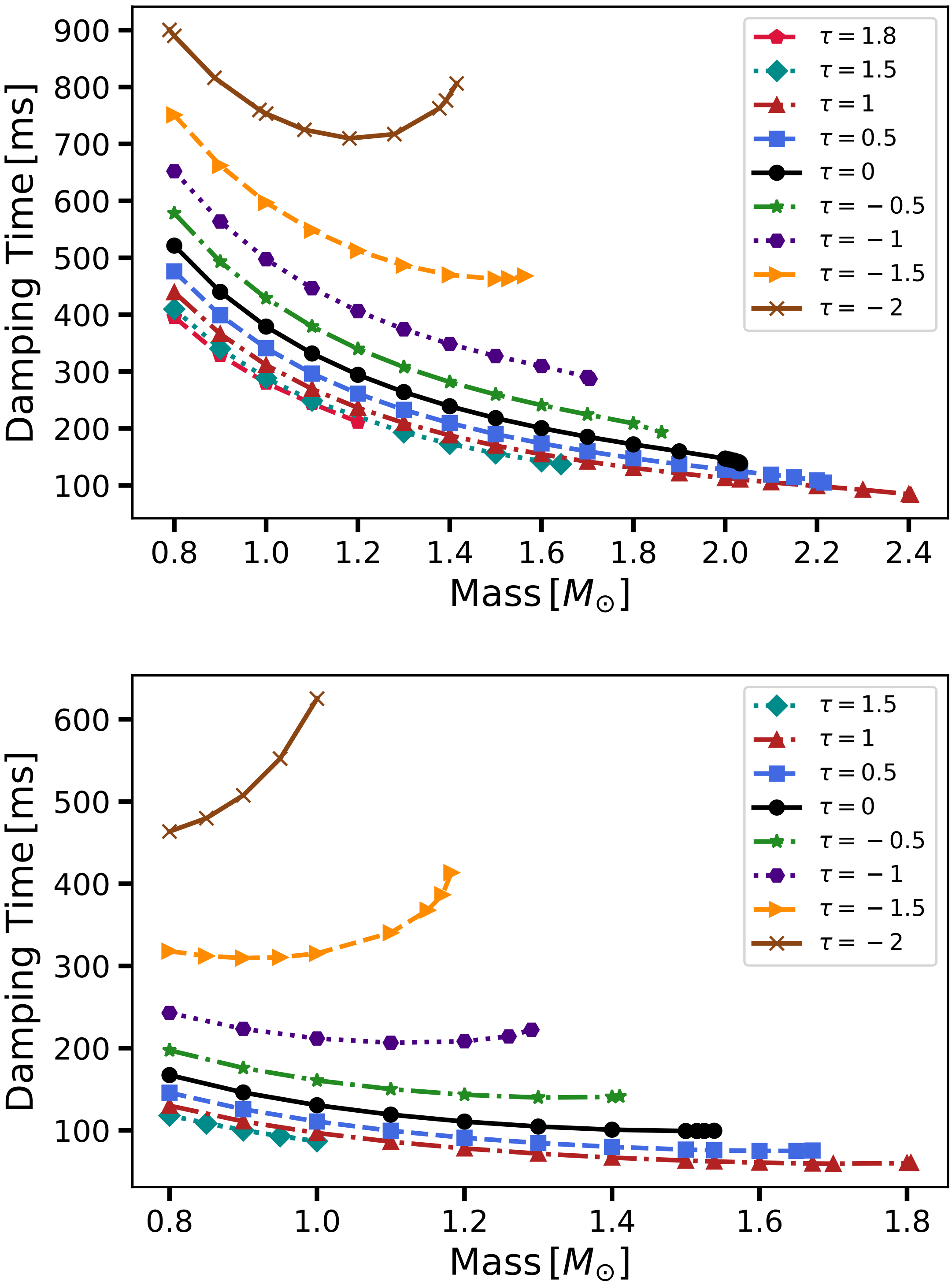

Figure 5.14: Variation of the damping time of f-mode oscillations with the stellar mass for quark stars at different values of the anisotropic strength τ. The top panel presents results for the MIT bag EoS, while the bottom panel corresponds to EOS-A.

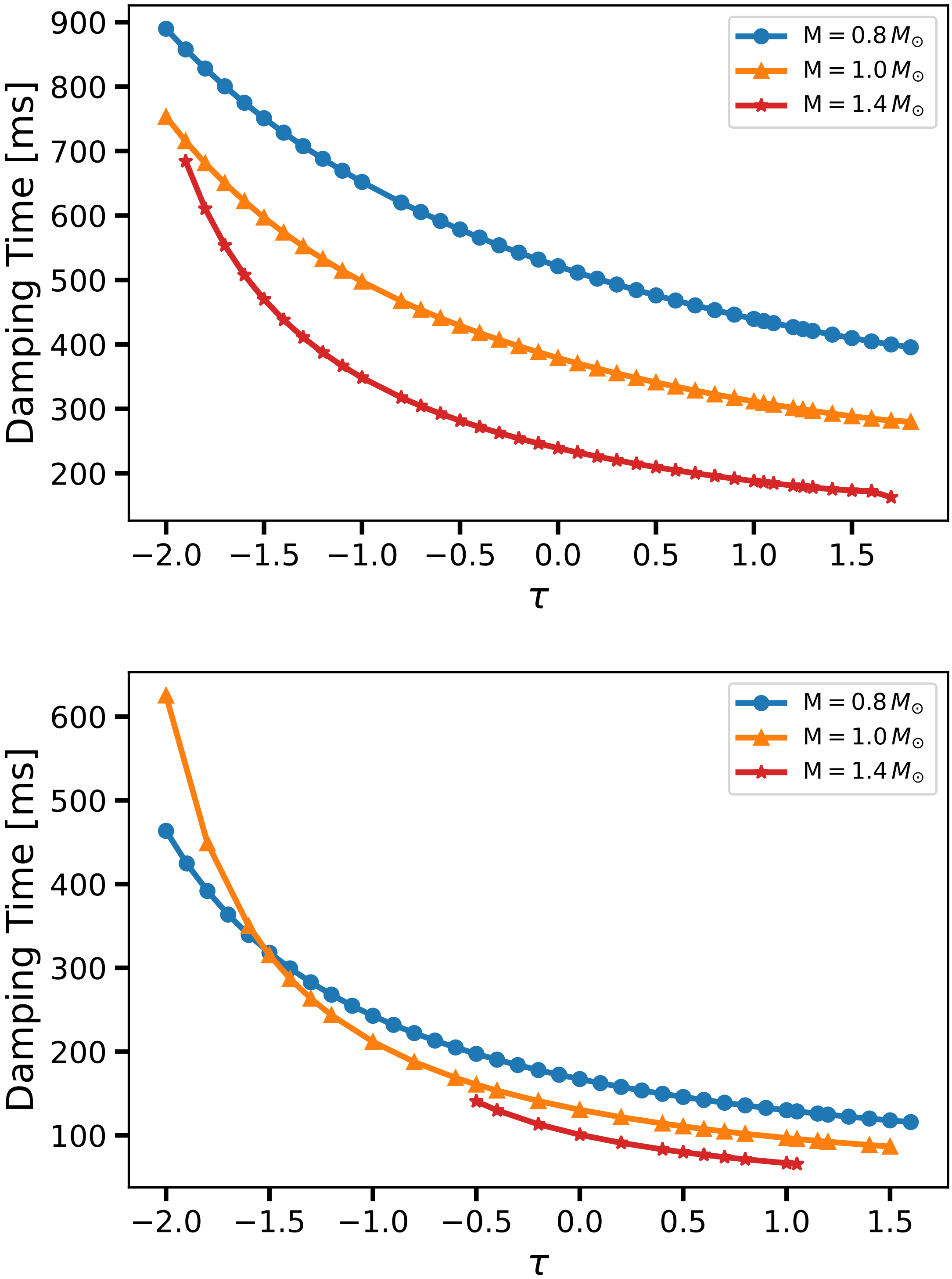

Figure 5.15: Dependence of the damping time of f-mode oscillations on the anisotropic strength τ for quark stars of fixed masses. Results for the MIT bag EoS are shown in the top panel, and those for EOS-A are displayed in the bottom panel.

In the next section, we will use the above findings to construct semi-empirical relations for the f-mode frequency in terms of mass, radius, and the anisotropic strength (τ) for both neutron stars and quark stars. Similarly, we will derive corresponding semi-empirical expressions for the damping time using the same set of stellar parameters.

5.3 Expressions for the frequency and the damping time as a function of mass, radius, and the anisotropic strength

In this section, we provide semi-empirical expressions for the f-mode oscillation frequency and damping time as functions of fundamental stellar parameters, namely, the total mass, radius, and the pressure anisotropy strength. These relations are constructed separately for neutron stars and quark stars and capture the dependence of oscillation properties on the underlying structural characteristics.

5.3.1 Expression for the frequency

As demonstrated in Figs. 5.2 and 5.10, the f-mode frequency $\mathcal{F}$ exhibits an approximately linear dependence on the square root of the average density. The anisotropic parameter τ modifies both the slope and intercept of the $\mathcal{F}-\sqrt{\rho_{\text{avg}}}$ relation. The empirical expression, previously shown in Eq. (5.12), is written as

$$\mathcal{F}(M,R,\tau) \approx C(\tau)\sqrt{\frac{3}{4\pi}}\sqrt{\frac{M}{R^3}} + D(\tau), \tag{5.14}$$

where the average density is defined as $\rho_{\text{avg}} = M\left[(4/3)\pi R^3\right]^{-1}$.

To determine the coefficients $C(\tau)$ and $D(\tau)$, we calculate $\mathcal{F}$ for a set of stable stellar models. For neutron stars, the mass range considered spans from 1.0 $\text{M}_\odot$ up to the respective maximum stable mass. For quark stars, the range extends from 0.8 $\text{M}_\odot$ to the corresponding maximum mass. The anisotropy parameter τ is varied from -2 to 1.7 for the BSk21 EoS and from -2 to 1.55 for the BSk19 EoS. For quark stars, τ ranges from -2 to 1.8 for the MIT bag EoS and from -2 to 1.6 for EOS-A.

At each fixed value of τ, we perform a linear fit between $\mathcal{F}$ and $\sqrt{3M/(4\pi R^3)}$. The slope and intercept of this fit yield $C(\tau)$ and $D(\tau)$, respectively. In this analysis, M is given in $M_\odot$, R in kilometers, and $\mathcal{F}$ in kilohertz.

We then fit $C(\tau)$ and $D(\tau)$ separately for each EoS using third-order polynomials in τ:

$$C(\tau) = c_0 + c_1\tau + c_2\tau^2 + c_3\tau^3, \tag{5.15}$$

$$D(\tau) = d_0 + d_1\tau + d_2\tau^2 + d_3\tau^3, \tag{5.16}$$

where c_0, c_1, c_2, and c_3 are the polynomial coefficients for $C(\tau)$, and d_0, d_1, d_2, and d_3 are those for $D(\tau)$. The best-fit parameters for all EsoS, corresponding to both neutron stars and quark stars are listed in Tables 5.5 and 5.6.

Table 5.5: Fitting parameters for $C(\tau)$ for various EsoS of neutron stars and quark stars. The parameters c_0, c_1, c_2, and c_3 are obtained from polynomial fitting.

EoS	c_0	c_1	c_2	c_3
BSk19	89.5917	13.6593	−9.2322	5.4053
BSk21	84.8297	17.7921	−10.0205	2.1940
MIT bag	121.1240	18.4186	−2.1998	13.1095
EOS-A	87.8584	12.3431	−6.7491	28.0644

Table 5.6: Fitting parameters for $D(\tau)$ for various EsoS of neutron stars and quark stars. The parameters d_0, d_1, d_2, and d_3 are obtained from polynomial fitting.

EoS	d_0	d_1	d_2	d_3
BSk19	0.7112	−0.0915	0.1122	−0.0761
BSk21	0.6182	−0.1313	0.1066	−0.0246
MIT bag	−0.1817	−0.1777	0.0261	−0.1995
EOS-A	0.5130	−0.0936	0.1472	−0.7172

We have also assessed the accuracy of the fits by computing the coefficient of determination $\mathcal{R}^2$, defined as [155, 156]:

$$\mathcal{R}^2 = 1 - \frac{\sum_i (Y_{ni} - Y_{fi})^2}{\sum_i (Y_{ni} - \bar{Y})^2}, \tag{5.17}$$

where Y_n denotes the numerically calculated value of the quantity Y (in this case, the f-mode frequency), Y_f is the corresponding value obtained from the fit, and $\bar{Y}$ is the mean of the numerically computed values. An $\mathcal{R}^2$ value above 0.95 typically indicates an excellent fit and suggests that the fitted relation accurately captures the functional dependence. For neutron stars, we find $\mathcal{R}^2 = 0.9976$ for the BSk21 EoS and $\mathcal{R}^2 = 0.9980$ for BSk19. For quark stars, the values are 0.9971 for the MIT bag EoS and 0.9972 for EOS-A, confirming an excellent fit in all cases.

For visual representation, Fig. 5.16 plots τ along the horizontal axis and the corresponding values of C (top panel) and D (bottom panel) along the vertical axis for neutron star EosS. Discrete points indicate values obtained from the linear fits between $\mathcal{F}$ and $\sqrt{3M/(4\pi R^3)}$, while the solid lines represent the fitted curves using Eqs. (5.15) and (5.16) with the coefficients listed in Tables 5.5 and 5.6. Similarly, for quark stars, the fitted parameters are also listed in the same tables, and the corresponding plots are shown in Fig. 5.17.

From these plots, we observe that the slope $C(\tau)$ increases monotonically with τ, whereas the intercept $D(\tau)$ decreases monotonically. Another notable feature is that the influence of anisotropy becomes significantly more pronounced for $|\tau| \gtrsim 1$.

5.3.2 Expression for the damping time

We have already observed in Figs. 5.6 and 5.13 that the normalized inverse damping time, $(\mathfrak{T} M^3/R^4)^{-1}$, decreases linearly with increasing compactness M/R, and that the anisotropic strength τ affects the slope and intercept of these fitted lines. The approximate functional form was given in Eq. (5.13). Here, we aim to extract the explicit forms

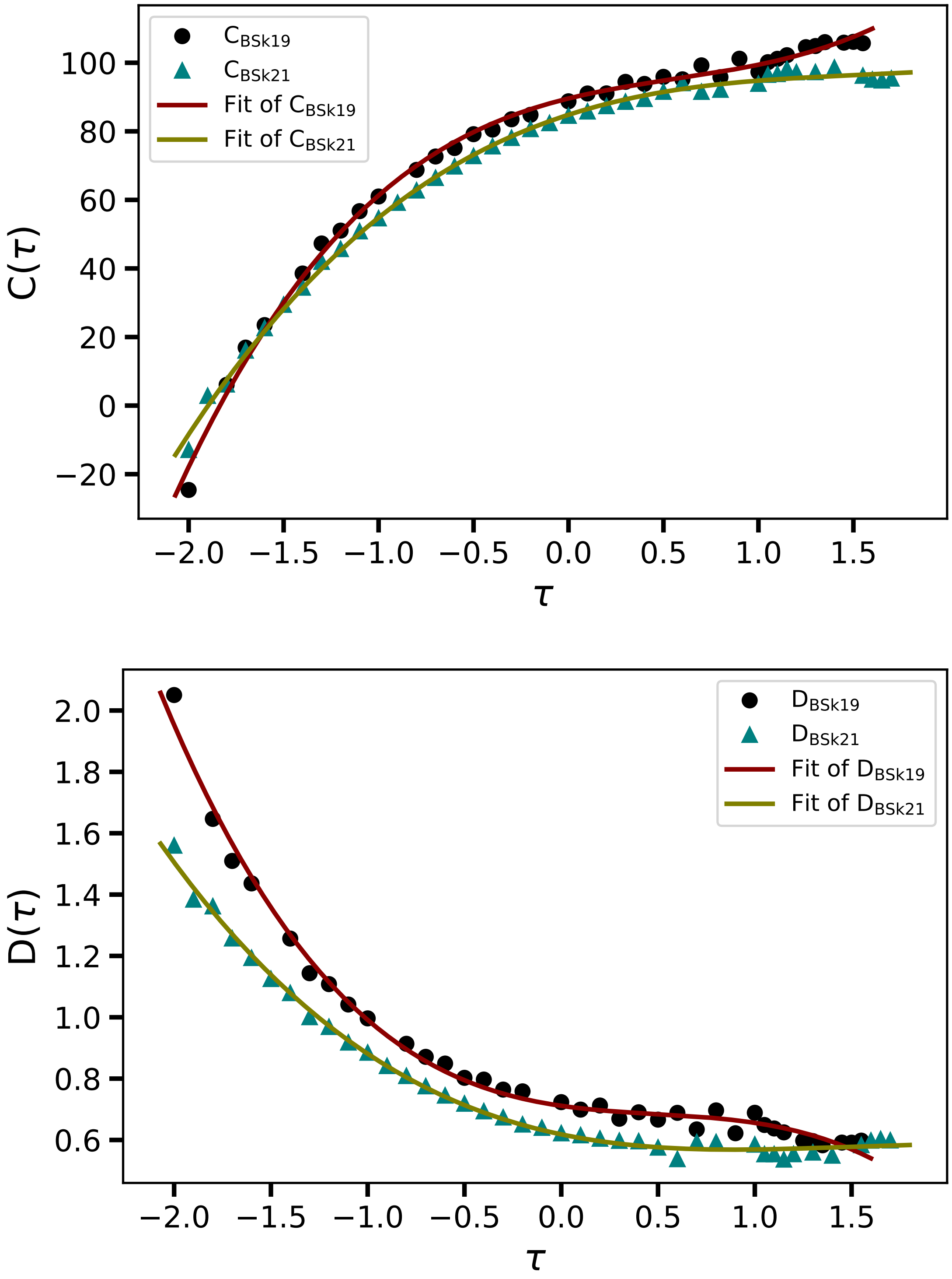

Figure 5.16: Variation of $C(\tau)$ (top panel) and $D(\tau)$ (bottom panel) with anisotropic strength τ for neutron stars modeled using the BSk19 and BSk21 EsoS. The discrete points denote the numerically obtained values of the slope C and intercept D from the linear fits to the $\mathcal{F} - \sqrt{\rho_{\mathrm{avg}}}$ relation, while the solid lines represent the corresponding polynomial fits. The subscripts in C and D indicate the respective EoS.

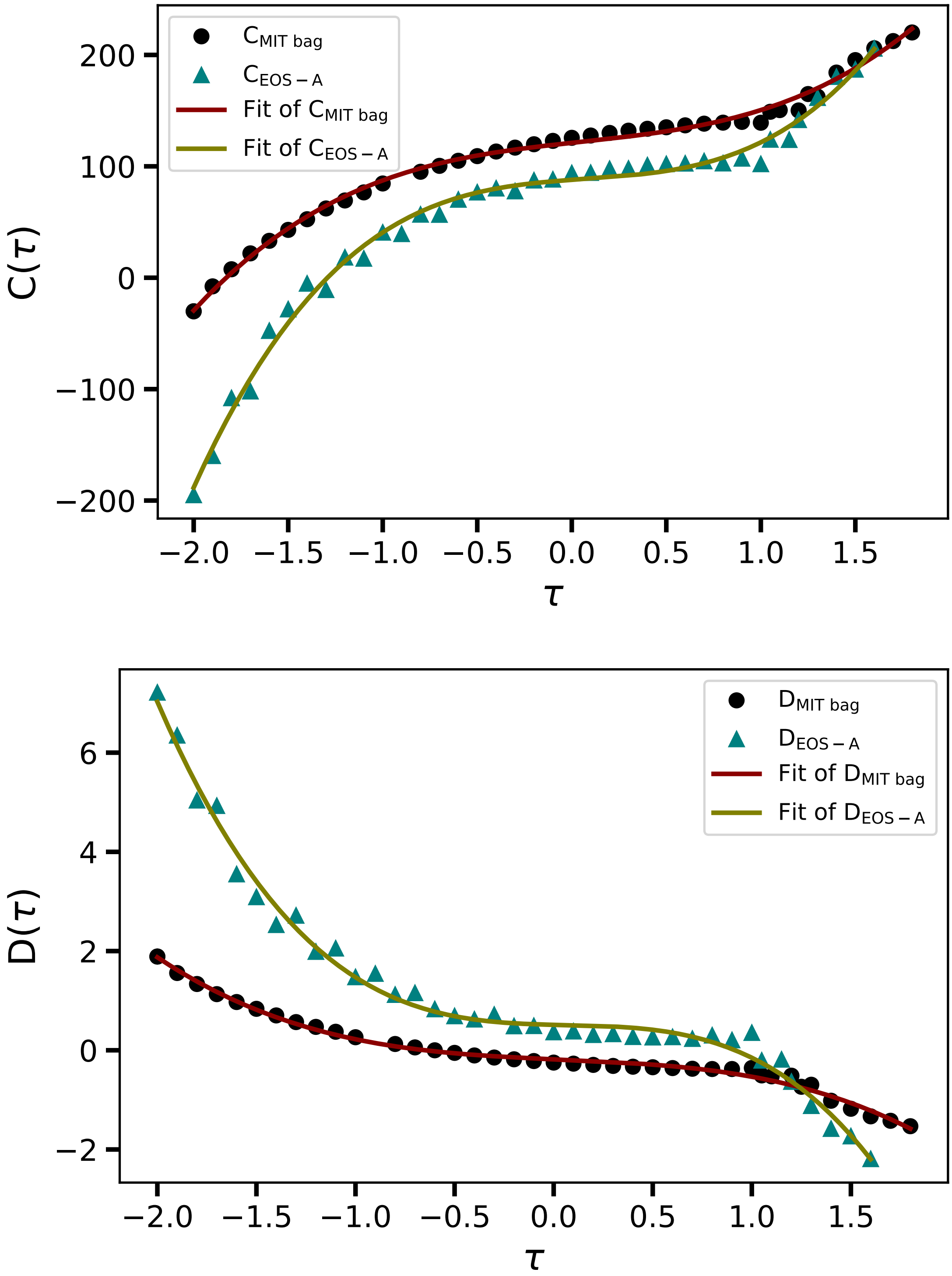

Figure 5.17: Variation of $C(\tau)$ (top panel) and $D(\tau)$ (bottom panel) with anisotropic strength τ for quark stars described by the MIT bag EoS and EOS-A. The discrete points indicate the numerically obtained values of the slope C and intercept D from the linear fits to the $\mathcal{F} - \sqrt{\rho_{\text{avg}}}$ relation, while the solid lines represent the corresponding polynomial fits. The subscripts in C and D refer to the respective EoS.

Table 5.7: Fitting parameters for $J(\tau)$ for two EsoS of neutron stars.

EoS	j_0	j_1	j_2	j_3	j_4	j_5	j_6
BSk19	−414.344	−54.361	−33.4275	127.115	36.0197	−62.9205	−25.1926
BSk21	−377.305	−36.5586	−68.2963	132.723	57.8742	−64.272	−29.1236

Table 5.8: Fitting parameters for $K(\tau)$ for two EsoS of neutron stars.

EoS	k_0	k_1	k_2	k_3	k_4	k_5	k_6
BSk19	87.3733	17.0643	2.9601	−8.69491	−2.74845	4.6428	1.8490
BSk21	82.6276	12.6987	4.73284	−8.16611	−3.39565	4.82892	2.08444

of $J(\tau)$ and $K(\tau)$.

First, we compute the values of $(\mathfrak{I}M^3/R^4)^{-1}$ across a range of stable compact star masses, using the same mass and anisotropy ranges as described in subsection 5.3.1. For each fixed value of τ, we perform a linear fit between $(\mathfrak{I}M^3/R^4)^{-1}$ and M/R. The slope of each fit gives the value of $J(\tau)$, while the intercept provides $K(\tau)$. As before, M is in solar mass units ($M_\odot$), R is in kilometers (km), and $\mathfrak{I}$ is in milliseconds (ms).

Next, we fit $J(\tau)$ and $K(\tau)$ separately for the two EsoS. For neutron stars, the best fits are obtained using sixth-order polynomials in τ:

$$J(\tau) = j_0 + j_1\tau + j_2\tau^2 + j_3\tau^3 + j_4\tau^4 + j_5\tau^5 + j_6\tau^6, \tag{5.18}$$

$$K(\tau) = k_0 + k_1\tau + k_2\tau^2 + k_3\tau^3 + k_4\tau^4 + k_5\tau^5 + k_6\tau^6, \tag{5.19}$$

where j_i and k_i ($i = 0$ to 6) are the fitting coefficients. The best-fit parameters for the neutron star EsoS are provided in Tables 5.7 and 5.8. The quality of these fits is evaluated using the coefficient of determination $\mathcal{R}^2$ (see Eq. 5.17), yielding values of 0.9773 for BSk19 and 0.9638 for BSk21—indicating excellent agreement between fit and numerical data.

On the other hand, for quark stars, the optimal fits are obtained with fourth-order polyno-

Table 5.9: Fitting parameters for $J(\tau)$ for two EsoS. The parameters j_0, j_1, j_2, j_3, and j_4 correspond to the coefficients obtained from the fit.

EoS	j_0	j_1	j_2	j_3	j_4
MIT bag	−175.9430	15.0989	−3.5854	1.4289	−0.3524
EOS-A	−171.4760	−8.1686	−2.6170	5.9472	2.1901

Table 5.10: Fitting parameters for $K(\tau)$ for two EsoS. The parameters k_0, k_1, k_2, k_3, and k_4 correspond to the coefficients obtained from the fit.

EoS	k_0	k_1	k_2	k_3	k_4
MIT bag	45.1012	5.4740	0.2597	−0.2780	−0.0175
EOS-A	43.7257	8.6682	0.2338	−0.8676	−0.3018

mials in τ:

$$J(\tau) = j_0 + j_1\tau + j_2\tau^2 + j_3\tau^3 + j_4\tau^4, \tag{5.20}$$

$$K(\tau) = k_0 + k_1\tau + k_2\tau^2 + k_3\tau^3 + k_4\tau^4, \tag{5.21}$$

where j_i and k_i ($i = 0$ to 4) are the fitting parameters. These coefficients are listed in Tables 5.9 and 5.10. The fits yield $\mathcal{R}^2 = 0.9988$ for the MIT bag EoS and $\mathcal{R}^2 = 0.9869$ for EOS-A, confirming excellent agreement between the fit and numerical data.

For visual representation, Fig. 5.18 shows the variation of J (top panel) and K (bottom panel) with the anisotropic strength τ for neutron stars. The discrete points represent the numerical values obtained from linear fits between $(\mathfrak{I}M^3/R^4)^{-1}$ and M/R, while the solid lines correspond to the fitted curves based on Eqs. (5.18) and (5.19) using the coefficients listed in Tables 5.7 and 5.8. Similarly, for quark stars, Fig. 5.19 presents the corresponding J and K values as functions of τ, along with the polynomial fits derived from the parameters given in Tables 5.9 and 5.10.

In this chapter, we have numerically solved the complete set of linear perturbation equations governing the f-mode oscillations of anisotropic neutron stars and quark stars in general relativity. We have shown that the f-mode frequency scales approximately linearly with the square root of the average density, whereas the normalized inverse damping

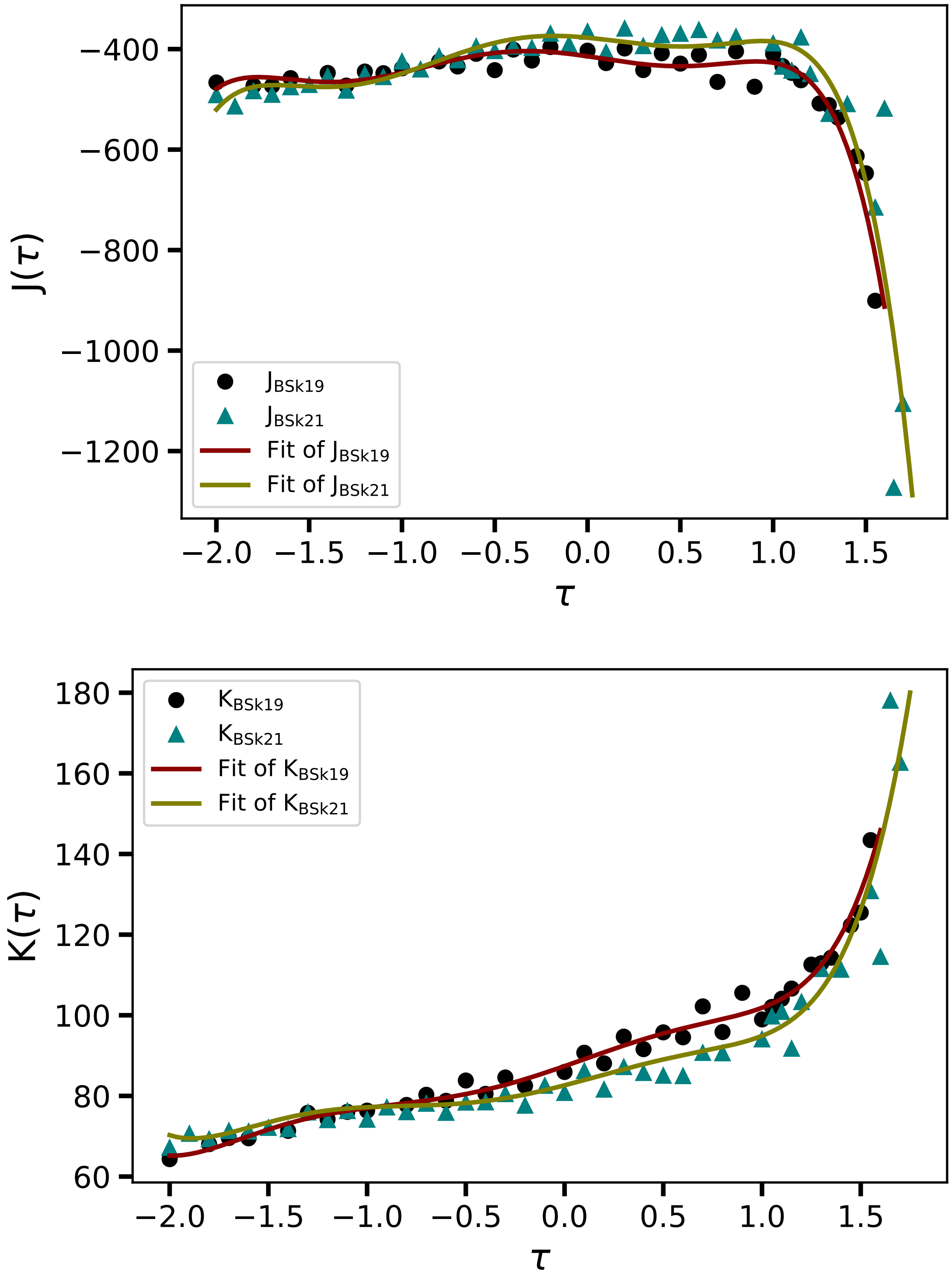

Figure 5.18: Variation of $J(\tau)$ (top panel) and $K(\tau)$ (bottom panel) with anisotropic strength τ for neutron stars described by the BSk19 and BSk21 EsoS. The discrete points indicate the numerically obtained slope J and intercept K from the linear fits to the $(\mathfrak{I}M^3/R^4)^{-1}$ versus M/R relation, while the solid lines represent the corresponding polynomial fits. The subscripts in J and K denote the respective EoS.

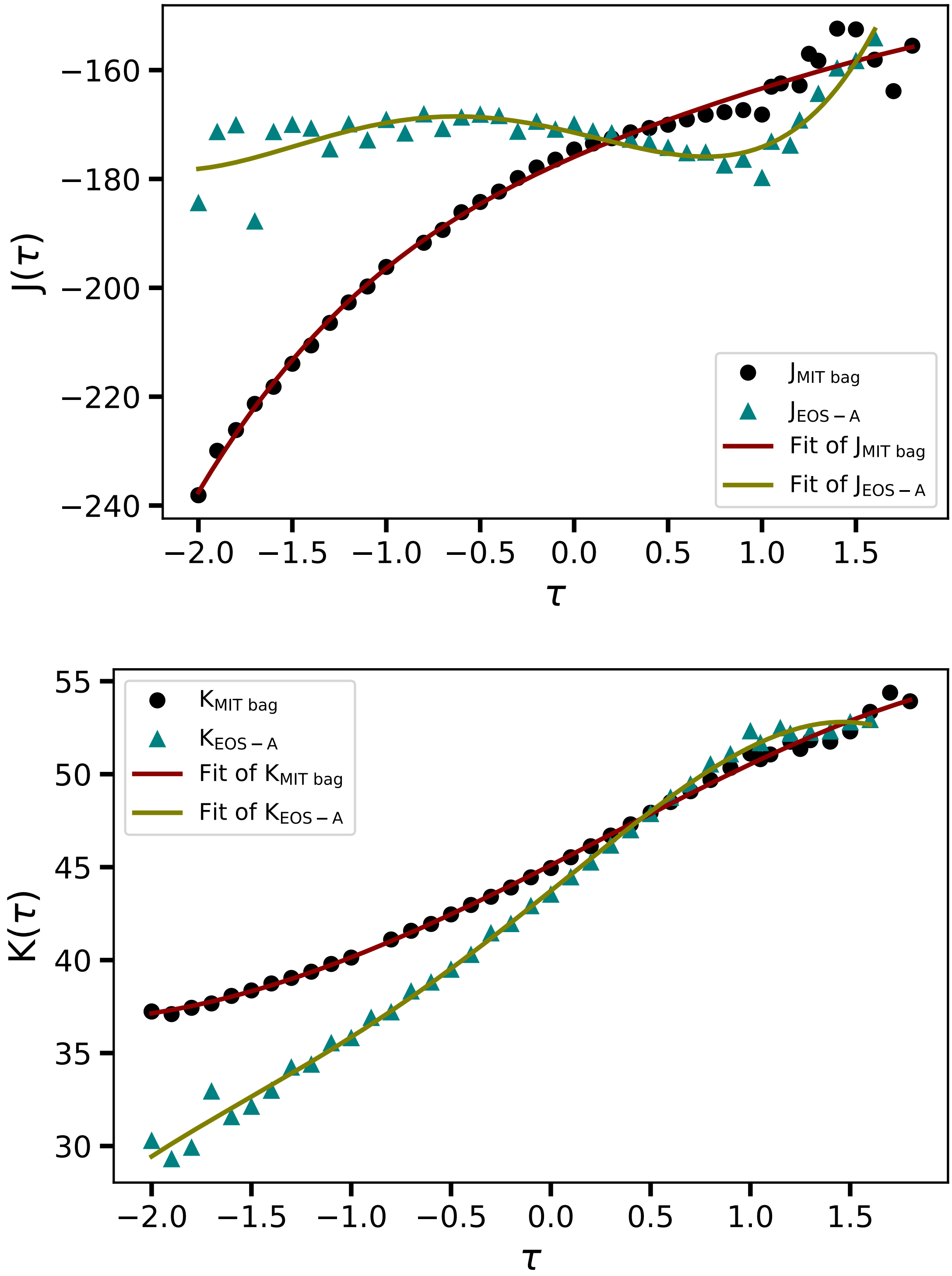

Figure 5.19: Variation of $J(\tau)$ (top panel) and $K(\tau)$ (bottom panel) with anisotropic strength τ for quark stars described by the MIT bag EoS and EOS-A. The discrete points show the numerically extracted slope J and intercept K from the linear fits to the $(\mathfrak{I}M^3/R^4)^{-1}$ versus M/R relation, while the solid lines represent the corresponding polynomial fits. The subscripts in J and K indicate the respective EoS.

time varies linearly with the compactness. The anisotropic parameter τ modifies both the slope and intercept of these relations, with stronger effects at higher stellar masses. For neutron stars, the frequency increases with τ for lower masses but decreases for massive stars due to the steep reduction in average density. Similar trends are observed in the case of quark stars, although the sensitivity to anisotropy and the threshold masses depend on the choice of the EoS.

To quantitatively capture these dependencies, we have introduced semi-empirical expressions for both the f-mode frequency and damping time as functions of mass, radius, and anisotropic strength. For all models considered, the frequency fits involve third-order polynomials in τ, while the damping time fits require sixth-order polynomials for neutron stars and fourth-order polynomials for quark stars. These relations exhibit excellent agreement with the numerical results and may serve as useful tools for interpreting gravitational wave signals from compact stars, particularly in scenarios where pressure anisotropy cannot be neglected.

Chapter 6

Summary and Conclusion

In this thesis, we have investigated the quasi-normal f-modes of anisotropic compact stars within the framework of full general relativity. To accomplish this, we employed linear perturbation theory, incorporating both metric and fluid perturbations to derive the governing equations for stellar oscillations. While the resulting equations resemble those for isotropic stars in structure, those include additional terms that capture the effects of pressure anisotropy, specifically, the difference between radial and tangential pressure and their respective perturbations. Using this formalism, we computed the characteristic f-mode frequencies for a range of neutron star and quark star models. Our results demonstrate that both the oscillation frequency and the damping time are significantly influenced by the presence of pressure anisotropy within the star.

In Chapter 2, as a pedagogical introduction, we reviewed the f-mode frequency within the framework of Newtonian theory, assuming that the stellar structure is governed by Newtonian gravity. By analyzing perturbations in this context, we derived the well-known relation that the f-mode frequency scales linearly with the square root of average density of the star. This classical result serves as a useful reference point and provides physical intuition for oscillation dynamics. Importantly, this simplified model motivates the transition to a more rigorous treatment using general relativity, which is essential for accurate description of compact stars such as neutron stars and quark stars.

In Chapter 3, we studied the equilibrium configuration of anisotropic compact stars in general relativity. This is a preparatory step for computing oscillation frequencies and is based on existing work. To model anisotropy realistically, we adopted two different equations of state (EsoS) for neutron stars and two EsoS for quark stars to describe the radial pressure. For the tangential pressure, we employed an ansatz specifically designed to satisfy appropriate boundary conditions. Our analysis revealed that increasing the tangential pressure relative to the radial pressure results in a higher total enclosed mass of the star, highlighting the significant impact of anisotropy on stellar structure.

In Chapter 4, we presented our new work: a full general relativistic formulation of the perturbation equations governing polar-type non-radial oscillations of anisotropic compact stars. Using the Regge-Wheeler gauge, explained in Appendix A, we systematically derived the equations governing the metric and fluid perturbations. We clearly highlighted the additional terms arising specifically due to anisotropic pressure, which differentiate these equations from their isotropic counterparts. Appropriate boundary conditions at the stellar center and surface were also rigorously discussed. This chapter thus laid the theoretical groundwork necessary for analyzing the impact of pressure anisotropy on the quasi-normal modes of neutron stars and quark stars.

In Chapter 5, we have carried out an extensive numerical study of the perturbation equations derived in Chapter 4, focusing on determining the quasi-normal $f-$ mode frequencies and damping times of anisotropic neutron stars and quark stars. We systematically examined the impact of pressure anisotropy using realistic equations of state, specifically the BSk19 and BSk21 models for neutron stars, and the MIT Bag model along with an interacting quark matter model (EOS-A) for quark stars. Our analysis demonstrates that the f-mode frequencies exhibit a linear relationship with the square root of the average stellar density for both isotropic and anisotropic compact stars. Importantly, the slope of this linear relationship depends significantly on the anisotropic strength τ, it increases for positive values of τ and decreases for negative values. Such a linear dependence was previously noted within a Newtonian framework by Hillebrandt and Steinmetz [108]. Since the mass of a compact star can be observationally determined through electromagnetic signals, we also analyzed the dependence of frequency and damping time on stellar mass. Our findings reveal that the qualitative behavior of these variations remains consistent for both isotropic and anisotropic configurations. As illustrated in Fig. 11, the frequency increases with greater anisotropic strength for neutron stars of masses 1 and 1.4 $M_{\odot}$. However, for a more massive neutron star (2.274 $M_{\odot}$), we observe a reduction in frequency with increasing anisotropic strength. This difference arises due to the rapid decrease in the square root of average density as anisotropy increases in massive stars, contrasted with the slow decrease observed for neutron stars with masses close to the solar mass, as depicted in Fig. 8. A similar trend is confirmed for quark stars. Additionally, we have found that the inverse normalized damping time is linearly related to the compactness of the star. Generally, for a fixed anisotropic strength, the damping time decreases as the stellar mass increases, except in cases involving quark stars with strongly negative values of τ. Moreover, for stars of fixed mass, the damping time decreases systematically as the anisotropy parameter τ increases. Using the calculated values of frequency and damping time, we obtain semi-empirical relations that express frequency and damping time in terms of the intrinsic properties of compact stars, such as mass, radius, and the anisotropic strength within the star. We find that the frequency exhibits a cubic polynomial dependence on the anisotropy strength parameter, while the damping time shows a sextic dependence for neutron stars and a quartic dependence for quark stars.

Our investigation offers valuable insights into the role of pressure anisotropy in the f-mode oscillations of compact stars. Previous analyses utilizing Newtonian gravity or the Cowling approximation provided preliminary perspectives on how anisotropy influences the internal structure and oscillatory behavior of these stars. However, our current work extends beyond these earlier approximations by incorporating full general relativistic perturbations, including both metric and fluid components. This comprehensive approach allows for a more accurate characterization of f-mode frequencies and their corresponding damping times, directly linked to energy dissipation through gravitational wave emission. These observable quantities, namely the frequency and damping time of the f-modes, serve as distinct astrophysical signatures encapsulating crucial stellar properties, such as mass, radius, and the degree of anisotropy.

Although we employed realistic equations of state in our study, the precise characterization of anisotropy remains an approximation due to limitations in current observational and theoretical constraints. Thus, future studies need to delve deeper into the detailed nature of anisotropic pressures, enhancing our understanding of compact stars at both microscopic and macroscopic levels. Furthermore, our present analysis focuses exclusively on the f-mode oscillations. Investigating the impact of pressure anisotropy on other non-radial oscillation modes, such as p-modes and w-modes, would provide complementary insights and broaden our comprehension of anisotropic compact star behavior. Additionally, since compact stars, especially neutron stars, often exhibit rapid rotation, incorporating rotational effects into the perturbation framework would yield a more realistic and comprehensive picture.

Appendix A

Regge-Wheeler Gauge

Since we are analyzing perturbations for a non-rotating neutron star, the background spacetime remains spherically symmetric. As a result, perturbations can be decomposed into angular components that depend on the coordinates θ and ϕ, while the remaining terms are functions of the radial coordinate and time.

To achieve this decomposition, we expand the angular dependence of the perturbations using spherical harmonics $Y_l^m(\theta, \phi)$. This approach allows us to separate the angular and the radial dependencies, significantly simplifying the analysis. However, use of only scalar spherical harmonics does not completely eliminate the angular dependence. To preserve the symmetry of the background, we must select appropriate spherical harmonics that ensure the expansion coefficients remain independent of the angular coordinates, thereby simplifying the perturbation equations.

The perturbed metric, as defined in Eq. (4.2), can be expressed as the sum of the background metric $g^{(B)}_{\mu\nu}$ and a small perturbation $h_{\mu\nu}$. The explicit form of the perturbation matrix is given by:

$$h_{\mu\nu} = \begin{bmatrix} h_{tt} & h_{tr} & h_{t\theta} & h_{t\phi} \\ h_{tr} & h_{rr} & h_{r\theta} & h_{r\phi} \\ h_{t\theta} & h_{r\theta} & h_{\theta\theta} & h_{\theta\phi} \\ h_{t\phi} & h_{r\phi} & h_{\theta\phi} & h_{\phi\phi} \end{bmatrix}. \tag{A.1}$$

Since we are primarily concerned with the rotational properties on a 2-sphere (S^2), it is useful to examine how different components of $h_{\mu\nu}$ transform under rotations in the angular coordinates.

The components h_{tt}, h_{rr}, and $h_{tr} = h_{rt}$ are scalars under rotation, meaning they remain independent of θ and ϕ. The elements $[h_{t\theta}\ h_{t\phi}]$ and $[h_{r\theta}\ h_{r\phi}]$ behave as vectors under rotation, as they carry a single angular index (θ or ϕ). The submatrix

$$\begin{bmatrix} h_{\theta\theta} & h_{\theta\phi} \\ h_{\theta\phi} & h_{\phi\phi} \end{bmatrix}, \tag{A.2}$$

transforms as a rank-2 tensor under rotation, as it contains two angular indices (θ, ϕ).

By appropriately decomposing the metric perturbations, we ensure that the resulting perturbation equations remain well-structured and independent of angular coordinates, aligning with the Regge-Wheeler gauge formalism.

From the above discussion, it follows that the choice of angular dependence must reflect the transformation properties of $h_{\mu\nu}$ under rotation. Scalar components can be expanded using scalar spherical harmonics, $Y_l^m(\theta, \phi)$, while vector and tensor components require vector and tensor spherical harmonics, respectively, as defined below:

$$\begin{aligned} \left(\overset{1}{V}{}_l^m\right)_a &= \nabla_a(S_l^m) \\ &= \frac{\partial}{\partial x^a} Y_l^m(\theta, \phi) \end{aligned}$$

$$= \begin{bmatrix} \frac{\partial}{\partial\theta} Y_l^m \\ \frac{\partial}{\partial\phi} Y_l^m \end{bmatrix}, \tag{A.3}$$

where x^a is coordinate on the three dimensional space, $S_l^m = Y_l^m$ is the scalar spherical harmonics.

$$\begin{aligned} \left(\overset{2}{V}{}_l^m\right)_a &= \epsilon^b{}_a \nabla_b (S_l^m) \\ &= \gamma^{bc} \epsilon_{ac} \frac{\partial}{\partial x^b} Y_l^m(\theta, \phi) \\ &= \begin{bmatrix} -\frac{1}{\sin(\theta)} \frac{\partial}{\partial\phi} Y_l^m \\ \sin(\theta) \frac{\partial}{\partial\phi} Y_l^m \end{bmatrix}, \end{aligned} \tag{A.4}$$

where γ_{ab} is the metric on the 2-sphere.

$$\begin{aligned} \left(\overset{1}{T}{}_l^m\right)_{ab} &= \nabla_b \nabla_a (S_l^m) \\ &= \frac{\partial^2}{\partial x^a \partial x^b} - \Gamma^k_{ab} \frac{\partial}{\partial x^k} Y_l^m \\ &= \begin{bmatrix} \frac{\partial^2}{\partial\theta^2} Y_l^m & \frac{\partial^2}{\partial\theta\partial\phi} Y_l^m - \cot(\theta) \frac{\partial}{\partial\phi} Y_l^m \\ \frac{\partial^2}{\partial\theta\partial\phi} Y_l^m - \cot(\theta) \frac{\partial}{\partial\phi} Y_l^m & \frac{\partial^2}{\partial\phi^2} Y_l^m + \sin(\theta)\cos(\theta) \frac{\partial}{\partial\theta} Y_l^m \end{bmatrix}, \end{aligned} \tag{A.5}$$

$$\left(\overset{2}{T}{}_l^m\right)_{ab} = S_l^m \gamma_{ab}, \tag{A.6}$$

$$\left(\overset{3}{T}{}_l^m\right)_{ab} = \frac{1}{2} \left[\epsilon_a{}^c \nabla_b \nabla_c (S_l^m) + \epsilon_b{}^c \nabla_a \nabla_c (S_l^m) \right]. \tag{A.7}$$

In all the above equations the indices a, b, c range from 2 to 3. The 2-sphere metric γ_{ab} is known as:

$$\gamma_{ab} = \mathrm{diag}(1, \sin^2\theta).$$

The symbol ϵ represents the totally antisymmetric tensor in two dimensions:

$$\epsilon = \sin\theta \begin{bmatrix} 0 & -1 \\ 1 & 0 \end{bmatrix}.$$

Here, all covariant derivatives are taken on the 2-sphere. This establishes the necessity of using scalar, vector, and tensor spherical harmonics to describe perturbations in a spherically symmetric spacetime.

The parity of scalar, vector, and tensor spherical harmonics plays a crucial role in the decomposition of the perturbation tensor. Parity refers to how a function transforms under spatial inversion, defined as $(\theta, \phi) \to (\pi - \theta, \pi + \phi)$. A function that remains unchanged under this transformation is said to have even parity, whereas a function that changes sign is said to have odd parity. In relativistic perturbation theory, functions transforming as $(-1)^l$ are classified as even (polar), while those transforming as $(-1)^{l+1}$ are classified as odd (axial). To emphasize this distinction, Chandrasekhar [157] introduced the terminology "polar" and "axial" to refer to perturbations with parity $(-1)^l$ and $(-1)^{l+1}$, respectively.

To determine whether the functions in Eq. (A.3) are polar or axial, we analyze their transformation properties under spatial inversion. However, it is important to note that the explicit expression of perturbation functions depends on the choice of gauge, meaning that their coordinate representation alone does not uniquely determine their parity. Nevertheless, we can use the well-established property that the gradient of a function preserves its parity, whereas the application of a totally antisymmetric tensor reverses it.

From these definitions, we conclude that the scalar spherical harmonic Y_l^m transforms as $(-1)^l$ under inversion, making it a polar function. Consequently, the scalar spherical harmonic expansion $S_l^m = Y_l^m$ is also classified as polar.

For vector spherical harmonics, $\left(\overset{1}{V}{}_l^m\right)_a$ consists of derivatives of Y_l^m with respect to x^a, thereby preserving the same polar parity as Y_l^m. In contrast, $\left(\overset{2}{V}{}_l^m\right)_a$ involves a multiplication by the antisymmetric tensor ϵ_{ac}, which flips its parity, making it axial (i.e., transforming as $(-1)^{l+1}$). Similarly, the tensor harmonics $\left(\overset{1}{T}{}_l^m\right)_{ab}$ and $\left(\overset{2}{T}{}_l^m\right)_{ab}$ are polar, while $\left(\overset{3}{T}{}_l^m\right)_{ab}$ is axial due to the presence of the antisymmetric tensor.

Since the unperturbed metric remains unchanged under spatial inversion, the perturbation equations are expected to preserve this symmetry, ensuring that polar and axial components remain decoupled. Consequently, perturbations can be decomposed into distinct polar and axial contributions, allowing them to be analyzed separately.

We can now explicitly write the polar and axial perturbations using Eq. (A.3) as

$$h_{\mu\nu}^{\text{polar}} = \begin{bmatrix} e^{\nu}H_0(t,r)Y_l^m & H_1(t,r)Y_l^m & h_0(t,r)\left(\overset{1}{V}{}_l^m\right)_a^T \\ H_1(t,r)Y_l^m & e^{\lambda}H_2(t,r)Y_l^m & h_1(t,r)\left(\overset{1}{V}{}_l^m\right)_a^T \\ h_0(t,r)\left(\overset{1}{V}{}_l^m\right)_a & h_1(t,r)\left(\overset{1}{V}{}_l^m\right)_a & r^2G(t,r)\left(\overset{1}{T}{}_l^m\right)_{ab} + r^2K(t,r)\left(\overset{2}{T}{}_l^m\right)_{ab} \end{bmatrix} \tag{A.8}$$

and

$$h_{\mu\nu}^{\text{axial}} = \begin{bmatrix} 0 & 0 & h_0(t,r)\left(\overset{2}{V}{}_l^m\right)_a^T \\ 0 & 0 & h_1(t,r)\left(\overset{2}{V}{}_l^m\right)_a^T \\ h_0(t,r)\left(\overset{2}{V}{}_l^m\right)_a & h_1(t,r)\left(\overset{2}{V}{}_l^m\right)_a & \frac{h_2(t,r)}{2}\left(\overset{3}{T}{}_l^m\right)_{ab} \end{bmatrix} \tag{A.9}$$

where $h_{\mu\nu}^{\text{polar}}$ represents the even-parity (polar) perturbation, and $h_{\mu\nu}^{\text{axial}}$ represents the odd-parity (axial) perturbation. In the above matrices, H_0, H_1, H_2, K, G, h_0, h_1, and h_2 are functions of t and r that serve as expansion coefficients for the spherical harmonics.

After decomposing the perturbations into polar and axial components, we study them separately. However, so far, we have not specified a coordinate system to work with. Choosing an appropriate coordinate system is crucial, as it simplifies the equations significantly and eliminates non-physical coordinate effects. Since general relativity is a coordinate-independent theory, any physically meaningful quantity remains valid regardless of the chosen coordinate system.

From the above discussion, we conclude that in a spherically symmetric background, perturbations naturally decompose into polar and axial modes, which can be analyzed independently. However, general relativity allows us to choose a gauge (coordinate system) in which the perturbation matrix takes a more convenient form. To implement this, we introduce an infinitesimal coordinate transformation

$$x^{\alpha} \to x'^{\alpha} = x^{\alpha} + \xi^{\alpha} \, , \tag{A.10}$$

where ξ^{α} represents a small displacement in the coordinate system. This is a diffeomorphism, ensuring that the transformed metric obeys

$$\delta g_{\mu\nu} = \mathcal{L}_{\xi} g_{\mu\nu} = \nabla_{\nu}\xi_{\mu} + \nabla_{\mu}\xi_{\nu} \, . \tag{A.11}$$

Since the background metric is the Schwarzschild metric, the perturbed metric before and after the transformation are related by

$$h'_{\mu\nu} = h_{\mu\nu} + \nabla_{\nu}\xi_{\mu} + \nabla_{\mu}\xi_{\nu} \, . \tag{A.12}$$

From this equation, we see that we have the freedom to choose four arbitrary functions $\xi^{\alpha}(x)$ to simplify the perturbation equations.

Regge and Wheeler [140] introduced a specific gauge choice by selecting $\xi^{\alpha}(x)$ in such a way that all terms containing second-order angular derivatives, such as $\frac{\partial^2}{\partial_{\theta}\partial_{\phi}}, \frac{\partial^2}{\partial^2\theta}, \frac{\partial^2}{\partial^2\phi}$ vanish. This simplifies the perturbation equations significantly. In particular, this gauge choice sets $G(t,r) = 0$ for polar perturbations and $h_2(t,r) = 0$ for axial perturbations. However, we still have two additional degrees of freedom. To further simplify the equations, we also set $h_0(t, r) = 0$ and $h_1(t, r) = 0$ for the polar perturbations.

A general 4-dimensional gauge vector can be written as

$$\xi^\alpha = \begin{bmatrix} A_1(t, r) Y_l^m \\ A_2(t, r) Y_l^m \\ A_3(t, r \begin{pmatrix} \overset{1}{V}{}_l^m \end{pmatrix}_a + A_4(t, r) \begin{pmatrix} \overset{2}{V}{}_l^m \end{pmatrix}_a \end{bmatrix} , \tag{A.13}$$

where $A_1(t, r)$, $A_2(t, r)$, $A_3(t, r)$, and $A_4(t, r)$ are functions of t and r. The quantities $\begin{pmatrix} \overset{1}{V}{}_l^m \end{pmatrix}_a$ and $\begin{pmatrix} \overset{2}{V}{}_l^m \end{pmatrix}_a$ are vector harmonics defined in Eq. (A.3), with indices $a = 2, 3$.

Since polar and axial perturbations are decoupled, we separate their gauge transformations accordingly.

For axial perturbations, we set $A_1 = A_2 = A_3 = 0$, reducing the gauge vector to:

$$\xi^\alpha_{ax} = A_4(t, r) \begin{bmatrix} 0 \\ 0 \\ \begin{pmatrix} \overset{2}{V}{}_l^m \end{pmatrix}_a \end{bmatrix} = A_4(t, r) \begin{bmatrix} 0 \\ 0 \\ -\frac{1}{\sin(\theta)} \frac{\partial}{\partial \phi} Y_l^m \\ \sin(\theta) \frac{\partial}{\partial \theta} Y_l^m \end{bmatrix} . \tag{A.14}$$

Now, we determine the function $A_4(t, r)$ such that h_2' vanishes, where prime denotes the differentiation with respect to r. From Eq. (A.12), considering the $(2, 2)$ component:

$$h'_{22} = h_{22} + 2\nabla_2 \xi_2 . \tag{A.15}$$

Setting $h'_{22} = 0$, we obtain the condition:

$$A_4 = -\frac{h_2}{2} . \tag{A.16}$$

Since we have already determined the expression for h_2, we can now compute A_4 to ensure that h_{22} is set to zero. This completes the choice of the gauge vector for axial perturbations.

Similarly, we now compute the components of the gauge vector for polar perturbations. The gauge vector for polar perturbations can be obtained by setting $A_4 = 0$ in Eq. (A.13), yielding:

$$\xi^{\alpha}_{\text{pol}} = \begin{bmatrix} A_1(t,r)Y_l^m \\ A_2(t,r)Y_l^m \\ A_3(t,r)\frac{\partial}{\partial\theta}Y_l^m \\ A_3(t,r)\frac{1}{\sin^2\theta}\frac{\partial}{\partial\phi}Y_l^m \end{bmatrix}. \tag{A.17}$$

To enforce the conditions $G = 0$, $h_0 = 0$, and $h_1 = 0$ in the transformed coordinate system, we compute the differential equations:

$$h'_{02} = h_{02} + \nabla_0\xi_2 + \nabla_2\xi_0, \tag{A.18}$$

$$h'_{12} = h_{12} + \nabla_1\xi_2 + \nabla_2\xi_1, \tag{A.19}$$

$$h'_{32} = h_{32} + \nabla_3\xi_2 + \nabla_2\xi_3. \tag{A.20}$$

Solving these equations expresses A_1, A_2, and A_3 in terms of G, h_0, and h_1. Using this gauge vector, we set the values of G, h_0, and h_1 in the transformed coordinate system to zero.

With this gauge choice, we can now express the metric perturbations in their final simplified forms. The axial perturbation metric takes the form:

$$h^{\text{axial}}_{\mu\nu} = \begin{bmatrix} 0 & 0 & -h_0(t,r)\left(\frac{\partial}{\sin\theta\partial\varphi}\right)Y_l^m & h_0(t,r)\left(\frac{\sin\theta}{\partial\theta}\right)Y_l^m \\ 0 & 0 & -h_1(t,r)\left(\frac{\partial}{\sin\theta\partial\varphi}\right)Y_l^m & h_1(t,r)\left(\frac{\sin\theta}{\partial\theta}\right)Y_l^m \\ \text{Sym} & \text{Sym} & 0 & 0 \\ \text{Sym} & \text{Sym} & 0 & 0 \end{bmatrix} \tag{A.21}$$

Similarly, the polar perturbation metric is given by:

$$h_{\mu\nu}^{\text{polar}} = \begin{bmatrix} e^{\nu} H_0(t,r) Y_l^m & H_1(t,r) Y_l^m & 0 & 0 \\ H_1(t,r) Y_l^m & e^{\lambda} H_2(t,r) Y_l^m & 0 & 0 \\ 0 & 0 & r^2 K(t,r) Y_l^m & 0 \\ 0 & 0 & 0 & r^2 K(t,r) \sin^2\theta Y_l^m \end{bmatrix} \tag{A.22}$$

In our analysis, we assume a harmonic time dependence characterized by the angular frequency ω.

Appendix B

Eulerian and Lagrangian Perturbations

In perturbation theory applied to fluid systems, two primary descriptions are used to quantify the changes in physical quantities: the Eulerian and Lagrangian frameworks.

Let us consider a physical quantity f defined in a fluid. In the unperturbed (background) configuration, this quantity at a spatial location x_0^i is denoted by $f_0(x_0^i)$. The Eulerian perturbation, denoted by δf, measures the change in f at a fixed spatial point before and after the perturbation. It is defined as:

$$\delta f(t, x_0^i) = f(t, x_0^i) - f_0(x_0^i). \tag{B.1}$$

This expression compares the same physical quantity at the same spatial location but at different stages, before and after the perturbation.

In contrast, the Lagrangian perturbation, denoted by Δf, tracks the change experienced by an individual fluid element as it moves through space due to perturbation. It is defined by:

$$\Delta f(t, x_0^i) = f(t, x^i) - f_0(x_0^i), \tag{B.2}$$

where x^i is the new position to which the fluid element originally at x_0^i has moved as a result of the perturbation.

To relate the two descriptions, we subtract Eq. (B.1) from Eq. (B.2), yielding:

$$\Delta f(t, x_0^i) - \delta f(t, x_0^i) = f(t, x^i) - f(t, x_0^i). \tag{B.3}$$

To describe this shift in position, we define the Lagrangian displacement vector ξ^i, which connects the position of a fluid element in the background to its perturbed location:

$$\xi^i(t, x_0^i) = x^i - x_0^i. \tag{B.4}$$

This means that a fluid element located at x_0^i in equilibrium is displaced by an amount ξ^i to a new position x^i.

Using this relation in Eq. (B.2), we expand the Lagrangian perturbation to first order as:

$$\begin{aligned}\Delta f(t, x_0^i) &= f\left[t, x_0^i + \xi^i(t, x_0^i)\right] - f_0(x_0^i) \\ &= f(t, x_0^i) + \xi^j(t, x_0^i)\partial_j f_0(x_0^i) - f_0(x_0^i) + O(|\xi^i|^2),\end{aligned} \tag{B.5}$$

where we have assumed that the perturbations Δf, δf, and ξ^i are small and retained only terms up to linear order in ξ^i.

From the above expression, the relation between the Lagrangian and Eulerian perturbations to linear order is:

$$\Delta f = \delta f + \mathcal{L}_\xi f_0, \tag{B.6}$$

where $\mathcal{L}_\xi$ denotes the Lie derivative of f_0 along the displacement vector ξ^i.

While the derivation above assumes f to be a scalar quantity, this relation holds more generally and can be extended to vector and tensor fields, with the Lie derivative accounting for their respective transformation properties under coordinate changes.

Appendix C

A Comparison of Frequencies Between Full GR and Cowling Approximation

In this appendix, we compare the f-mode frequencies of anisotropic stars computed using the relativistic Cowling approximation-where spacetime perturbations are neglected and only fluid variables are evolved, with those obtained from the full general relativistic (GR) treatment used throughout the thesis. It is already well established that the Cowling approximation can introduce an error (mostly overestimation) of approximately 20–30% relative to full GR calculations at linear order in perturbation theory [89, 111, 158]. Figure C.1 shows the variation of f-mode frequencies as a function of the anisotropic strength τ for a fixed stellar mass of 1.4 $M_{\odot}$. Panels (a) and (b) correspond to neutron stars modeled using the BSk19 and BSk21 equations of state (EosS), respectively, while panels (c) and (d) present results for quark stars described by the MIT bag model and EOS-A.

The Cowling approximation consistently overestimates the f-mode frequencies in comparison with the full GR results. The fractional difference remains nearly uniform across the range of anisotropy considered, with average deviations of approximately 23.35 % for BSk19, 30.51 % for BSk21, 35.39 % for MIT bag, and 23.48 % for EOS-A. Notably, this overestimation is already evident in the isotropic case ($\tau = 0$) and persists as τ varies, sug-

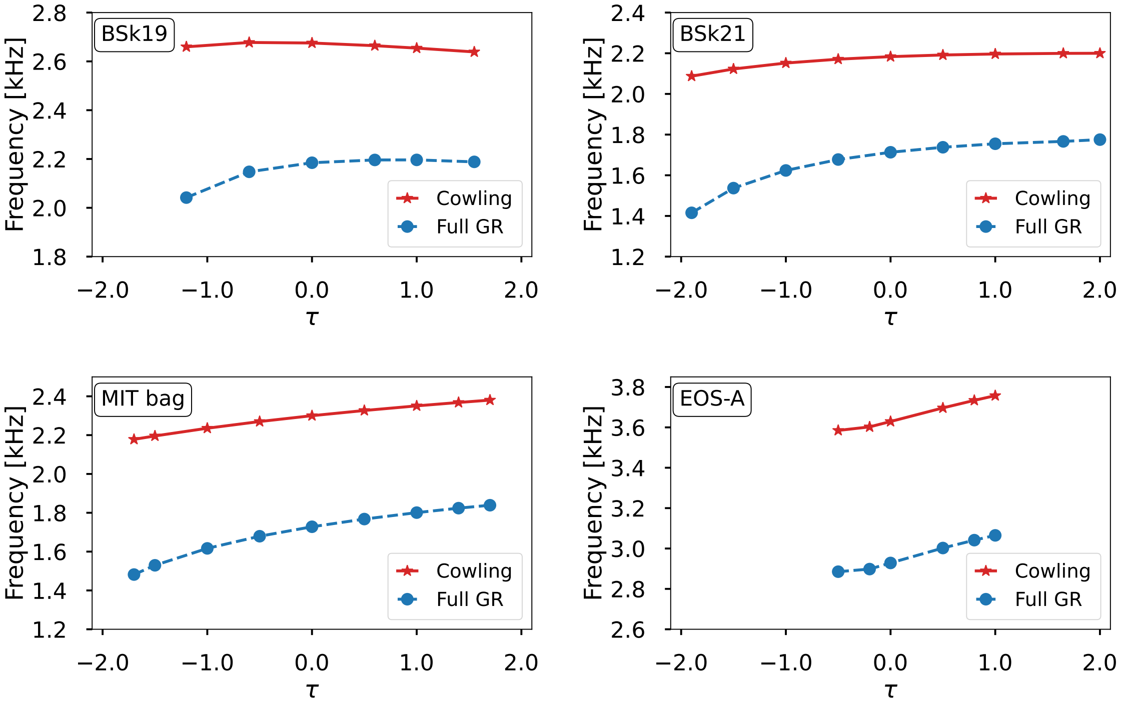

Figure C.1: Comparison of f-mode frequencies computed using full general relativity (as employed in this thesis) and the Cowling approximation, for different equations of state at fixed stellar mass $1.4\,\mathrm{M}_{\odot}$. The top-left panel corresponds to neutron stars modeled with the BSk19 EoS, while the top-right panel corresponds to those modeled with the BSk21 EoS. The bottom-left panel corresponds to quark stars modeled with the MIT bag model, and the bottom-right panel corresponds to quark stars modeled with EOS-A. The variation of frequencies is shown as a function of the anisotropic strength τ.

gesting that the deviation is primarily due to the omission of spacetime dynamics rather than anisotropic effects. These comparisons highlight the limitations of the Cowling approximation in capturing the full dynamical response of anisotropic stars and underscore the importance of employing full GR calculations for accurate mode frequency analysis.

Furthermore, since the Cowling approximation omits metric perturbations altogether, it is incapable of estimating the damping time, which can instead be accessed through the full GR formalism.

Bibliography

[1] D. G. Yakovlev, A. D. Kaminker, P. Haensel, and O. Y. Gnedin, "The cooling neutron star in 3c 58," *Astronomy & Astrophysics*, vol. 389, pp. L24–L27, jul 2002.

[2] V. Doroshenko, V. Suleimanov, G. Pühlhofer, and A. Santangelo, "A strangely light neutron star within a supernova remnant," *Nature Astronomy*, vol. 6, pp. 1444–1451, dec 2022.

[3] A. Einstein, "Die grundlage der allgemeinen relativitätstheorie," *Annalen der Physik*, vol. 354, no. 7, pp. 769–822, 1916. [Online]. Available: https://onlinelibrary.wiley.com/doi/abs/10.1002/andp.19163540702

[4] ——, "Approximative Integration of the Field Equations of Gravitation," *Sitzungsber. Preuss. Akad. Wiss. Berlin (Math. Phys.)*, vol. 1916, pp. 688–696, 1916.

[5] ——, "Über Gravitationswellen," *Sitzungsber. Preuss. Akad. Wiss. Berlin (Math. Phys.)*, vol. 1918, pp. 154–167, 1918.

[6] F. A. E. Pirani, "On the Physical significance of the Riemann tensor," *Acta Phys. Polon.*, vol. 15, pp. 389–405, 1956.

[7] ——, "Invariant formulation of gravitational radiation theory," *Phys. Rev.*, vol. 105, pp. 1089–1099, 1957.

[8] H. Bondi, "Plane gravitational waves in general relativity," *Nature*, vol. 179, pp. 1072–1073, 1957.

[9] A. Abramovici *et al.*, "LIGO: The Laser interferometer gravitational wave observatory," *Science*, vol. 256, pp. 325–333, 1992.

[10] B. C. Barish and R. Weiss, "LIGO and the detection of gravitational waves," *Phys. Today*, vol. 52N10, pp. 44–50, 1999.

[11] R. A. Hulse and J. H. Taylor, "Discovery of a pulsar in a binary system," *Astrophys. J. Lett.*, vol. 195, pp. L51–L53, 1975.

[12] B. P. Abbott *et al.*, "Observation of Gravitational Waves from a Binary Black Hole Merger," *Phys. Rev. Lett.*, vol. 116, no. 6, p. 061102, 2016.

[13] ——, "Multi-messenger Observations of a Binary Neutron Star Merger," *Astrophys. J. Lett.*, vol. 848, no. 2, p. L12, 2017.

[14] G. Agazie *et al.*, "The NANOGrav 15 yr Data Set: Evidence for a Gravitational-wave Background," *Astrophys. J. Lett.*, vol. 951, no. 1, p. L8, 2023.

[15] J. Antoniadis *et al.*, "The second data release from the European Pulsar Timing Array - III. Search for gravitational wave signals," *Astron. Astrophys.*, vol. 678, p. A50, 2023.

[16] H. Xu *et al.*, "Searching for the Nano-Hertz Stochastic Gravitational Wave Background with the Chinese Pulsar Timing Array Data Release I," *Res. Astron. Astrophys.*, vol. 23, no. 7, p. 075024, 2023.

[17] P. Amaro-Seoane *et al.*, "eLISA/NGO: Astrophysics and cosmology in the gravitational-wave millihertz regime," *GW Notes*, vol. 6, pp. 4–110, 2013.

[18] ——, "Laser Interferometer Space Antenna," *arXiv e-prints*, 2017.

[19] M. Punturo *et al.*, "The Einstein Telescope: a third-generation gravitational wave observatory," *Class. Quant. Grav.*, vol. 27, p. 194002, 2010.

[20] M. Maggiore *et al.*, “Science case for the Einstein telescope,” *JCAP*, vol. 2020, p. 050, 2020.

[21] D. Reitze *et al.*, “Cosmic Explorer: The U.S. Contribution to Gravitational-Wave Astronomy beyond LIGO,” *Bull. Am. Astron. Soc.*, vol. 51, no. 7, p. 035, 2019.

[22] M. Evans *et al.*, “A Horizon Study for Cosmic Explorer: Science, Observatories, and Community,” 9 2021.

[23] J. Abadie *et al.*, “Predictions for the Rates of Compact Binary Coalescences Observable by Ground-based Gravitational-wave Detectors,” *Class. Quant. Grav.*, vol. 27, p. 173001, 2010.

[24] Y. Shao, “On the Neutron Star/Black Hole Mass Gap and Black Hole Searches,” *Res. Astron. Astrophys.*, vol. 22, no. 12, p. 122002, 2022.

[25] R. Abbott *et al.*, “GW190814: Gravitational Waves from the Coalescence of a 23 Solar Mass Black Hole with a 2.6 Solar Mass Compact Object,” *Astrophys. J. Lett.*, vol. 896, no. 2, p. L44, 2020.

[26] F. Gittins, “Gravitational waves from neutron-star mountains,” *Class. Quant. Grav.*, vol. 41, no. 4, p. 043001, 2024.

[27] J. Soldateschi and N. Bucciantini, “Detectability of Continuous Gravitational Waves from Magnetically Deformed Neutron Stars,” *Galaxies*, vol. 9, no. 4, p. 101, 2021.

[28] B. Abbott *et al.*, “Search for gravitational wave radiation associated with the pulsating tail of the SGR 1806-20 hyperflare of 27 December 2004 using LIGO,” *Phys. Rev. D*, vol. 76, p. 062003, 2007.

[29] C. Cutler, “Gravitational waves from neutron stars with large toroidal B fields,” *Phys. Rev. D*, vol. 66, p. 084025, 2002.

[30] D. G. Yakovlev, P. Haensel, G. Baym, and C. J. Pethick, “Lev Landau and the concept of neutron stars,” *Phys. Usp.*, vol. 56, pp. 289–295, 2013.

[31] L. D. Landau, “On the theory of stars,” *Phys. Z. Sowjetunion*, vol. 1, p. 285, 1932.

[32] K. R. Lang and O. Gingerich, Eds., *A Source Book in Astronomy and Astrophysics, 1900–1975*. Cambridge, MA and London, England: Harvard University Press, 1979. [Online]. Available: https://doi.org/10.4159/harvard.9780674366688

[33] J. Chadwick, “Possible Existence of a Neutron,” *Nature*, vol. 129, p. 312, 1932.

[34] W. Baade and F. Zwicky, “Cosmic Rays from Super-Novae,” *Proc. Nat. Acad. Sci.*, vol. 20, no. 5, p. 259, 1934.

[35] ——, “On Super-Novae,” *Proc. Nat. Acad. Sci.*, vol. 20, no. 5, pp. 254–259, 1934.

[36] R. C. Tolman, “Static solutions of Einstein’s field equations for spheres of fluid,” *Phys. Rev.*, vol. 55, pp. 364–373, 1939.

[37] J. R. Oppenheimer and G. M. Volkoff, “On massive neutron cores,” *Phys. Rev.*, vol. 55, pp. 374–381, 1939.

[38] A. Hewish, S. J. Bell, J. D. H. Pilkington, P. F. Scott, and R. A. Collins, “Observation of a rapidly pulsating radio source,” *Nature*, vol. 217, pp. 709–713, 1968.

[39] R. N. Manchester *et al.*, “The Australia Telescope National Facility Pulsar Catalogue,” *Astron. J.*, vol. 129, pp. 1993–2006, 2005.

[40] N. Itoh, “Hydrostatic Equilibrium of Hypothetical Quark Stars,” *Prog. Theor. Phys.*, vol. 44, p. 291, 1970.

[41] A. R. Bodmer, “Collapsed nuclei,” *Physical Review D*, vol. 4, no. 6, pp. 1601–1606, sep 1971.

[42] E. Witten, “Cosmic separation of phases,” *Physical Review D*, vol. 30, no. 2, pp. 272–285, 1984.

[43] J. Horvath, L. Rocha, L. de Sá, P. Moraes, L. Barão, M. de Avellar, A. Bernardo, and R. Bachega, “A light strange star in the remnant hess j1731- 347: Minimal consistency checks,” *Astronomy & Astrophysics*, vol. 672, p. L11, 2023.

[44] Y. L. Yue, X. H. Cui, and R. X. Xu, “Is psr b0943+10 a low-mass quark star?” *The Astrophysical Journal*, vol. 649, no. 2, p. L95, sep 2006.

[45] F. Weber, “Strange quark matter and compact stars,” *Progress in Particle and Nuclear Physics*, vol. 54, no. 1, pp. 193–288, mar 2005.

[46] N. A. Gentile, M. B. Aufderheide, G. J. Mathews, F. D. Swesty, and G. M. Fuller, “The qcd phase transition and supernova core collapse,” *Astrophysical Journal*, vol. 414, pp. 701–711, 1993.

[47] K. S. Cheng and Z. G. Dai, “Conversion of neutron stars to strange stars as a possible origin of gamma-ray bursts,” *Physical Review Letters*, vol. 77, no. 7, pp. 1210–1213, 1996.

[48] R. Ouyed, J. Dey, and M. Dey, “Quark-nova,” *Astronomy and Astrophysics*, vol. 390, pp. L39–L42, 2002.

[49] J. Sedaghat, S. M. Zebarjad, G. H. Bordbar, B. Eslam Panah, and R. Moradi, “Is the remnant of gw190425 a strange quark star?” *Physics Letters B*, vol. 833, p. 137388, 2022.

[50] W. C. Ho and C. O. Heinke, “A neutron star with a carbon atmosphere in the cassiopeia a supernova remnant,” *Nature*, vol. 462, no. 7269, pp. 71–73, 2009.

[51] M. Servillat, C. O. Heinke, W. C. Ho, J. E. Grindlay, J. Hong, M. van den Berg, and S. Bogdanov, “Neutron star atmosphere composition: the quiescent, low-mass x-ray binary in the globular cluster m28,” *Monthly Notices of the Royal Astronomical Society*, vol. 423, no. 2, pp. 1556–1561, 2012.

[52] P. Haensel, A. Y. Potekhin, and D. G. Yakovlev, *Neutron stars 1: Equation of state and structure*. New York, USA: Springer, 2007, vol. 326.

[53] W. G. Newton, M. A. Kaltenborn, S. Cantu, S. Wang, A. Stinson, and J. Rikovska Stone, “Glassy quantum nuclear pasta in neutron star crusts,” *Phys. Rev. C*, vol. 105, no. 2, p. 025806, 2022.

[54] K. Hebeler, J. M. Lattimer, C. J. Pethick, and A. Schwenk, “Equation of state and neutron star properties constrained by nuclear physics and observation,” *The Astrophysical Journal*, vol. 773, no. 1, p. 11, 2013.

[55] G. Baym, T. Hatsuda, T. Kojo, P. D. Powell, Y. Song, and T. Takatsuka, “From hadrons to quarks in neutron stars: a review,” *Reports on Progress in Physics*, vol. 81, no. 5, p. 056902, 2018.

[56] S. L. Shapiro and S. A. Teukolsky, *Black Holes, White Dwarfs, and Neutron Stars: The Physics of Compact Objects*. Wiley-Interscience, 1983.

[57] P. Haensel, A. Y. Potekhin, and D. G. Yakovlev, *Neutron Stars 1: Equation of State and Structure*. Springer, 2007.

[58] N. K. Glendenning, *Compact stars: Nuclear physics, particle physics, and general relativity*, 1997.

[59] K. Rajagopal and F. Wilczek, “Enforced electrical neutrality of the color flavor locked phase,” *Phys. Rev. Lett.*, vol. 86, pp. 3492–3495, 2001.

[60] M. G. Alford, A. Schmitt, K. Rajagopal, and T. Schäfer, “Color superconductivity in dense quark matter,” *Rev. Mod. Phys.*, vol. 80, pp. 1455–1515, Nov 2008. [Online]. Available: https://link.aps.org/doi/10.1103/RevModPhys.80.1455

[61] M. Buballa, “Njl-model analysis of dense quark matter,” *Physics Reports*, vol. 407, no. 4, pp. 205–376, 2005. [Online]. Available: https://www.sciencedirect.com/science/article/pii/S037015730400506X

[62] J. L. Zdunik, "On the Minimum radius of strange stars with crust," *Astron. Astrophys.*, vol. 394, pp. 641–646, 2002.

[63] C. Alcock, E. Farhi, and A. Olinto, "Strange stars," *The Astrophysical Journal*, vol. 310, p. 261, nov 1986.

[64] G. Lemaitre, "The expanding universe," *Annales Soc. Sci. Bruxelles A*, vol. 53, pp. 51–85, 1933.

[65] R. L. Bowers and E. P. T. Liang, "Anisotropic Spheres in General Relativity," *Astrophys. J.*, vol. 188, pp. 657–665, 1974.

[66] M. Ruderman, "Pulsars: structure and dynamics," *Ann. Rev. Astron. Astrophys.*, vol. 10, pp. 427–476, 1972.

[67] M. Hoffberg, A. E. Glassgold, R. W. Richardson, and M. Ruderman, "Anisotropic Superfluidity in Neutron Star Matter," *Phys. Rev. Lett.*, vol. 24, no. 14, p. 775, 1970.

[68] A. I. Sokolov, "Phase transitions in a superfluid neutron liquid," *Soviet Journal of Experimental and Theoretical Physics*, vol. 52, p. 575, Oct. 1980.

[69] R. F. Sawyer, "Condensed pi- phase in neutron star matter," *Phys. Rev. Lett.*, vol. 29, pp. 382–385, 1972.

[70] S. Nelmes and B. M. A. G. Piette, "Phase transition and anisotropic deformations of neutron star matter," *Phys. Rev. D*, vol. 85, no. 12, p. 123004, June 2012.

[71] W. Barreto and S. Rojas, "An equation of state for radiating dissipative spheres in general relativity," *Astrophysics and space science*, vol. 193, pp. 201–215, 1992.

[72] W. Barreto, "Exploding radiating viscous spheres in general relativity," *Astrophysics and space science*, vol. 201, pp. 191–201, 1993.

[73] S. Yazadjiev, “Relativistic models of magnetars: Nonperturbative analytical approach,” *Phys. Rev. D*, vol. 85, p. 044030, 2012.

[74] A. Alho, J. Natário, P. Pani, and G. Raposo, “Compact elastic objects in general relativity,” *Physical Review D*, vol. 105, no. 4, p. 044025, 2022.

[75] M. Karlovini and L. Samuelsson, “Elastic stars in general relativity. 1. Foundations and equilibrium models,” *Class. Quant. Grav.*, vol. 20, pp. 3613–3648, 2003.

[76] L. Herrera and N. O. Santos, “Local anisotropy in self-gravitating systems,” *Phys. Rept.*, vol. 286, pp. 53–130, 1997.

[77] H. Shapley, “On the nature and cause of cepheid variation,” *The Astrophysical Journal*, vol. 40, p. 448, dec 1914.

[78] A. S. Eddington, “On the pulsations of a gaseous star,” *Monthly Notices of the Royal Astronomical Society*, vol. 79, pp. 2–22, nov 1918.

[79] R. B. Leighton, R. W. Noyes, and G. W. Simon, “Velocity fields in the solar atmosphere. i. preliminary report.” *The Astrophysical Journal*, vol. 135, p. 474, mar 1962.

[80] K. S. Thorne and A. Campolattaro, “Non-Radial Pulsation of General-Relativistic Stellar Models. I. Analytic Analysis for $L >= 2$,” *Astrophys. J.*, vol. 149, p. 591, 1967.

[81] R. Price and K. S. Thorne, “Non-radial pulsation of general-relativistic stellar models. ii. properties of the gravitational waves,” *The Astrophysical Journal*, vol. 155, p. 163, jan 1969.

[82] L. Lindblom and S. L. Detweiler, “The quadrupole oscillations of neutron stars,” *Astrophys. J. Suppl.*, vol. 53, pp. 73–92, 1983.

[83] S. L. Detweiler and L. Lindblom, “On the nonradial pulsations of general relativistic stellar models,” *Astrophys. J.*, vol. 292, pp. 12–15, 1985.

[84] N. Andersson and K. D. Kokkotas, "Towards gravitational wave asteroseismology," *Mon. Not. Roy. Astron. Soc.*, vol. 299, pp. 1059–1068, 1998.

[85] G. L. Comer, D. Langlois, and L. M. Lin, "Quasinormal modes of general relativistic superfluid neutron stars," *Phys. Rev. D*, vol. 60, p. 104025, 1999.

[86] H. Sotani and T. Harada, "Nonradial oscillations of quark stars," *Phys. Rev. D*, vol. 68, p. 024019, 2003.

[87] H. Sotani, K. Tominaga, and K.-i. Maeda, "Density discontinuity of a neutron star and gravitational waves," *Phys. Rev. D*, vol. 65, p. 024010, 2002.

[88] G. Miniutti, J. A. Pons, E. Berti, L. Gualtieri, and V. Ferrari, "Non-radial oscillation modes as a probe of density discontinuities in neutron stars," *Mon. Not. Roy. Astron. Soc.*, vol. 338, p. 389, 2003.

[89] A. Kunjipurayil, T. Zhao, B. Kumar, B. K. Agrawal, and M. Prakash, "Impact of the equation of state on f- and p- mode oscillations of neutron stars," *Phys. Rev. D*, vol. 106, no. 6, p. 063005, 2022.

[90] V. Boriakoff, "Pulsar ap 2016+28: high-frequency periodicity in the pulse microstructure," *The Astrophysical Journal Letters*, vol. 208, pp. L43–L46, aug 1976.

[91] J. M. Cordes and T. H. Hankins, "Pulsar polarization fluctuations at 430 mhz with microsecond time resolution," *The Astrophysical Journal*, vol. 218, pp. 484–503, dec 1977.

[92] H. M. van Horn, "Micropulses, drifting subpulses, and nonradial oscillations of neutron stars," *The Astrophysical Journal*, vol. 236, pp. 899–903, mar 1980.

[93] B. P. Abbott *et al.*, "GW170817: Observation of Gravitational Waves from a Binary Neutron Star Inspiral," *Phys. Rev. Lett.*, vol. 119, no. 16, p. 161101, 2017.

[94] O. H. Wilson and W. C. G. Ho, “Gravitational waves from glitch-induced f-mode oscillations in quark and neutron stars,” *Phys. Rev. D*, vol. 109, no. 8, p. 083006, 2024.

[95] A. Kumar, P. Thakur, and M. Sinha, “Non-radial oscillations in newly born compact star considering effects of phase transition,” *Mon. Not. Roy. Astron. Soc.*, vol. 530, no. 1, pp. 501–513, 2024.

[96] H.-J. Kuan and K. D. Kokkotas, “f-mode imprints on gravitational waves from coalescing binaries involving aligned spinning neutron stars,” *Phys. Rev. D*, vol. 106, no. 6, p. 064052, 2022.

[97] N. Stergioulas, A. Bauswein, K. Zagkouris, and H.-T. Janka, “Gravitational waves and nonaxisymmetric oscillation modes in mergers of compact object binaries,” *Monthly Notices of the Royal Astronomical Society*, vol. 418, p. 427, 2011.

[98] A. Bauswein, N. Stergioulas, and H.-T. Janka, “Exploring properties of high-density matter through remnants of neutron-star mergers,” *European Physical Journal A*, vol. 52, no. 3, p. 56, 2016.

[99] K. Chakravarti and N. Andersson, “Exploring universality in neutron star mergers,” *Monthly Notices of the Royal Astronomical Society*, vol. 497, no. 4, pp. 5480–5484, oct 2020.

[100] G. Lioutas, A. Bauswein, and N. Stergioulas, “Frequency deviations in universal relations of isolated neutron stars and postmerger remnants,” *Physical Review D*, vol. 104, no. 4, p. 043011, 2021.

[101] J. L. Friedman and B. F. Schutz, “Gravitational radiation instability in rotating stars,” *The Astrophysical Journal Letters*, vol. 199, pp. L157–L159, aug 1975.

[102] S. Chandrasekhar, “Solutions of two problems in the theory of gravitational radiation,” *Physical Review Letters*, vol. 24, no. 11, pp. 611–615, mar 1970.

[103] M. Surace, K. D. Kokkotas, and P. Pnigouras, “The stochastic background of gravitational waves due to the f-mode instability in neutron stars,” *Astronomy & Astrophysics*, vol. 586, p. A86, 2016.

[104] A. Passamonti, E. Gaertig, K. D. Kokkotas, and D. Doneva, “Evolution of the f-mode instability in neutron stars and gravitational wave detectability,” *Physical Review D*, vol. 87, no. 8, p. 084010, 2013.

[105] W. Dong and A. Melatos, “Gravitational waves from non-radial oscillations of stochastically accreting neutron stars,” *Monthly Notices of the Royal Astronomical Society*, vol. 530, no. 3, pp. 2822–2839, may 2024.

[106] J. A. Clark, A. Bauswein, N. Stergioulas, and D. Shoemaker, “Observing Gravitational Waves From The Post-Merger Phase Of Binary Neutron Star Coalescence,” *Class. Quant. Grav.*, vol. 33, no. 8, p. 085003, 2016.

[107] M. Ball, R. Frey, and K. Merfeld, “Prospects for neutron star parameter estimation using gravitational waves from f modes associated with magnetar flares,” *Mon. Not. Roy. Astron. Soc.*, vol. 533, no. 3, pp. 3090–3097, 2024.

[108] W. Hillebrandt and K. Steinmetz, “Anisotropic neutron star models-stability against radial and nonradial pulsations,” *Astronomy and Astrophysics*, vol. 53, pp. 283–287, 1976.

[109] D. D. Doneva and S. S. Yazadjiev, “Gravitational wave spectrum of anisotropic neutron stars in Cowling approximation,” *Phys. Rev. D*, vol. 85, p. 124023, 2012.

[110] E. J. A. Curi, L. B. Castro, C. V. Flores, and C. H. Lenzi, “Non-radial oscillations and global stellar properties of anisotropic compact stars using realistic equations of state,” *Eur. Phys. J. C*, vol. 82, no. 6, p. 527, 2022.

[111] H. Sotani and T. Takiwaki, “Accuracy of relativistic Cowling approximation in protoneutron star asteroseismology,” *Phys. Rev. D*, vol. 102, no. 6, p. 063025, 2020.

[112] C. W. Yip, M.-C. Chu, and P. T. Leung, "The quadrupole oscillations of strange-quark stars," *The Astrophysical Journal*, vol. 513, no. 2, pp. 849–860, mar 1999.

[113] O. Benhar, V. Ferrari, L. Gualtieri, and S. Marassi, "Quark matter imprint on Gravitational Waves from oscillating stars," *Gen. Rel. Grav.*, vol. 39, p. 1323, 2007.

[114] Y. Kojima and K.-i. Sakata, "Discrimination of quark stars from neutron stars in quadrupole oscillations," *Prog. Theor. Phys.*, vol. 108, pp. 801–808, 2002.

[115] X.-L. Zhang, Y.-F. Huang, and Z.-C. Zou, "Recent progresses in strange quark stars," *Frontiers in Astronomy and Space Sciences*, vol. 11, p. 1409463, aug 2024.

[116] J. M. Z. Pretel and C. Zhang, "Universal relations for anisotropic interacting quark stars," *JCAP*, vol. 10, p. 032, 2024.

[117] D. Horvat, S. Ilijic, and A. Marunovic, "Radial pulsations and stability of anisotropic stars with quasi-local equation of state," *Class. Quant. Grav.*, vol. 28, p. 025009, 2011.

[118] M. K. Mak and T. Harko, "Anisotropic stars in general relativity," *Proc. Roy. Soc. Lond. A*, vol. 459, pp. 393–408, 2003.

[119] J. D. V. Arbañil and M. Malheiro, "Radial stability of anisotropic strange quark stars," *JCAP*, vol. 11, p. 012, 2016.

[120] M. Cosenza, L. Herrera, M. Esculpi, and L. Witten, "Some models of anisotropic spheres in general relativity," *Journal of Mathematical Physics*, vol. 22, no. 1, pp. 118–125, 01 1981. [Online]. Available: https://doi.org/10.1063/1.524742

[121] V. Folomeev, "Anisotropic neutron stars in R^2 gravity," *Phys. Rev. D*, vol. 97, no. 12, p. 124009, 2018.

[122] H. O. Silva, C. F. B. Macedo, E. Berti, and L. C. B. Crispino, "Slowly rotating anisotropic neutron stars in general relativity and scalar–tensor theory," *Class. Quant. Grav.*, vol. 32, p. 145008, 2015.

[123] C. E. Rhoades and R. Ruffini, “Maximum mass of a neutron star,” *Phys. Rev. Lett.*, vol. 32, no. 6, pp. 324–327, 1974.

[124] S. Goriely, N. Chamel, and J. M. Pearson, “Further explorations of Skyrme-Hartree-Fock-Bogoliubov mass formulas. XII: Stiffness and stability of neutron-star matter,” *Phys. Rev. C*, vol. 82, p. 035804, 2010.

[125] J. M. Pearson, S. Goriely, and N. Chamel, “Properties of the outer crust of neutron stars from Hartree-Fock-Bogoliubov mass models,” *Phys. Rev. C*, vol. 83, p. 065810, 2011.

[126] J. M. Pearson, N. Chamel, S. Goriely, and C. Ducoin, “Inner crust of neutron stars with mass-fitted Skyrme functionals,” *Phys. Rev. C*, vol. 85, p. 065803, 2012.

[127] A. Y. Potekhin, A. F. Fantina, N. Chamel, J. M. Pearson, and S. Goriely, “Analytical representations of unified equations of state for neutron-star matter,” *Astron. Astrophys.*, vol. 560, p. A48, 2013.

[128] J. W. McKee *et al.*, “A precise mass measurement of PSR J2045 + 3633,” *Mon. Not. Roy. Astron. Soc.*, vol. 499, no. 3, pp. 4082–4096, 2020.

[129] R. W. Romani, D. Kandel, A. V. Filippenko, T. G. Brink, and W. Zheng, “PSR J0952−0607: The Fastest and Heaviest Known Galactic Neutron Star,” *Astrophys. J. Lett.*, vol. 934, no. 2, p. L17, 2022.

[130] C. G. Bassa *et al.*, “LOFAR discovery of the fastest-spinning millisecond pulsar in the Galactic field,” *Astrophys. J. Lett.*, vol. 846, no. 2, p. L20, 2017.

[131] M. Bagchi, “Rotational parameters of strange stars in comparison with neutron stars,” *New Astron.*, vol. 15, pp. 126–134, 2010.

[132] J. L. Zdunik, P. Haensel, and E. Gourgoulhon, “Recycling strange stars to millisecond periods,” *Astron. Astrophys.*, vol. 381, p. 933, 2002.

[133] ——, “The Crust of rotating strange quark stars,” *Astron. Astrophys.*, vol. 372, p. 535, 2001.

[134] M. Dey, I. Bombaci, J. Dey, S. Ray, and B. C. Samanta, “Strange stars with realistic quark vector interaction and phenomenological density dependent scalar potential,” *Phys. Lett. B*, vol. 438, pp. 123–128, 1998, [Addendum: Phys.Lett.B 447, 352–353 (1999), Erratum: Phys.Lett.B 467, 303–305 (1999)].

[135] M. Bagchi, S. Ray, M. Dey, and J. Dey, “Compact strange stars with a medium dependence in gluons at finite temperature,” *Astron. Astrophys.*, vol. 450, pp. 431–435, 2006.

[136] J. L. Richardson, “The Heavy Quark Potential and the Upsilon, J/psi Systems,” *Phys. Lett. B*, vol. 82, pp. 272–274, 1979.

[137] M. Bagchi, M. Dey, S. Daw, and J. Dey, “A model finding a new richardson potential with different scales for confinement and asymptotic freedom, by fitting the properties of Δ^{++} and Ω^{-},” *Nuclear Physics A*, vol. 740, no. 1, pp. 109–118, aug 2004.

[138] M. Bagchi, S. Daw, M. Dey, and J. Dey, “Mean-field baryon magnetic moments and sumrules,” *EPL (Europhysics Letters)*, vol. 75, no. 4, pp. 548–554, aug 2006.

[139] Y. Kojima, “Equations governing the nonradial oscillations of a slowly rotating relativistic star,” *Phys. Rev. D*, vol. 46, pp. 4289–4303, 1992.

[140] T. Regge and J. A. Wheeler, “Stability of a Schwarzschild singularity,” *Phys. Rev.*, vol. 108, pp. 1063–1069, 1957.

[141] F. Gittins, N. Andersson, and J. P. Pereira, “Tidal deformations of neutron stars with elastic crusts,” *Phys. Rev. D*, vol. 101, no. 10, p. 103025, 2020.

[142] N. Andersson and G. L. Comer, “Relativistic fluid dynamics: physics for many different scales,” *Living Rev. Rel.*, vol. 24, no. 1, p. 3, 2021.

[143] C. W. Misner, K. S. Thorne, and J. A. Wheeler, *Gravitation*. San Francisco: W. H. Freeman, 1973.

[144] L. Rezzolla and O. Zanotti, *Relativistic Hydrodynamics*. London, England: Oxford University Press, Aug. 2017.

[145] B. Carter and H. Quintana, "Foundations of General Relativistic High-Pressure Elasticity Theory," *Proceedings of the Royal Society of London Series A*, vol. 331, no. 1584, pp. 57–83, Nov. 1972.

[146] S. Y. Lau, S. Ajith, V. Guedes, and K. Yagi, "Nonradial instabilities in anisotropic neutron stars," 5 2024.

[147] L. Petzold, "Automatic selection of methods for solving stiff and nonstiff systems of ordinary differential equations," *SIAM Journal on Scientific and Statistical Computing*, vol. 4, no. 1, pp. 136–148, 1983. [Online]. Available: https://doi.org/10.1137/0904010

[148] K. Radhakrishnan and A. C. Hindmarsh, "Description and use of lsode, the livermore solver for ordinary differential equations," 1993. [Online]. Available: https://api.semanticscholar.org/CorpusID:53752439

[149] F. J. Zerilli, "Effective potential for even parity Regge-Wheeler gravitational perturbation equations," *Phys. Rev. Lett.*, vol. 24, pp. 737–738, 1970.

[150] T. Zhao and J. M. Lattimer, "Universal relations for neutron star f-mode and g-mode oscillations," *Phys. Rev. D*, vol. 106, no. 12, p. 123002, 2022.

[151] S. Chandrasekhar and V. Ferrari, "On the non-radial oscillations of a star," *Proc. Roy. Soc. Lond. A*, vol. 432, pp. 247–279, 1991.

[152] J.-L. Lu and W.-M. Suen, "Determining the long living quasi-normal modes of relativistic stars," *Chin. Phys. B*, vol. 20, p. 040401, 2011.

[153] N. Andersson, *Gravitational-Wave Astronomy*, ser. Oxford Graduate Texts. Oxford University Press, 11 2019.

[154] S. L. Detweiler, "A variational calculation of the fundamental frequencies of quadrupole pulsation of fluid spheres in general relativity," *The Astrophysical Journal*, vol. 197, pp. 203–217, 1975.

[155] T. O. Kvålseth, "Cautionary note about r2," *The American Statistician*, vol. 39, no. 4, pp. 279–285, 1985. [Online]. Available: https://doi.org/10.1080/00031305.1985.10479448

[156] M. D. Godfrey, "Econometric theory, by arthur s. goldberger, john wiley and sons, new york, 1964, xi + 399 pp," *Naval Research Logistics Quarterly*, vol. 11, no. 2, pp. 230–231, 1964. [Online]. Available: https://onlinelibrary.wiley.com/doi/abs/10.1002/nav.3800110213

[157] S. Chandrasekhar, *The mathematical theory of black holes*, 1985.

[158] B. K. Pradhan, D. Chatterjee, M. Lanoye, and P. Jaikumar, "General relativistic treatment of f-mode oscillations of hyperonic stars," *Phys. Rev. C*, vol. 106, no. 1, p. 015805, 2022.